Universidade de Évora - Escola de Ciências e Tecnologia

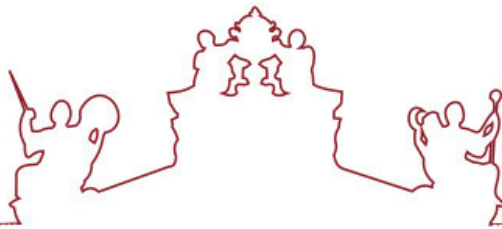Mestrado em Engenharia Mecatrónica

Dissertação

Monitoring and control of a photovoltaic panel in real time

Marlene Dâmaso Mateus

Orientador(es) | Mouhaydine Tlemcani
Fernando Manuel Janeiro

Évora 2022

Universidade de Évora - Escola de Ciências e Tecnologia

Mestrado em Engenharia Mecatrónica

Dissertação

Monitoring and control of a photovoltaic panel in real time

Marlene Dâmaso Mateus

Orientador(es) | Mouhaydine Tlemcani

Fernando Manuel Janeiro

Évora 2022

A dissertação foi objeto de apreciação e discussão pública pelo seguinte júri nomeado pelo Diretor da Escola de Ciências e Tecnologia:

Presidente | João Manuel Figueiredo (Universidade de Évora)

Vogais | Gonçalo Silva (Universidade de Évora) (Arguente)
Mouhaydine Tlemcani (Universidade de Évora) (Orientador)

Évora 2022

Abstract

Monitoring and control of a photovoltaic panel in real time

The performance of the photovoltaic cell, among many factors, also depends on the accurate estimation of its internal and external parameters determined by I-V characterization, whose measurements are affected by noise and the resulting uncertainties. Their determination is of extreme importance and allows the monitoring of the maximum power point (MPP).

The present work aims at designing an innovative numerical and simulation platform for optimal characterization purposes. It is a decision support software applied to the estimation of the photovoltaic cell five parameters. The *modified Nelder-Mead Algorithm* is implemented at its base, which allows the search for the optimum value of each parameter. Furthermore, through an experimental work, it is sought to show the performance of the developed algorithm by applying indicators analysis, namely *RMSE* and *R-squared*. This algorithm will be also implemented in a low-cost embedded system where the purpose is to calculate the MPP.

Keywords

Solar energy

PV Panel

Nelder-Mead Algorithm

Parameter estimation

Sensitivity analysis

MPPT

Resumo

Monitorização e controlo de um painel fotovoltaico em temo real

O desempenho da célula fotovoltaica, entre muitos fatores, depende também da estimativa precisa dos seus parâmetros internos e externos determinados pela caracterização I-V, cujas medições são afetadas pelo ruído e pelas incertezas resultantes. A sua determinação é de extrema importância e permite a monitorização do ponto de potência máxima (MPP).

O presente trabalho visa a conceção de uma inovadora plataforma numérica e de simulação para fins de caracterização ótima. Trata-se de um software de apoio à decisão aplicado à estimativa dos cinco parâmetros de uma célula fotovoltaica. Na sua base encontra-se implementado o *Algoritmo Nelder-Mead modificado*, o que permite a procura do valor ótimo de cada parâmetro. Além disso, através de um trabalho experimental, pretende-se mostrar o desempenho do algoritmo desenvolvido aplicando a análise de indicadores, nomeadamente RMSE e R-squared. Este algoritmo será também implementado num sistema integrado de baixo custo com o objetivo de calcular o MPP.

Palavras-Chave

Energia solar

Painel PV

Algoritmo Nelder-Mead

Estimativa de parâmetros

Análise de sensibilidade

MPPT

Acknowledgment

Contents

List of Figures

Chapter 1

Chapter 2

Chapter 3

List of Tables

Chapter 2

Chapter 3

Nomenclature

Symbol	Description
C	Temperature coefficient
CH_4	Methane
CO_2	Carbon dioxide
e-	Electron
E_g	Band gap
E_{gap}	Band gap of the semiconductor
h+	Proton
H_2O	Water
I	Electric current
I_D	Diffusion current
I_L	Light-generated current
I_p	Measured current
$\hat{I}_p$	Estimated current
I_{ph}	Photoelectric current parameter
I_s	Saturation current parameter
I_{SC}	Short-circuit current
k	Boltzman constant
L_n	Electron diffusion length
L_p	Hole diffusion length
n	Diode ideality factor of the cell
N_s	Number of cells in the module in serial
N_2O	Nitrous oxide
P_{max}	Maximum power point value
q	Charge of the electron
Rs	Serial resistance parameter
R_{sh}	Shunt resistance parameter
R^2	R-squared coefficient
T	Temperature
V	Voltage
V_{best}	The best point value of the simplex
V_F	Direct bias voltage
V_{good}	The second-best point value of the simplex
V_{mp}	Voltage at P_{max}
V_{OC}	Open-circuit voltage
V_T	Thermal potential
V_{worst}	The worst point value of the simplex
x_e	Expanded value
x_{ic}	Inner contracted value
x_{oc}	Outer contracted value
x_r	Reflected value

Acronyms list

Abbreviation	Description
ABC	Artificial bee colony
ABSO	Artificial bee swarm optimization
AC	Alternating current
ADC	Analog-to-digital converter
ANN	Artificial Neural Networks
COMSAT	Communications Satellite Corporation
DAQ	Data acquisition
DC	Direct current
EFG	Edge-defined film-fed growth
EU	European Union
EVA	Ethylene vinyl acetate
FG	Function Generator
GA	Genetic algorithm
GHG	Greenhouse gases
GPIB	General Purpose Interface Bus
GPIO	General Purpose Input/Output
GUIs	User interfaces
I2C	Inter Integrated circuits
IEEE	Institute of Electrical and Electronics Engineers
INC	Incremental conductance methods
kWh	Kilowatt-hour
MPP	Maximum power point
MPPT	Maximum power point tracking
NASA	National Aeronautics and Space Administration
P&O	Perturb and observe
PV	Photovoltaic
RMSE	Root mean square error
RTC France cell	Real Time Clock France cell
SC n	n-layer
SC p	p-layer
USA	United States of America
USB	Universal Serial Bus

Greek symbols

Symbol	Description
μ_X	Mean value
σ_X	Standard deviation value
χ	Expansion coefficient
γ	Contraction coefficient
ρ	Reflection coefficient
σ	Shrinkage coefficient

Notations

This dissertation is written in United Kingdom English. The mathematical expressions, Tables and Figures are properly referenced. The numbering is restarted in each chapter and the mathematical expressions are identified by parentheses (). The style used for referencing articles, books, web sites, among other materials analysed is the IEEE 2006 standard, duly numbered using brackets [].

Communications

This work resulted in two presentations:

1. The first contribution took place at the University of Évora, in the "Jornadas do ICT" and was related to the modelling of the photovoltaic cell and the application developed for parameter estimation. The event was organised by the Institute of Earth Sciences (ICT).

   M. Mateus, M. Tlemçani, F. M. Janeiro, "Monitoring and Control of a Photovoltaic Panel in Real Time", in Jornadas do ICT, University of Évora, Portugal, 2022

2. The second presentation was also held at the University of Évora during the "Festival da Ciência '22" where the practical part of the developed work was shown.

Desktop application installation

The desktop PC application is available in a Drive folder with the following public link: https://drive.google.com/file/d/1b5dH1oFSM5ZcsakS1Fe1bC7JjiRsS4Ia/view?usp=sharing. To install it, just download the application and it is not necessary to have the MATLAB tool installed on the computer.

CHAPTER

1

Introduction

This chapter focuses on the fundamental aspects of the work to be developed. It begins with an introduction which is followed by the motivations and purposes of the work. In this sense, the objectives will be defined, which can be found in the topic created for this effect. A bibliographic review is presented, covering the historical development of solar cells up to state-of-the-art applications. The chapter ends with a description of the dissertation structure.

1.1. Opening Remarks

The accelerated economic, population and technological growth that occurred in the 20th century increased exponentially the consumption of resources for the production of goods and energy, as well as improved the quality of life in cities. This advance was possible due to the use of electrical energy, mostly based on fossil fuels. The intense use of these non-renewable energy sources has contributed to the advance of industrialisation, but also brought negative results with the increase of greenhouse gases in the atmosphere, such as carbon dioxide (CO_2) and methane (CH_4), which cause impact to the quality of life of current and future generations.

However, the oil crisis in the decade of 1970 made countries dependent on this fossil fuel look for alternatives for energy generation. The risk caused by CO_2 emissions from burning fossil fuels and the necessity to find alternatives to the use of coal and oil for generating energy have increased the demand for energy systems with renewable and clean sources, such as solar energy.

Solar energy is the oldest source of energy. The sun was worshipped by many ancient civilisations as a powerful god. The first known practical application was drying for food preservation. [1]

The sun (Figure 1.1.1) is a sphere of extremely hot gaseous matter with a diameter of $1,39 \times 10^9$ m. The sun is about $1,5 \times 10^8$ kilometres away from Earth. As thermal radiation travels with the speed of light in a vacuum (about 300,000 km/s), after leaving the sun, solar energy reaches our planet in 8 minutes and 20 seconds. It has a powerful temperature of 5760 K where in the central region it is higher than on the outer side. In reality, the sun is a nuclear fusion reactor, by means of which hydrogen is transformed into helium. [1]
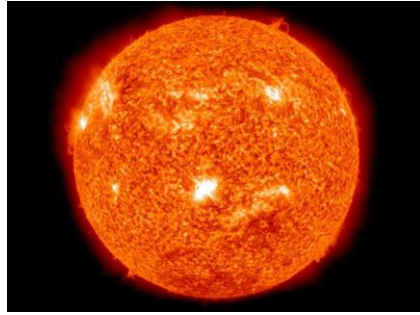
Figure 1.1.1: Sun. [2]

The Sun transfers energy to the Earth through the light it sends to us. Solar radiation refers to the electromagnetic radiation emitted by the sun. Due to the great distance between the sun and earth, only a tiny part of this radiation reaches the earth's surface, which corresponds to an energy quantity of 1 x 10^{18} kWh/year. Due to the eccentricity of the Earth's orbit around the Sun, our planet is closer to the sun in January than in July. Figure 1.1.2 shows the orbit described by the Earth around the Sun, outlining the angles made Earth-Sun. [3]
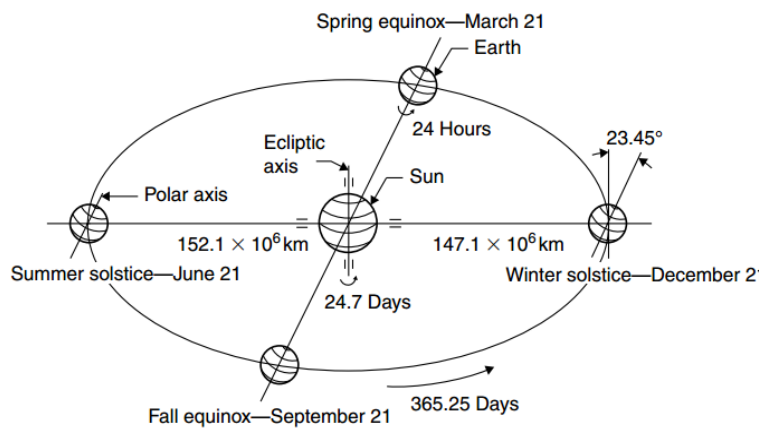
Figure 1.1.2: Orbit described by the Earth around the Sun. [1]

As it is known, solar energy has many applications. Without a doubt, this type of energy does not pollute, does not produce noise, and is used in systems with reliable and long-lasting systems. Solar energy can be subdivided into two main types of energy: thermal and photo-voltaic. [4]

The sun's energy can be harnessed as a source of heat to warm up or for producing electricity. In solar heating systems, heat is captured by solar collectors installed on the roofs of buildings or homes to heat water. Inside the collectors there are tubes through which the water circulates, is heated and then stored in a reservoir. The objective of these systems is to heat water using directly the heat of the Sun, in a simple, clean and efficient way, saving other energy resources such as natural gas, coal and electric energy. [4]

Figure 1.1.3 shows a residence that has solar collectors installed on its roof for water heating.

Figure 1.1.3: Solar thermal collectors for water heating installed on the roof. [4]

Photovoltaic systems do not use heat to produce electricity, interpreting the word photovoltaic, "photo" means produced by photon and the suffix "voltaic" refers to electricity produced by a chemical reaction. Therefore, as will be studied in the Chapter 2, photovoltaic technology allows to directly convert solar energy into electrical energy, normally using silicon as the converting material, and the electrical energy produced has a high degree of reliability. [4]

Unlike solar thermal systems, which are employed to perform heating or to produce electricity from the thermal energy of the sun, photovoltaic systems have the ability to directly capture sunlight and produce electric current. This current is collected and processed by control devices and converters, and can be stored in batteries or used directly in systems connected to the electrical grid. [4]

Photovoltaic modules can be used on the roofs and facades of homes and buildings to supply local electricity needs, Figure 1.1.4 (a), or they can be used in the construction of electricity generating plants, Figure 1.1.4 (b). [4]

(a)   *(b)*

Figure 1.1.4: Photovoltaic panels (a) Photovoltaic panels for electricity generation installed on the roof of a residence. (b) Photovoltaic electricity plant. [4]

The increased use of renewable energies consequently brings competitiveness in the market. Due to these factors, according to a study carried out by the International Renewable Energy Agency (IRENA), it is predicted that the costs of photovoltaic (PV) modules by 2025 could fall by between 18% and 22%. This results in an impressive combination: the price of renewable energy equipment decreases and at the same time it becomes more efficient. The total costs of a solar photovoltaic installation are made up of several components. However, for

simplicity, these are often separated into three categories: module, inverter and balance of
system costs. [5]

Source: IRENA analysis.
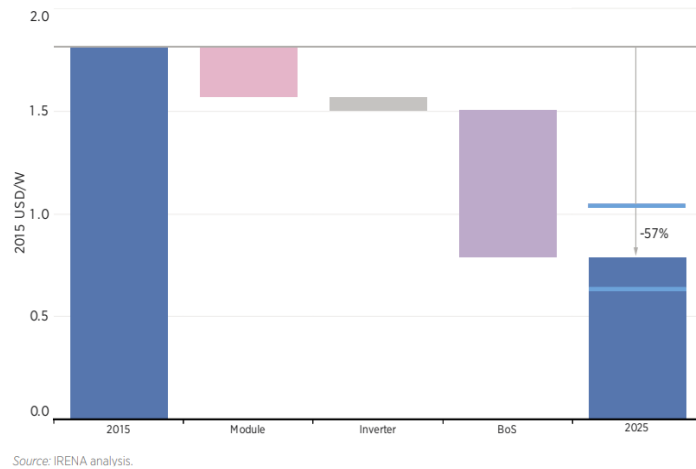
*Figure 1.1.5: Global weighted average total installed costs of utility-scale solar PV systems and costs re-
ductions by source, 2015-2025 [5]*

The graph in Figure 1.1.5 shows that the price value of a 2015 installation is USD 1.8/W and
it is expected to be a 57% reduction in its value to USD 0.8/W in a few 10 years, i.e. in the
year 2025.

Source: IRENA analysis and Photon Consulting, 2016.
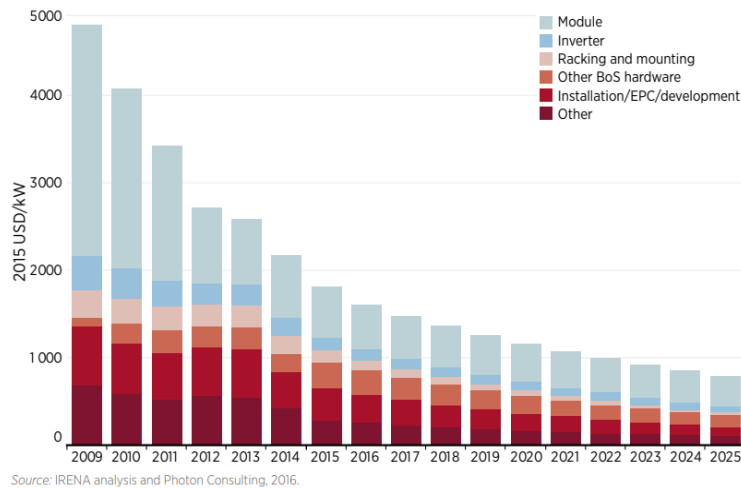
*Figure 1.1.6: Global weighted average total system costs breakdown of utility-scale solar PV systems,
2009-2025. [5]*

Figure 1.1.6 shows the cost forecast at a more comprehensive scale represented by total costs
and also simple cost breakdown, where the difference in each of the three categories is pre-
dicted. The value of the photovoltaic module stands out in particular, presenting an abysmal
cost reduction. [4]

According to the Global Solar Atlas, Portugal is one of the European countries with the highest annual global index of solar radiation of 5.06 kWh/m2 per day, on average, as can be seen in Figures 1.1.7 (a) and 1.1.7 (b).

(a)   *(b)*
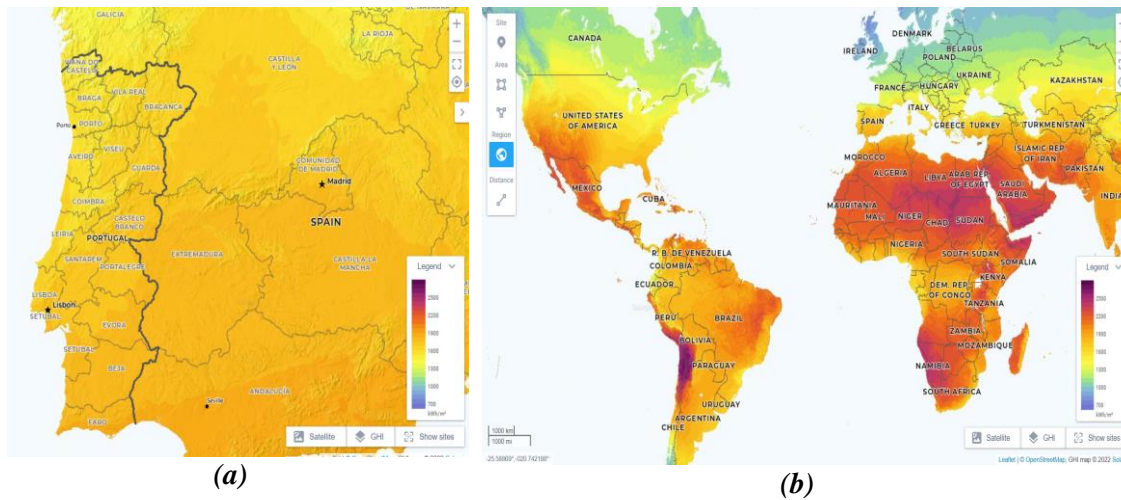
Figure 1.1.7: Annual global radiation (a) Annual global radiation in Portugal. (b) World solar radiation atlas. [6]

By analysing the Figures mentioned above, it can be seen that there is a higher irradiance in southern Portugal. When close to the equator, the hottest regions in the world can exceed 3000 kWh/m2, although in southern Europe it does not exceed 2000 kWh/m2. When comparing the global solar irradiation distributions of two different periods, it is possible to note a general variation.

The solar radiation received in a location depends largely of some factors. [3] Nowadays, there are radiative transfer models (RTM) that allow estimating and simulating the solar irradiance. These models evaluate various parameters such as the day of the year, the angle of the solar zenith, local atmospheric pressure, local temperature, relative humidity, height of the ozone layer concentration, ozone concentration, single scattering albedo, terrestrial albedo, among others. There is published literature where sensitivity studies to the input parameters are done. [7]

1.2. Motivation

Since 1880, the Earth's temperature raised 0.08º Celsius per decade, subsequently the rate of warming since 1981 is more than twice that: 0.18° C per decade. The average temperature of the planet is increasing because human activities are emitting large amounts of greenhouse gases (GHG) into the atmosphere. This could have consequences such as: health problems would become more frequent, economic activities would be seriously affected, wildlife would change resulting in the extinction of species, polar ice caps would melt, among others. The Figure 1.2.1 shows global temperature anomalies in 2021, where the warmest years occurred in the last decade**.** [8] [9]
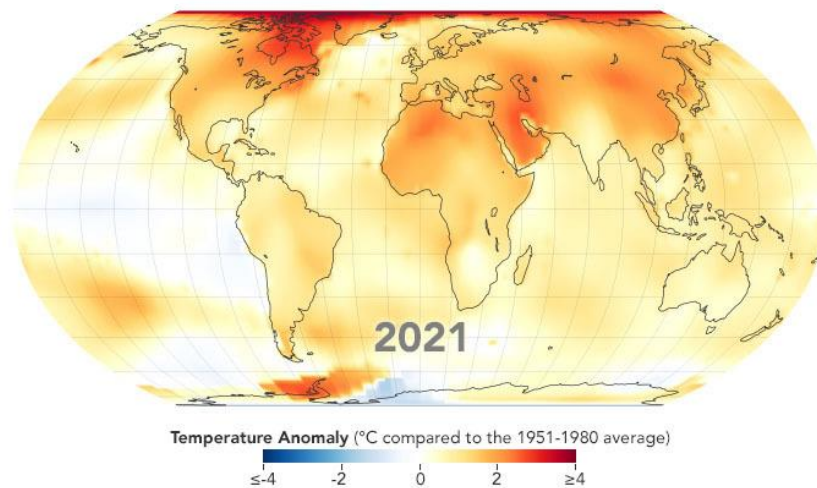
Figure 1.2.1: Global temperature anomalies in 2021. [8]

According to the map, in global warming temperatures do not rise at the same rate across the world, and can rise by 5ºC in one region and fall by 2ºC in others. [8]

The emission of greenhouse gases (GHG) is being affected at a very fast pace, causing great imbalance, and thus promoting accentuated warming in a short period of time. This phenomenon began in the Industrial Revolution, when humanity began to use fossil fuels more intensely to move their machines, and since then, GHG emissions have increased more and more.
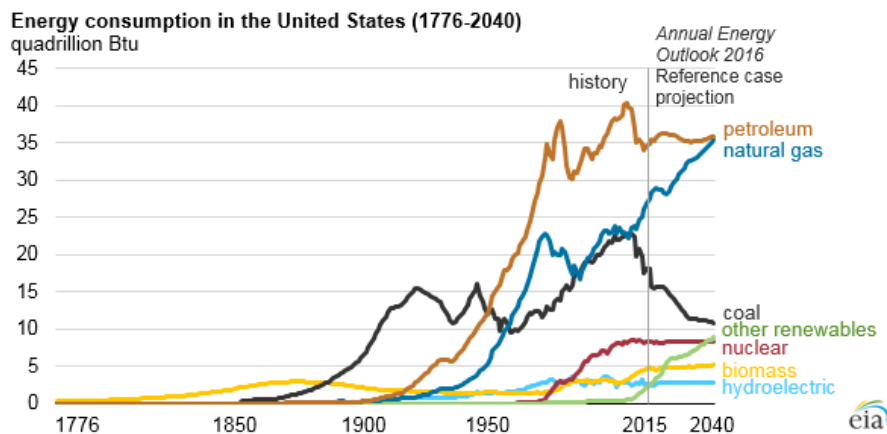
Figure 1.2.2; Forecast of energy consumption up to 2040. [10]

There are different fossil fuels such as coal, petroleum derivatives (such as petrol and diesel oil) and natural gas. The graph in Figure 1.2.2 shows a forecast for energy use up to the year 2040. It is predicted that the use of oil will keep increasing but the use of coal will decrease. [10]

The main global emission when these fuels are burnt, as shown in the Figure 1.2.3, are carbon dioxide (CO_2), methane (CH_4), nitrous oxide (N_2O) and water vapour (H_2O), CO_2 being the most relevant GHG, as it has the highest volume in these emissions.
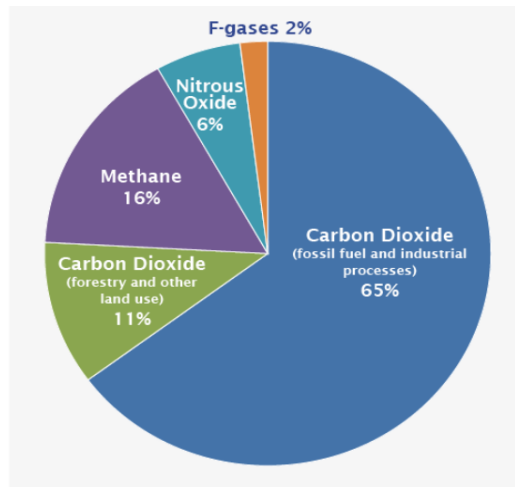
Source: IPCC (2014) EXIT Exit based on global emissions from 2010. Details about the sources included in these estimates can be found in the *Contribution of Working Group III to the Fifth Assessment Report of the Intergovernmental Panel on Climate Change* EXIT . Exit

Figure 1.2.3: Global greenhouse gas emissions. [11]

Many of today's human activities use energy and most of this energy comes from burning fossil fuels. The world's main source of electricity generation is coal. In transport, the energy used to power vehicles comes mainly from combustion. In industry, natural gas and other petroleum derivatives, such as fuel oil, are widely used. All this burning of fossil fuels emits large amounts of GHGs into the atmosphere.
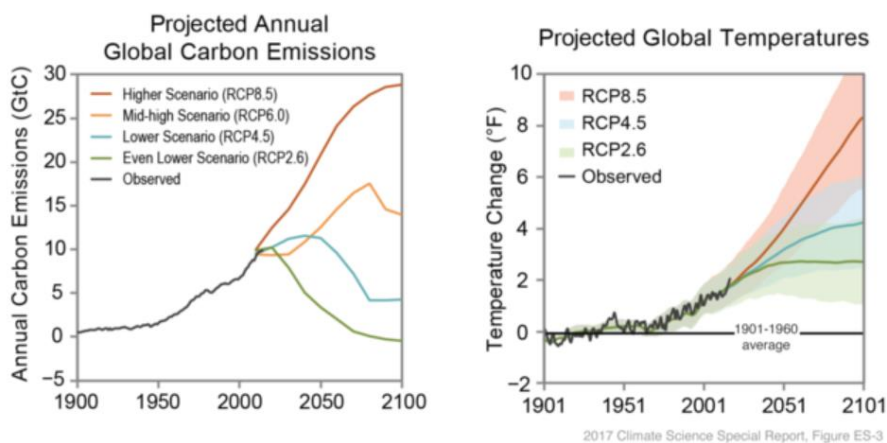
Image by Katharine Hayhoe, from the *2017 Climate Science Special Report* by the U.S. Global Change Research Program.

Figure 1.2.4: Prediction of temperature increase by 100 years as a function of carbon emissions. [9]

According to the data of the Figure 1.2.4 of the 2017 U.S. Climate Science Special Report, "if yearly emissions continue to increase rapidly, as they have since 2000, models project that by the end of this century, global temperature will be at least 5 degrees Fahrenheit warmer than the 1901-1960 average, and possibly as much as 10.2 degrees warmer. If annual emissions increase more slowly and begin to decline significantly by 2050, models project temperatures would still be at least 2.4 degrees warmer than the first half of the 20th century, and possibly up to 5.9 degrees warmer". [9]

In this sense, the necessity to use renewable energies arises. These energies are inexhaustible on a human scale compared to fossil fuels; have no environmental impact compared to energy sources derived from fossil fuels (coal, oil and gas), since they do not produce carbon dioxide or other greenhouse gases; the country becomes energetically independent. However, they may bring disadvantages related to investment costs. [12]

In order to overcome some of these problems, photovoltaic energy can be used. Nowadays, the researches are focused on the following areas:

- Materials for manufacturing photovoltaic cells;
- Power conditionate technologies.

Several studies have been carried out in order to identify the most efficient material to build a photovoltaic cell, such as the article. [13] On the other hand, research is being carried out in the area of the development of algorithms for the characterisation of photovoltaic panels [14], maximum power point trackers or DC/AC and DC/DC converters. [15] [16] There has also been studies directed towards the environmental conditions surrounding the system, where concerns arise mainly linked to the dust that accumulates on the solar panel and shadows generated by objects that surround it. [17]

These are the motivations for the dissertation, where it is intended to extract the maximum performance from a photovoltaic system through robust algorithms, seeking the development of low-cost devices.

1.3. Objectives

The present dissertation has the purpose of studying the five parameters of the single diode photovoltaic cell model, whose equation is non-linear and depends on external parameters (such as temperature) and has a complex behaviour. The aim is to obtain precise values of the parameters in order to identify the maximum value of power that can be extracted from a photovoltaic panel. The study is based on mathematical modelling and its experimental validation on a photovoltaic panel. In this sense, the following objectives are defined for this work:

The first goal will be to implement an algorithm that makes the estimation of the five parameters. The algorithm is the *Nelder-Mead algorithm*, where improvements in its performance are implemented, in particular the initialization and stopping criteria will be distinct from the classical algorithm.

Secondly, a sensitivity analyses will be carried out. Here the error function is studied for each parameter, where a confidence interval is taken. The parameters are submitted to different test conditions namely white noise will be added.

Thirdly, it is intended to create an application that allows the study of the five parameters. This platform will help in the identification of the best initial guesses for each parameter and

it is provided with three distinct screens: The first screen allows for parameter estimation. This screen has a graph showing the convergence of the *Nelder-Mead algorithm* as well as the level lines indicating where the minimum value of the parameter is; The second screen allows to study each parameter individually. It displays the graph of the error function and allows, like the previous screen, to follow the convergence of the algorithm; The last screen shows the exposed problem in a financial perspective whose objective will be to identify the monetary losses if a parameter is not properly estimated.

The last aim of the work comprises the experimental practice, where values are extracted from a photovoltaic panel available in the laboratory and the developed *modified Nelder-Mead algorithm* will be applied. After testing the algorithm, it will be implemented in a low-cost embedded system - ESP32. It is planned that the microcontroller, through a current-voltage sensor, reads the values which allow the IV characteristic curve to be plotted and, using the algorithm developed, indicates the maximum power value of the photovoltaic panel.

1.4. Structure of the dissertation

The dissertation is divided into four main chapters. This section aims to explain the organisation of each one of them.

Chapter 1 is an introductory chapter where the topics to be developed throughout the dissertation are exposed. It is mainly composed of the motivations, objectives and state of the art in the area of photovoltaic energy.

Chapter 2 presents the fundamental concepts of a photovoltaic cell. It starts with physical aspects that explain the functioning of a cell as well as the photovoltaic effect. Then the five and seven parameter mathematical models are explained and the root iteration method used. This chapter also contains the two main topics of this dissertation: here the *modified Nelder-Mead algorithm* developed for parameter estimation is explained; and also shown the interface platform developed that aims to support in the search for the best values to improve the PV performance.

Chapter 3 is devoted to the validation of the *modified Nelder-Mead algorithm* through laboratory experiments. Here two different methods are applied to acquire measurements of a photovoltaic panel: using a current-voltage sensor and a data acquisition system. The chapter ends with the insertion of the algorithm that allows the calculation of MPP in a low-cost integrated system - ESP32.

Chapter 4 depicts the main conclusions taken from the work developed and also gives some guidelines for improving the work in the future.

1.5. State of the art

Edmond Becquerel first observed the photovoltaic effect in 1839. He found that metal plates (silver or platinum) immersed in an electrolyte produced a slight potential difference, but only when exposed to sunlight as shown in the Figure 1.5.1. [18]
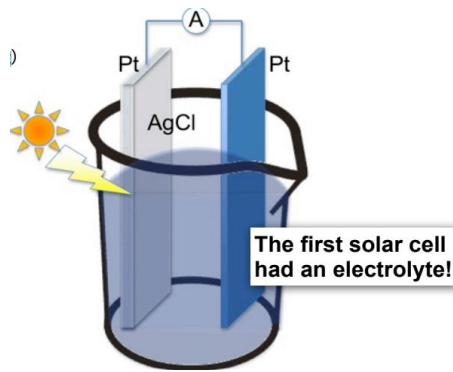
Figure 1.5.1: Becquerel Effect - first method of generating photo-electricity [18]

In 1877 the first solid device for producing electricity through exposure to the sun was produced. The photoconductive properties of selenium were used for this. This device (Figure 1.5.2) was built by two North Americans, W. G. Adams and R.E. Day. [19] This device consisted of a selenium film deposited on an iron substrate and a second semi-transparent gold film which provided a frontal contact. However, it had a low efficiency of around 0.5%.
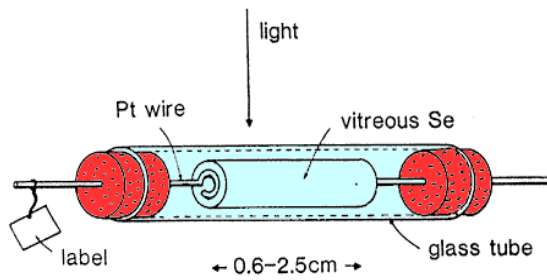
Figure 1.5.2: Solar cell by Adams and Day. [20]

For the great development of photovoltaic energy it was necessary to wait for the scientific developments that took place in the first half of the 20th century, namely with the explanation of the photoelectric effect by Albert Einstein in 1905, for which he was awarded the Nobel Prize in Physics in 1921. [21]

The photoelectric effect was first observed in 1887 by Heinrich Hertz, when he carried out experiments with a spark-gap generator. However, it was the American physicist Robert Milikan who discovered that light with frequencies below a certain value does not inject photoelectrons from the metal surface, regardless of the intensity of the light source, and this result was completely unexpected. This is called the Threshold Frequency (Figure 1.5.3).
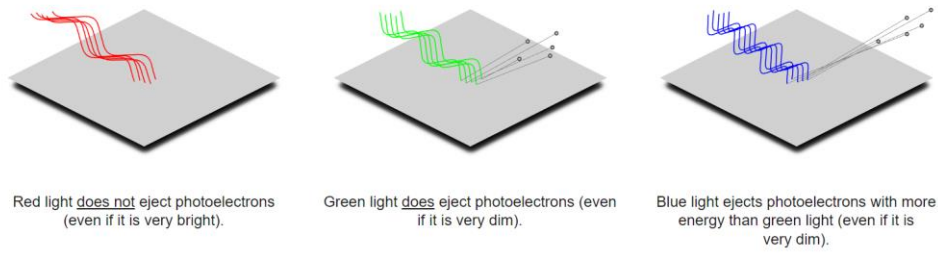
Figure 1.5.3: Typical results of the photovoltaic effect. [22]

However, these results are actually not as typical as one might expect since most elements have threshold frequencies in the ultraviolet region. The materials with lower frequencies are all semiconductors and some have this frequency in the infrared part of the electromagnetic spectrum.

According to the classical physics model, light is described as an electromagnetic wave. This nature of light was confirmed when applied to optical phenomena such as reflection, refraction and diffraction. However, this explanation was not compatible with the photoelectric phenomenon, which does not predict an energy-frequency relationship, but rather an energy-amplitude relationship. [22]

In another way, photoelectrons seem to emerge from the surface. When the light intensity is low the rate of energy delivered to the surface is slow, consequently the time of energy capture by the electron should also be slow. However, this does not happen. When light reaches the surface, at least one electron will appear.

With this problem a new idea appeared: There are two factors that directly affect the maximum kinetic energy of photoelectrons, which are the frequency of radiation and the material of the surface hit. As illustrated in Figure 1.5.4, the energy increases linearly with frequency. It is also possible to verify that all curves have the same slope, being equal to the Planck Constant. As such, it is demonstrated that the energy-frequency relationship is equal in all materials. [22]
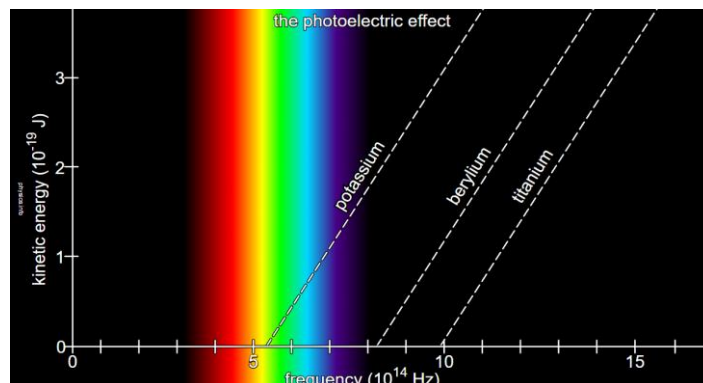
Figure 1.5.4: Photoelectric effect. [22]

In 1905, Albert Einstein realised that light behaved as if it were composed of small particles and that the energy of these particles was proportional to the frequency of electromagnetic radiation of which it was a part. These particles were initially called quanta, being later called photons. [22]

The birth: the first modern solar cell

In March 1953, Calvin Fuller, a chemist at Bell Laboratories in the United States, developed a new process for introducing impurities into silicon crystals. These impurities made it possible to control the electrical properties of silicon. A silicon bar containing a small concentration of gallium (positive *p*-type charges) was produced. The bar was then immersed in a bath of hot lithium, by the physicist Gerald Pearson, creating on the surface of the bar an area with an excess of free electrons (negative *n*-type charges). In the region where the *n*-type silicon is in contact with the *p*-type silicon, a permanent electric field is created, and this area is called the "*p-n* junction".

When exposing the sample to sunlight, Pearson found that it produced an electric current, and the first silicon solar cell was invented. [23]

After the success of the sample, Pearson was in contact with engineer Daryl Chapin. The latter was studying solutions to replace the electric batteries in remote telephone networks. Chapin was experimenting with selenium solar cells, which had been known for a long time, although the results were much poorer than expected. With the new cell, it was possible to verify an energy conversion efficiency close to 4%, much higher than the selenium cells, which were much less than 1% efficient.

As the study of the new cell continued, serious obstacles were quickly encountered. To solve these problems several changes were made to the original model the most important being the replacement of gallium by arsenic followed by boron diffusion, which revealed a record efficiency of 6%.

After Pentagon authorization, the first solar cell (Figure 1.5.5) was presented at the annual meeting of the National Academy of Sciences, Washington, and announced at a press conference on 25 April 1954. The results were published in the Journal of Applied Physics [24] and a patent was also filed. [25]
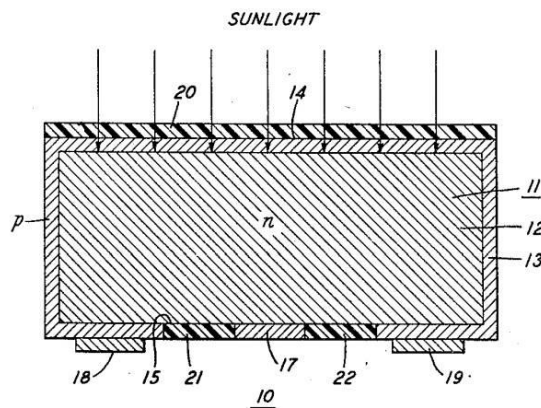
Figure 1.5.5: First solar cell, registered in 1954. [25]

The first application of this new cell was on an isolated telephone line in a town in Georgia, USA. The results were very satisfactory.

Figure 1.5.6: First application of a solar cell in the United States of America, 1955. [26]

After some time of operation, it was quickly realised that solar cells were too expensive and their use was only economically competitive in specific applications. Such applications focus on producing electricity in space.

Childhood and adolescence

At first, satellites used chemical batteries or batteries based on radioactive isotopes. Only with great effort were solar cells incorporated by NASA, but only as a back-up, on Vanguard I (Figure 1.5.7), launched in March 1958. Its chemical battery failed, but the panel of about 100 cm^2 kept the transmitter (5 mW) working for eight years. Only after this demonstration of durability and reliability associated with the low weight of the panel, the North American space programme adopted solar cells as an essential energy source in its satellites.
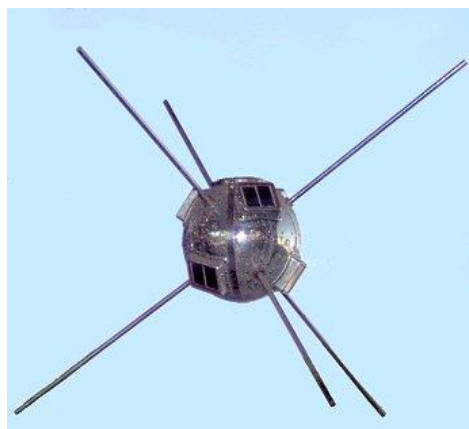
Figure 1.5.7: Vanguard I, the first solar cell satellite launched in March 1958. [27]

It was not only the US space programme that incorporated solar cells, the Soviet programme also did it, as an inexhaustible source of energy for its satellites. Two months after the launch of Vanguard I, the Soviet Union launched Sputnik-3, belonging to the Soviet Union. Today, all space vehicles are equipped with solar cells, such as the International Space Station (ISS) and the Mars Rover shown in the Figure 1.5.8.
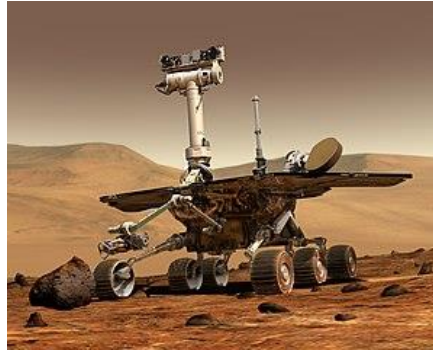
Figure 1.5.8: Mars Rover. [28]

Increasingly efficient cells were developed for use in space, thus leading to some important technological advances in the 1960s [29] and [30].

One of the most significant advances was the so-called "violet cell", from COMSAT Laboratories. [31] This had a significantly thinner *n*-type zone than previous cells, allowing the elimination of the existing inactive zone prior to the surface (improving the response in blue light). The violet cell obtained an efficiency of 13.5%, a record for the time. The use of a Back Surface Field (BSF) on the surface behind the cell (improving the response in red light) [32], and the texturing of the front surface to reduce reflection losses are also noteworthy.

The 1960s also saw the first terrestrial applications for solar cells, notably SOLAREX cells, a company owned by Jospeh Lindmeyer. This company started producing solar cell applications for navigation buoys and remote telecommunication systems. These types of applications were very specific, mainly due to the lack of nearby power sources.

In 1973 there was an oil crisis that brought panic throughout the world. This crisis led to a sudden investment in research programmes to reduce the production costs of solar cells. Some technologies funded in these programmes have completely changed the solar energy paradigm, such as multicrystalline silicon. [33]

In terms of efficiency, the University of New South Wales, Australia, managed for the first time to surpass the 20% barrier [34] while Dick Swanson and his team managed to achieve 25% efficiency in cells with concentrator. [35]

The maturity

The growing awareness of the threat of climate change, notably due to the burning of fossil fuels, led to major investment in programmes to find this form of energy in the 1980s and 1990s. The political powers realised that the creation of a large photovoltaic market could not

only be based on technological development, but had to be based on scale economy: the more cells manufactured, the lower the unit cost. [36]

In 1998 a record efficiency of 24.7% was achieved with monocrystalline silicon cells [37] In 2003, the Fraunhofer Institute for Solar Energy announced an efficiency of 20% for multicrystalline silicon cells. [38] Multi-junction cells, which consist of superposition of multiple layers of semiconductor cells, each sized and optimized for a particular wavelength of solar radiation. These cells make possible to achieve performances of 34%. [39]

Nowadays

Photovoltaic technology is currently divided into three subcategories. First generation cells, made from crystalline silicon, include monocrystalline and polycrystalline solutions. Second generation cells appeared around 30 years ago, and correspond to thin film solutions, where new semiconductor materials are explored. Finally, the third generation cell category comprises several new solar cell concepts, most of which are still only at the development stage. Microcrystalline, nanocrystalline or hybrid solutions are some examples.

I. Crystalline silicon cells (1st Generation)

This is still the technological generation that dominates the market. Today, 90% of the photo generators installed in the world are made from crystalline silicon. Within these, monocrystalline silicon (Figure 1.5.9) is the oldest, and still the one that dominates the market. Typically, it has efficiencies between 15% and 18%, and is used in all types of medium and high-power ground-based applications. Multi-crystalline (or polycrystalline) silicon is a slightly cheaper alternative, but also less performing alternative. Efficiency varies between 12% and 15%, already with an anti-reflection layer. Power cells are a variation, the result of polycrystalline wafer engineering, and can be produced with two photosensitive sides, but have an efficiency of around 10%. Examples of less common technologies are polycrystalline silicon EFG, filament band (polycrystalline) dendritic lattice (monocrystalline), or the polycrystalline Apex cells. [3] [40]

Figure 1.5.9: Monocrystalline silicon solar cell. [41]

II. Thin Film Cells (2nd Generation)

The second generation of cells arises from the necessity to reduce the consumption of silicon, which is too expensive as it requires high temperatures in production and a very high degree

of purity. The thin film also has the advantage of being much less heavy, allowing integrated applications in building facades. The main technology is amorphous silicon (Figure 1.5.10), widely used in professional electronics and in clocks and calculators. Although it has much lower efficiencies than the first generation, in the order of 5% to 7%, it is cheaper to manufacture and operates over a wider range of luminosity: we can use solar calculators with diffused lighting. Copper Indium Diselenide (CIS) cells are more efficient and equally cheap, but they contain Cadmium, a hazardous material and banned by the EU. There is also Cadmium Telluride (CdTe) technology. [3] [40]
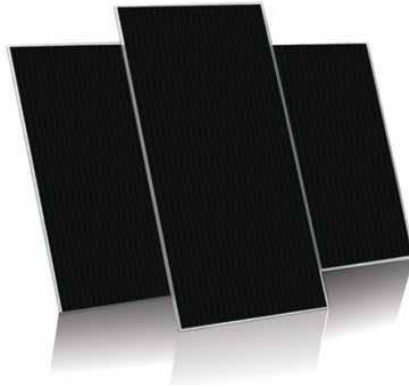
Figure 1.5.10: Amorphous silicon photovoltaic panel. [42]

III.   Recent Solar Cells (3rd Generation)

Many new technologies are still in the research phase. They promise high efficiencies and very low costs. These include nanocrystalline technologies sensitised with colourants, microcrystalline, micromorphic and hybrid (HCI solar cells). It is also important to mention another, already widely used, but only in very specific situations: Gallium Arsenic (GaAs) has yields that can reach 25%, but has very high production costs, which only allow its use in satellites or concentrator systems (CSP). [40]

Figure 1.5.11: Gallium Arsenic photovoltaic panel.[40]

CHAPTER

2

Photovoltaic Cell

This chapter aims to explain how photovoltaic cells work and formulate the mathematical model (single and double diode model) that allows to plot the I-V characteristic curve of a cell. It also describes the modified Nelder-Mead algorithm which enable the estimation of the five PV model parameters, whose determination are extremely important for monitoring the maximum power point (MPP). In order to analyse the performance of the algorithm, a comparison is made with the classical Nelder-Mead algorithm. The chapter ends with the developed numerical simulation platform which is based on the modified Nelder-Mead algorithm and has optimal characterization purposes.

2.1.   Materials and their proprieties

In general, materials are classified according to their properties as belonging to one of the following families: ceramics, glass, metals, polymers, elastomers and composites (hybrid materials that combine the properties of two or more materials) as shown in Figure 2.1.1. [43]
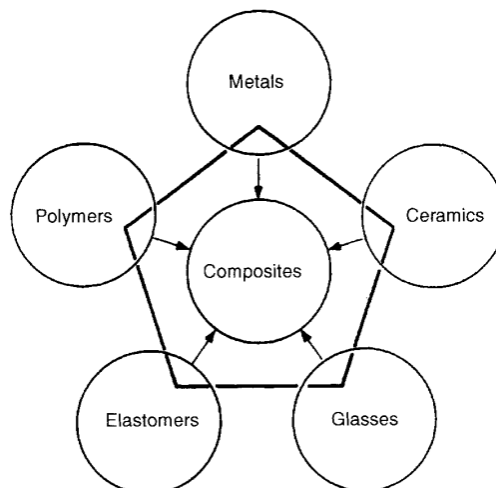
Figure 2.1.1: The menu of engineering materials. [43]

In addition to the materials being distributed among their families (see Figure 2.1.1), they can be grouped according to certain properties. Considering electrical conductivity, there are three major groups: conductors, semiconductors and insulators as shown in the Figure 2.1.2.
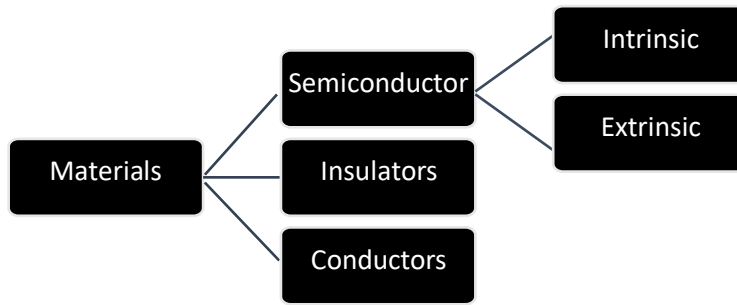
Figure 2.1.2: Material proprieties.

Of all the available materials, metals are the group with the best conductive materials. One of the main characteristics of conducting metals is electrical resistance, the ability of a body to prevent the passage of electric current. In metallic conductors, conduction takes place in the valence band, which is only partially full. Copper, silver and gold also represent examples of conductive metals that have semi-full outer energy bands. [44] [45]

Insulating materials are materials that have low values of electrical conductivity, in other words, they have a high electrical resistance. The electrons are strongly bound to the atoms with ionic or covalent bond. They are not "free" so they cannot conduct electricity unless a large amount of energy is supplied to them. The energy band model of insulators consists of a lower valence band, and an upper conduction band, without electrons (empty). These bands are separated by an energy gap very large (so they do not conduct electricity). These materials are normally used to insulate the conductive parts in a device. Although insulators prevent the passage of electric current some of these materials have high polarizability, the ability to form instantaneous electric dipoles when polarized by an applied electric field - dielectric materials. Thus, insulating materials can be further divided into the following basic groups: dielectric solids, dielectric liquids, gas and vacuum. There are many such materials, such as: ceramics and glass, plastic films, resins and varnishes, elastomers and thermoplastics, among others. [44] [45] The property that distinguishes semiconductors from other materials concerns the behaviour of their electrons, in particular the existence of gaps in their electron excitation spectra. The microscopic behaviour of the electrons in a solid is described according to band theory and is showed in the Figure 2.1.3. [46]
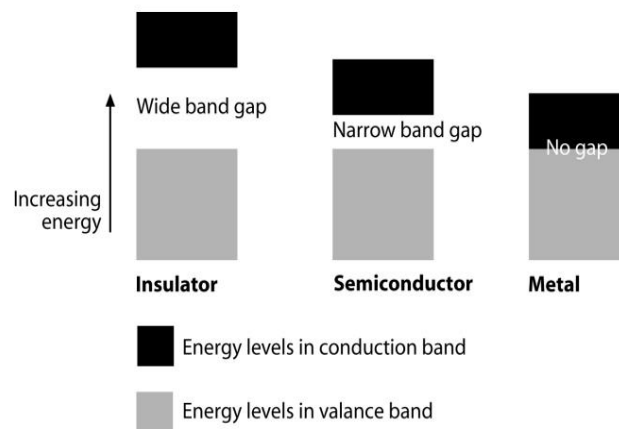
Figure 2.1.3: Band image showing the difference between isolator, semiconductor and metal materials.
[47]

A semiconductor material is defined as a material that exhibits a volume resistivity between 10^{-2} Ωcm and 10^9 Ωcm, a range between insulators and metals. Alternatively, it can be defined as a material whose energy gap for electronic excitations lies between zero and around 4 electron volts (eV). Materials without bound gap are metals or semi-metals, while those with energy gaps greater than 3 eV are better known as insulators. These materials can be of several types: elementary semiconductors, such as silicon (Si), the best-known semiconductor; oxides, such as copper oxide (Cu_2O); layered semiconductors such as gallium selenide ($GaSe$); organic semiconductors, such as polyacetylene ($(CH_2)_n$); magnetic semiconductors, such as manganese (Mn); and several others. They differ, therefore, both in their chemical composition and in their crystalline structure. [46] In this way and according to Figure 2.1.2, semiconductors can be subdivided mainly into two different types: intrinsic or pure semiconductors and extrinsic or impure semiconductors.

Intrinsic semiconductors are pure semiconductors whose electrical conductivity is determined by their intrinsic conductive properties such as Silicon. These elements have the cubic structure of diamond with strongly directional covalent bonds, as shown schematically in Figure 2.1.4. [44]
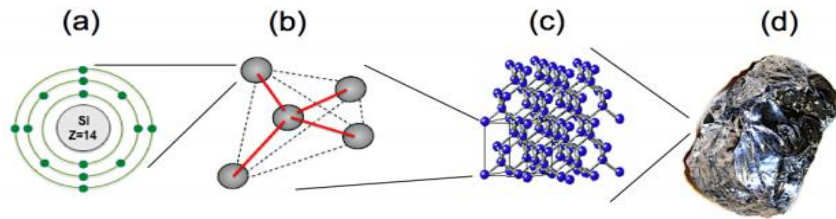
Figure 2.1.4: Silicon: (a) atomic structure, (b) tetrahedral structure, (c) crystalline structure, (d) pure silicon. [44]

In silicon, the atoms are linked tetrahedrally in the crystalline lattice by electron pairs in sp^3 hybrid bonding orbitals. In this structure, each silicon atom contributes four valence electrons. In practice, the crystalline structure is only achieved when the silicon crystal is subjected to the temperature of absolute zero. At this temperature, all covalent bonds are complete (allowing the atom to have chemical and molecular stability); the material therefore behaves like an insulator as there are no free electrons, so it is not possible to establish an electric current through the crystal. [46] Figure 2.1.5 shows the energy gap diagram of an Si semiconductor.
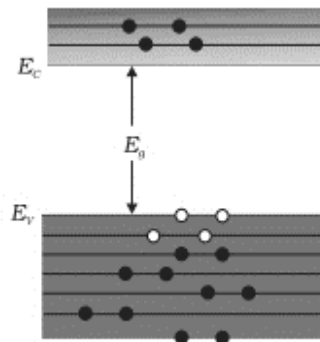
Figure 2.1.5: Schematic of an intrinsic semiconductor energy gap diagram with Si, where Ec is the conduction band, EV the valence band and Eg is the Gap band. [111]

In the energy band diagram of intrinsic semiconductors (such as Si or Ge), the ligand electrons occupy the energy levels of the valence band (which is fully filled at a temperature of 20°C). Above the valence band there is a forbidden energy gap (band gap), where there are no permitted energy states. For silicon at a temperature of 20°C, the energy gap is 1.1eV. On the other hand, above the energy gap lies the empty conduction band, as shown in Figure 2.1.5.

When a silicon crystal is subjected to a temperature of approximately 20°C, the thermal energy (heat) delivered is high enough to excite some electrons from the valence band to the conduction band, thus leaving empty spaces or holes in the valence band. In this way, when an electron is excited into the conduction band, two charge carriers are created: an electron (negative charge) and a hole (positive charge). In the presence of an externally applied electric field (or electric potential difference) the behaviour will be as shown in the Figure 2.1.6.
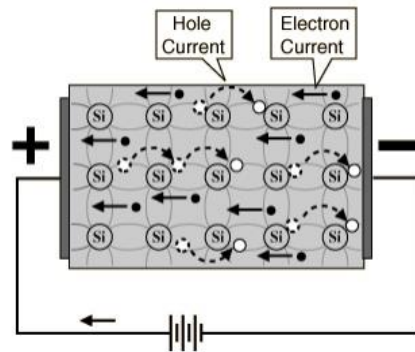
Figure 2.1.6: Movement of holes and electrons in a presence of on externally electric field [48]

The extrinsic semiconductors are very dilute substitutional solid solutions in which the dissolved impurity atoms have valence characteristics that are different from those of the crystalline lattice atoms of the solvent. The doping process consists of the insertion of impurities, i.e., the introduction of atoms of another chemical element into the crystalline structure of silicon. The extrinsic are subdivided into two parts: *n*-type semiconductors and *p*-type semiconductors. [46]

If a Si atom in the crystal lattice of pure silicon is replaced by a phosphorus atom (pentavalent element), then there will be an excess of one electron over and above the four required to establish the covalent bonds in the silicon crystal lattice. In this situation, the extra electron is weakly bound to the nucleus of the phosphorus atom, having a binding energy with a value of approximately 0.05eV. [46]

Thus, two types of elements are added to Si: Boron (B) and Phosphorus (P). [3]

Semiconductors containing impurity atoms of group V (e.g. phosphorus) in their crystal lattices are called *n*-type (negative-type) extrinsic semiconductors, as the main charge carriers are electrons. [3] [46]

Phosphorus has the atomic number 15. Its electronic distribution is 2,8,5. This means that it has five valence electrons and, when the addition is forced with Si, it has an unpaired electron, but this time in excess.
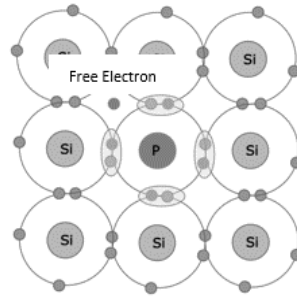
Figure 2.1.7: n-type layer [3]

On the other hand, when the atom of a trivalent element of group 13 (for example boron) is introduced into the crystal lattice of silicon, an electron will be missing from the bonding orbitals. The absence of an electron translates in practice into the appearance of a hole in the tetrahedral bonds of the silicon crystal lattice.

The external supply of a small amount of energy (for example, through the incidence of light) can displace an electron from a neighbouring silicon atom in order to fill the hole in the boron atom. Under these conditions, boron is an electron acceptor atom and is called a *p*-type dopant (positive type) or *p*-type impurity. [44]
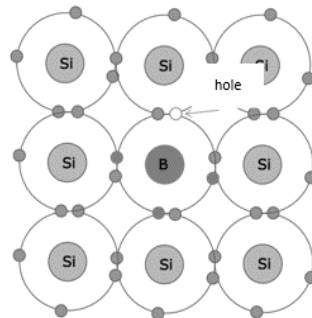
Figure 2.1.8: p-type layer. [3]

2.2. Semiconductor diode

Diodes are electrical components belonging to the semiconductor family. Semiconductors are Silicon (Si) or Germanium (Ge) based devices made by joining two Silicon or Germanium wafers with impurities of different materials, one of them with an excess of positive charges (*p*-type semiconductor) and the other with an excess of negative charges (*n*-type semiconductor). [110] The operation of a *p-n* junction will be described below.

The *p-n* junction is in equilibrium when the terminals are open and no voltage is applied to the device. Considering an *p-n* junction where one side has more holes and the other side has excess of electrons, the gradient of electrons and holes leads to two diffusion currents: electrons flow from the *n*-side to the *p*-side, while holes flow in the opposite direction as shown in the Figure 2.2.1. [50]

n_n : Concentration of electrons on n side
p_n : Concentration of holes on n side
p_p : Concentration of holes on p side
n_p : Concentration of electrons on p side
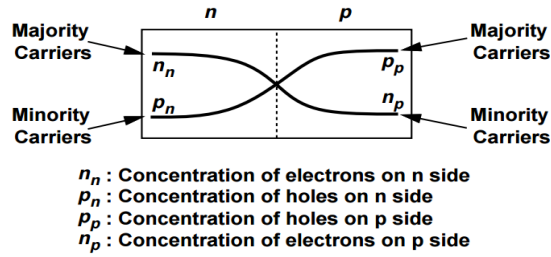
Figure 2.2.1: Diffusion of e-/h+ in an p-n junction. [50]

There is a high amount of charge exchange, which will decay to zero over time because the concentrations become equal on both sides. However, there is an effect that can overpower this and stop the diffusion of currents before it reaches this point. [50]

In this effect, it is recognised that each time an electron leaves the *n*-side, a positive ion is left behind, thus considering t=0 as shown in the Figure 2.2.2. At this point, the diffusion currents continue to expose more ions as time progresses until the "depletion region" is formed due to the lack of free transporters. [50]
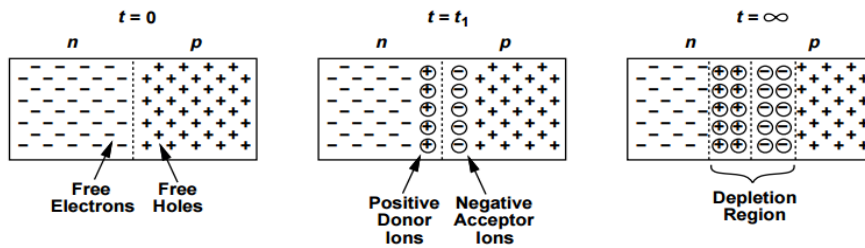
Figure 2.2.2: Evolution of charge concentrations in a p-n junction. [50]

In this way an electric field is created in the depletion region as shown in the Figure 2.2.3.
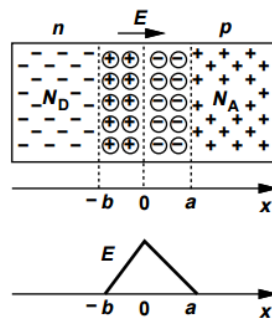
Figure 2.2.3: Electric field profile in a p-n junction. [50]

The electric field tends to force the flow of positive charges from left to right while the concentration gradient requires the flow of charges from right to left. Equilibrium is thus reached when the electric field is strong enough to stop the diffusion currents. In other words, the

junction will come into equilibrium when the drift current due to the action of the electric field equals the diffusion current. The following mathematical expressions (2.1) and (2.2) can be written. [50]

$$|I_{drift,p}| = |I_{diff,p}| \qquad (2.1)$$

$$|I_{drift,n}| = |I_{diff,n}| \qquad (2.2)$$

With the existence of an electric field, a potential difference (V_0) arises at which prevents diffusion across the junction and is determined by the equation (2.3).

$$V_0 = \frac{kT}{q} ln \frac{N_A N_D}{n_i^2} \qquad (2.3)$$

Where k represents the Boltazman constant, T the temperature, q the electron charge, N_A the concentration of acceptor impurities, N_D the concentration of donor impurities and n_i the intrinsic concentration of the semiconductor. [50]

By applying an external voltage across the device as shown in the Figure 2.2.4, the voltage source will make the n-side more positive than the p-side. The junction is therefore inversely polarised. [50]
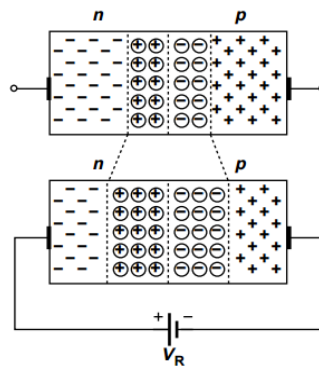
Figure 2.2.4: p-n junction under reverse bias. [50]

In reverse polarisation, the positive terminal being connected to the n-junction will create an electric field in the same direction as the internal electric field of the junction, i.e. there is an intensification of the electric field through the material. In other words, there will be an intensification of positive charges fixed on the n-side and an intensification of negative charges fixed on the p-side and there is an increase in the width of the depletion region preventing diffusion.

In this situation there is still current, but not a diffusion current (I_D). The majority carrier diffusion current tends towards zero as the depletion region increases. However, due to thermal vibration, holes may appear on the n-side and free electrons may appear on the p-side. In

this sense a minority carrier current (I_s) – saturation current is formed, i.e. a reverse bias current which is very small.

The reverse bias *p-n* junction behaves as if it were a voltage-controlled capacitor as shown in the Figure 2.2.5. By increasing the voltage across the junction, we increase the potential barrier where the *n*-side is seen as a positive plate and the *p*-side as a negative plate. In this way, increasing the voltage in reverse bias consequently increases the potential barrier, i.e. the distance between plates decreasing consequently the capacitance. [50]
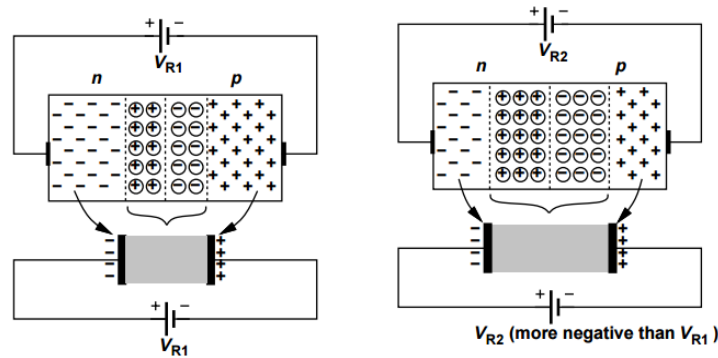
Figure 2.2.5: Reduction of junction capacitance with reverse bias. [50]

Applying a voltage source where the negative terminal is connected to the *n*-junction and the positive terminal is connected to the *p*-junction gives a forward bias (Figure 2.2.7). [50]
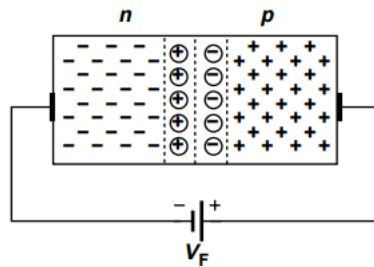
Figure 2.2.6: p-n junction under forward bias. [50]

Thus, the *p*-side is more positive than the *n*-side where at the junction there is an electric field that flows from left to right. However, with forward bias, the source creates an intense electric field from right to left against the *p-n* junction field that has formed at equilibrium to prevent diffusion. Consequently, the field generated by the voltage source will weaken the field created in the depletion region so as to favour the diffusion of charge carriers by the concentration difference. [50]
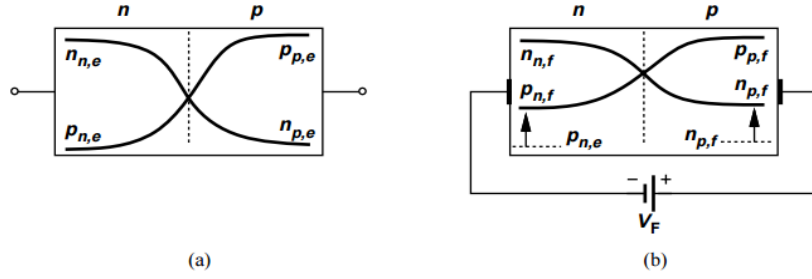
Figure 2.2.7: Carrier profiles (a) in equilibrium and (b) under forward bias. [50]

As shown in Figure 2.2.7 there is an increase in minority carriers on the *p*-side and an increase in minority carriers on the *n*-side. By decreasing the depletion layer we favour the majority carrier diffusion currents (I_D) which will be much more intense than the reverse bias current (I_S) – saturation current. The junction will conduct an intense current which can be demonstrated by the equation (2.4).

$$I_{tot} = I_s (exp \frac{V_F}{V_T} - 1)$$ (2.4)

Where V_F is the direct bias voltage, V_T is the thermal potential which is calculated by the expression in (2.5).

$$V_T = \frac{kT}{q}$$ (2.5)

In turn, the saturation current (I_S) is given by the equation (2.6).

$$I_S = Aqn_i^2 \left(\frac{D_n}{N_A L_n} + \frac{D_p}{N_D L_p} \right)$$ (2.6)

In the equation, A is the cross section area of the device, L_n the electron diffusion length and L_p the hole diffusion length.
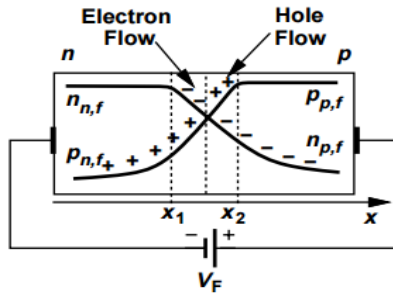
Figure 2.2.8: Variable majority carrier profiles outside the depletion region. [50]

25

The Figure 2.2.8 shows the diffusion and consequently the decrease of carriers. In the case of the electron, these pass from the *p* region to the *n* region and after crossing the depletion barrier, they recombine with holes and their concentration decreases. The same happens with the holes. These diffuse to the *n* region and recombine with electrons thus decreasing the concentration. In this situation, the *p-n* junction conducts current.
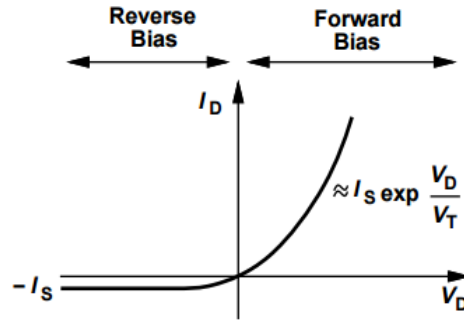
Figure 2.2.9: I-V characteristic of a p-n junction. [50]

The Figure 2.2.9 shows the I-V characteristic curve of an *p-n* junction. In reverse bias, the current is very small, reaching values close to zero. In turn, in forward bias the diode begins to conduct when the applied voltage is greater than or equal to the internal potential of the *p-n* junction. [50]

2.3. Photovoltaic Effect

The photovoltaic effect is a phenomenon that transforms light energy into electrical energy using photovoltaic cells. Its operation is based on the properties of semi-conducting materials. [3] [51]

This process is only possible due to the movement of electrons within the structure of the type of material. The structure of semiconductors consists of a valence band and a conduction band, separated by a gap. The photovoltaic effect occurs when the electrons in the valence band of the semiconductor receive photons with enough energy so that they can jump the gap to the conduction band, creating the electric current. In this section this process is explained in detail.

The photovoltaic cell is a practical application of the photoelectric effect discovered in 1887 by the German physicist Heinrich Rudolf Hertz (1857-1894) and explained in 1905 by Albert Einstein (1879-1955). [44]

The cell consists of two layers of differently doped semiconductor material:

- In the *n* layer there is an excess of peripheral electrons;
- In the *p* layer there is an electron deficit.

When light strikes the surface of a diode, photons with energy equal to or greater than the band gap (E_g) are absorbed, and electron/hole (e^-/h^+) pairs are generated as shown in the Figure 2.3.1.
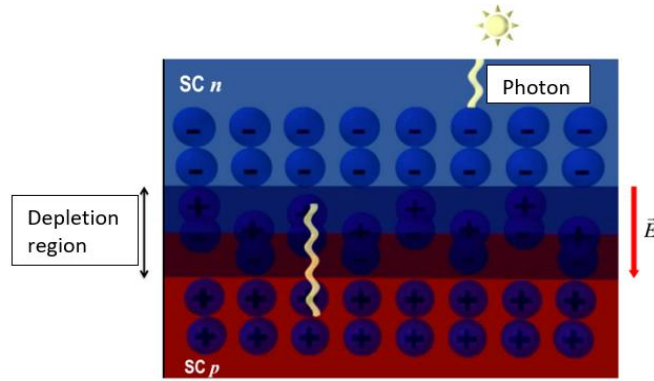
Figure 2.3.1: Schematic representation of a p-n junction diode subjected to the action of light. Adapted from [49]

Light absorption dramatically increases the generation of e^-/h^+ pairs, in addition to generation that comes from thermal excitation. In the presence of the electric field, the electrons will move to the *n*-type semiconductor region, while the holes will move to the *p*-type semiconductor region giving rise to the so-called light-generated current, I_L. Under these circumstances, the system would fall into a state which would result in the loss of its electrical neutrality. Indeed, in this situation, SC *n* would have an excess of electrons, while SC *p* would have a corresponding excess of holes as shown in the Figure 2.3.2. [3] [44]
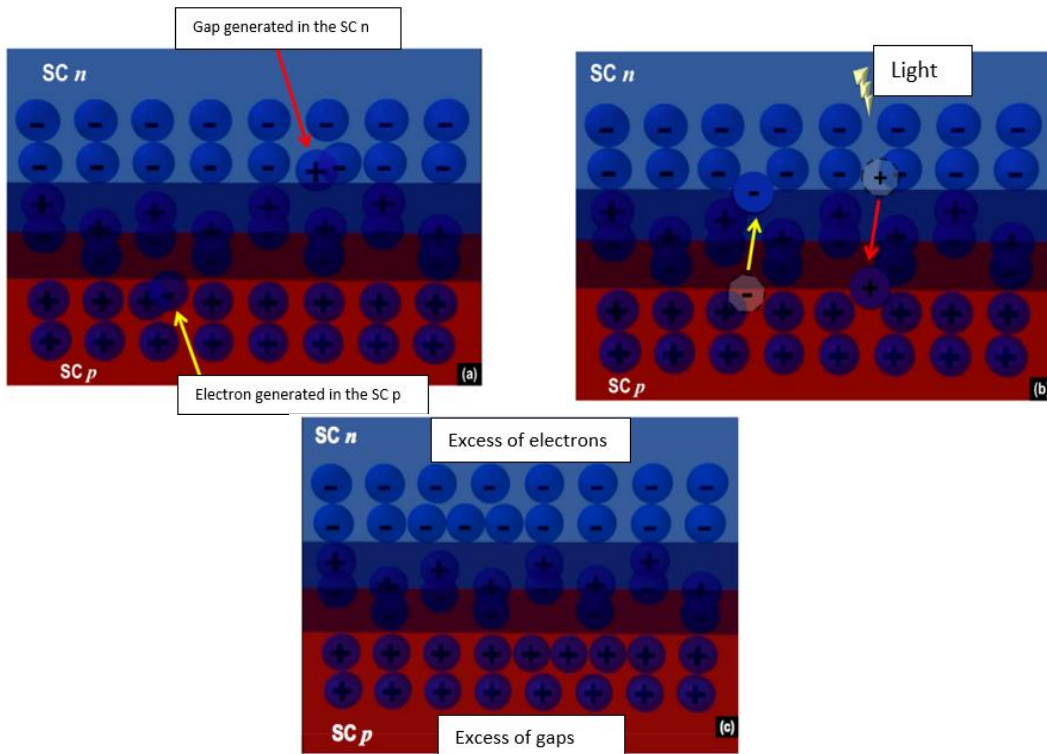
Figure 2.3.2: (a) Schematic representation of the generation of e-/h+ pairs in a p-n junction diode subjected to the action of light.(b) Schematic representation of the movement of e-/h+ pairs through the depletion region of a p-n junction diode subjected to the light action. (c) Schematic representation of the excess charge carriers (electrons in SC n and holes in SC p) after the movement of e^-/h^+ pairs through the depletion region of a p-n junction diode. Adapted from [49]

In this sense, one might think that these electrons and holes could combine. However, the electric field in the depletion region will not allow this to happen. If a conductive wire is used to connect the region of the *n*-type semiconductor to the region of the *p*-type semiconductor, it is found that excess electrons (in the SC *n*) will move through the conducting wire so that they combine with the excess of gaps in the SC *p*. Under these circumstances, an electric current, *I*, is generated. Figure 2.3.3 shows the photovoltaic effect.
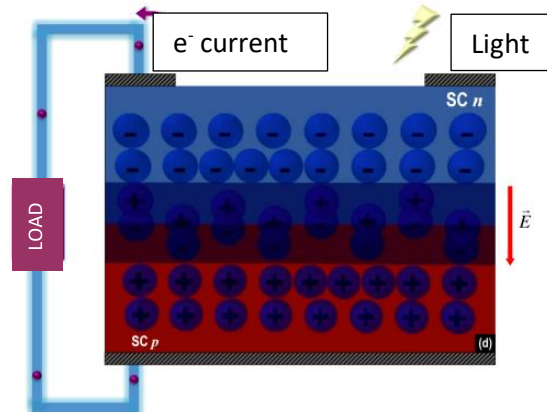
Figure 2.3.3: Schematic representation of the excess charge carriers (electrons in SC n and holes in SC p) after the movement of e -/h+ pairs through the depletion region of a p-n junction diode. Adapted from [49]

The electric current, *I* circulating through the circuit external to the diode is calculated by equation (2.7).

$$I = I_S \left[exp \left(\frac{V}{nV_T} - 1 \right) \right] - I_L \qquad (2.7)$$

where I_L (also represented by I_{ph}) is the current generated by the light, *n* the ideality factor diode, V_t the thermal potential. The electric current *I* flowing through the external circuit is the sum of the contributions of the dark diode current and the light-generated current. This condition, therefore, is called the superposition principle.

The I_L term shifts the current - voltage (I-V) characteristic curve of the diode into the fourth quadrant, where the voltage is positive but the current is negative. Thus, the power absorbed (using the usual sign convention) is negative. In other words, the illuminated diode supplies energy to the external circuit.

Figure 2.3.4 corresponds to the graphical representation of equation (2.7), that is, the current-voltage (I-V) characteristic curve of a *p-n* junction diode under lighting conditions. This schematic representation shows when the junction is in direct bias (i.e. in the presence of an external load in the circuit), current *I* flows and approaches zero as the electrical resistance of the external load increases.

In a photovoltaic cell it is usual to assume that the current supplied by the cell has a positive value. Thus, the *I* axis in Figure 2.3.4 must be inverted (equivalent to multiplying equation by -1) in order to obtain positive values for the current intensity, *I*. [44] [49]
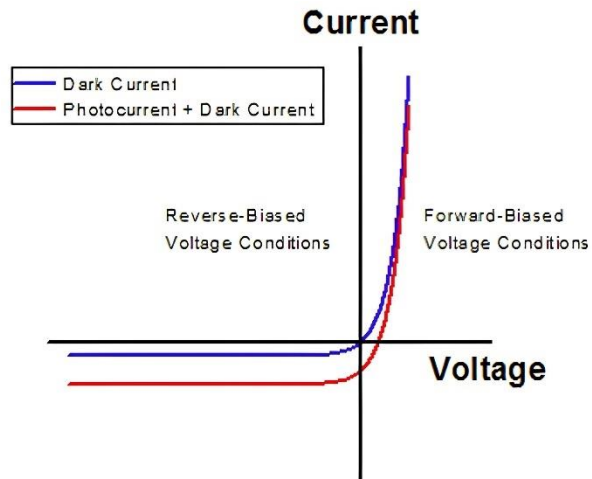
Figure 2.3.4: Schematic representation of the I-V characteristic curve of a p-n junction diode under lighting conditions.[3]

2.4. Photovoltaic panel

Photovoltaic cell, or solar cell, is a device which is able to convert solar radiation directly into electrical energy through the photovoltaic effect. There are several types of solar cells, which are classified according to the materials used in their manufacturing process. Each type of photovoltaic cell has its own characteristics, advantages and disadvantages.

A photovoltaic cell is approximately square in shape with a width of about 15 cm and surface coated with an anti-reflective silicon nitride coating. Figure 2.4.1 shows the active surface of a typical polycrystalline silicon cell.

Figure 2.4.1: Active surface of a photovoltaic cell. [3]

Cells are normally grouped in modules, which are encapsulated with different materials in order to protect the cells and the electrical connectors from environmental conditions. [1] On the other hand, the grouping of several photovoltaic modules is called an installation. [3] The Figure 2.4.2 schematically shows the sequence of assembly to obtain a photovoltaic panel installation.
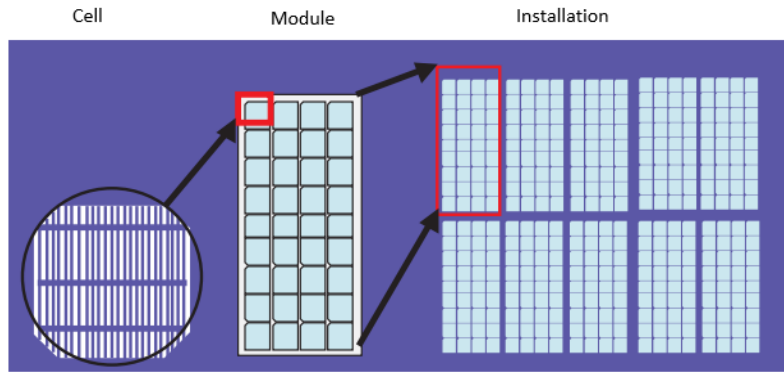
Figure 2.4.2: Cell, module and an installation PV panel photovoltaic. [3]

The combination of photovoltaic modules of the same type can be done by establishing series, parallel or mixed connections, thus obtaining different values of voltage or current. This procedure allows you to control the energy produced by the panel. [3]

The total set of photovoltaic modules is called a photovoltaic generator (Figure 2.4.3). A set of modules in series is called a string, and several can be connected in parallel.
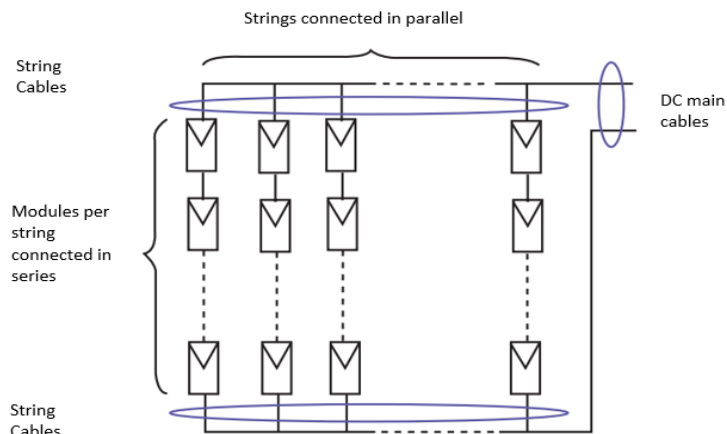
Figure 2.4.3: Composition of a photovoltaic generator. [3]

With the association of modules in series we can have higher voltage values, but the current maintains its value. On the other hand, the association of photovoltaic modules in parallel, the voltage value is maintained, and the value of the current increases the greater the association of PV modules.

The modules, which components are schematically represented in Figure 2.4.4, must be built with characteristics that enable them to resist the adverse environmental conditions to which they will be subjected. In this sense, to ensure protection against mechanical stress, atmospheric agents and humidity, the cells are normally embedded in a film of ethylene vinyl acetate (EVA). It is a flexible, translucent, and non-reflective material for solar radiation, with the additional feature of ensuring electrical insulation between cells. [44]
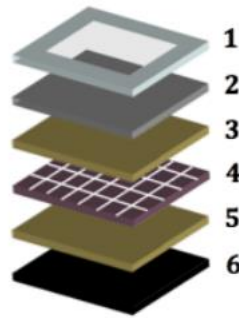
Figure 2.4.4: Schematic representation of the structure of a crystalline silicon photovoltaic module. [44]

For the mechanical stabilisation of the structure, the finishing is carried out with aluminium frames (light and resistant) and a glass panel. Table 2.4.1 describes the functions of each component in a photovoltaic module.

	Components	**Description**
1	*Frame*	Anodised aluminium. Provides mechanical rigidity.
2	*Glass*	Tempered glass. Allows sunlight to enter and protects the cells against mechanical impacts.
3,5	*Encapsulation material*	Translucent film that does not reflect solar radiation. EVA also guarantees electrical insulation between cells.
4	*Photovoltaic cells (c.Si)*	They represent the element that converts sunlight into electric current. It is composed of the *p-n* region.
6	*Electrical isolator*	Protects the back of the module and also prevents the ingress of water and gases

Table 2.4.1: Description of the different functions of the components that make up a photovoltaic module. Adapted from [44]

2.5.   Mathematical model of a photovoltaic cell

The mathematical models used describe the behaviour of the photovoltaic cell, assimilating it as an equivalent electric circuit that includes some linear and non-linear components. The parameters that describe the equivalent electric circuit (PV parameters) are directly related to the performance characteristics. [52]

In the literature there are several mathematical models that allow characterising/simulating the behaviour of a PV cell or module under different operating conditions, where the most well-known are: ideal model, single diode model and double diode model. [52] [53] [54]

The ideal mathematical model consists of a current source and a diode connected in parallel with it. Figure 2.5.1 shows the equivalent electric circuit that symbolizes the ideal behaviour of a PV cell. [55]
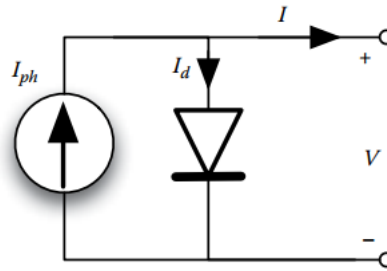
Figure 2.5.1: Equivalent circuit to the ideal mathematical model. [55]

The current source represents the unidirectional current produced by the PV effect, which is called photocurrent (I_{ph}), whose magnitude depends on the intensity of the incident irradiance. The diode represents the *p-n* junction, which functions as a diode that is passed through by an internal unidirectional current, called diode current (I_d), which depends on the voltage (V) at the terminals of the cell.

The characteristic current-voltage (I-V) curve of this circuit depends on the value of I_{ph} and the current density I_d flowing internally through the semiconductor junction of the ideal cell for a given temperature (T) and voltage V at its terminals.

Applying Kirchhoff's laws to the circuit in Figure 2.5.1, the circuit current (I) is given by the equation (2.8). [3]

$$I = I_{ph} - I_d \qquad (2.8)$$

where, the diode current, I_d, is described by equation (2.9) according to Shockley equation.

$$I_d = I_s \left[exp \left(\frac{V}{n \times V_t} \right) - 1 \right] \qquad (2.9)$$

where I_s is the saturation reverse current of the diode, n is the ideality factor of the diode and V_t is the thermal voltage which is given by equation (2.10), where k is the Boltzman constant ($1,38 \times 10^{-23}\ J.K^{-1}$), T is temperature in Kelvin and q is the charge of the electron ($1,60 \times 10^{-19}\ C$).

$$V_t = \frac{k \times T}{q} \qquad (2.10)$$

The saturation reverse current of the diode I_s is expressed by the equation (2.11).

$$I_s = C \times T^3 exp\left(-\frac{E_{gap}}{k \times T}\right) \qquad (2.11)$$

where E_{gap} is the band gap of the semiconductor material and C is the temperature coefficient. Where, for crystalline silicon $E_{gap} = 1{,}8 \times 10^{-19}J$ and for amorphous silicon $E_{gap} = 1{,}72 \times 10^{-19}J$.

Substituting equation (2.9) into equation (2.8), the equation describing the current of the circuit for the ideal model is given by equation (2.12).

$$I = I_{ph} - I_s \left[exp\left(\frac{V}{n \times V_t}\right) - 1\right] \qquad (2.12)$$

Since the ideal mathematical model does not consider voltage and current losses it is necessary to add to this model a series resistance (R_s) and a parallel resistance (R_{sh}) in order to obtain a real model that characterises the behaviour of the cells or PV modules, which is called a single diode model or five-parameter model.

The model of a single diode shown in Figure 2.5.2 consists of: a current source representing the current produced by the PV effect, which depends on the characteristics of the semiconductor material and mainly on the variation of the incident irradiance and the cell or module temperature; a diode which takes into account the physical effects occurring at the *p-n* junction level (diffusion and recombination of charge carriers in the semiconductor) in parallel with the current source whose value varies with temperature and load; a series resistance representing ohmic losses in the semiconductor and in the metal contacts (Joule effect losses), which affects the slope of the curve in the open-circuit area (V_{OC}); a parallel resistance that represents leakage current losses (eddy currents circulating in the cells due to imperfections in the structure of the material), which affects the slope of the curve in the short-circuit zone (I_{SC}). [55] [53]
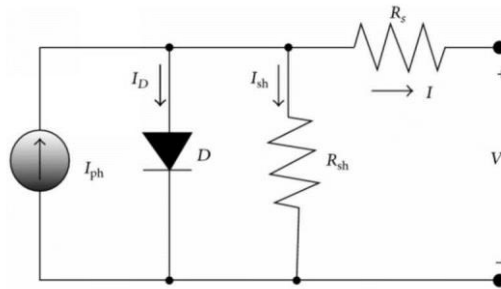
Figure 2.5.2: Equivalent circuit for the mathematical model of a single diode.

The above electrical circuit has five main parameters, these are the photocurrent (I_{ph}), diode saturation reverse current (I_s), diode ideality factor (n), series resistance (R_s) and shunt resistance (R_{sh}). From the above circuit analysis, to determine the expression of the current it is necessary to apply Kirchofft's Laws.

$$I = I_{ph} - I_d - I_{sh} \qquad (2.13)$$

Current flowing through the diode:

$$I_d = I_s \left[exp \left(\frac{q(V + R_sI)}{nKT} \right) - 1 \right] \qquad (2.14)$$

Current flowing through the shunt resistance:

$$I_{sh} = \left(\frac{V + R_sI}{R_{sh}} \right) \qquad (2.15)$$

Substituting expressions (2.14) and (2.15) into expression (2.13), we obtain:

$$I = I_{ph} - I_s \left[exp \left(\frac{q(V + R_sI)}{nKT} \right) - 1 \right] - \left(\frac{V + R_sI}{R_{sh}} \right) \qquad (2.16)$$

Where, the charge current is I, the saturation current of the diode is I_s, the absolute value of the charge of an electron is $(1{,}602 \times 10^{-19}$ C), K is the Boltzmann constant $(1{,}38 \times 10^{-23}$ $J.K^{-1})$ and T (K) is the temperature of the PV cell. The expression of the voltage (V) is obtained similarly to expression (2.16), this being [56]:

$$V = I_{ph}R_{sh} - R_{sh}I + I_s \left[exp \left(\frac{q(V + R_sI)}{nKT} \right) - 1 \right] - \left(\frac{V + R_sI}{R_{sh}} \right) \qquad (2.17)$$

The saturation current (I_s) is affected by the temperature variation of the PV panel and is given by the expression in (2.18).

$$I_s(T) = I_{sn} \left(\frac{T}{T_{nom}} \right)^3 \times exp \left[\left(\frac{T}{T_{nom}} - 1 \right) \frac{E_g}{nV_t} \right] \qquad (2.18)$$

Where, T (K) is the PV cell temperature, T_{nom} (K) is the nominal PV cell temperature, E_g is the gap energy, n is the ideality factor of the diode and V_t is the voltage at the terminal.

The model is characterised by five unknown parameters $p = [I_{ph}, I_s, R_s, R_{sh}, n]$ [57] [58] that can be obtained. [10] [11] From the above expression (2.16) we can conclude that the analytical solution for the current is almost impossible to obtain, since this is a transcendental equation [56]. It will be necessary to resort to computational methods to solve it.

In order to have a more precise model, the two-diode model is introduced: the double diode model. The equivalent circuit is shown in Figure 2.5.3 and it is similar to the previous one, but with the particularity of having two diodes in parallel with the current source, also known as double exponential model. This one describes more accurately the physical phenomena at the *p-n* junction level, one diode represents the diffusion current in the junction, while the

other considers the recombination effect in the space-charge region. It provides better accuracy than the single diode model, especially for low irradiance levels and for polycrystalline technology, however it is more complex due to the increased number of parameters. [54] [59]
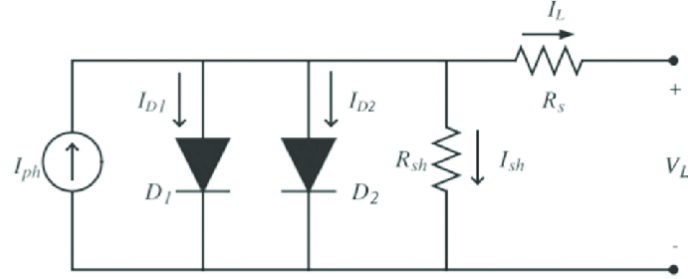
Figure 2.5.3: Equivalent circuit for the mathematical double diode model.

Applying Kirchhoff's laws to the circuit in Figure 2.5.3, the circuit current (I) is given by equation (2.19).

$$I = I_{ph} - I_{d1} - I_{d2} - \left(\frac{V + R_s I}{R_{sh}}\right) \tag{2.19}$$

with the currents of diode 1 (I_{d1}) and diode 2 (I_{d2}) described by equations (2.20) and (2.21) according to the according to the Shockley equation.

$$I_{d1} = I_{s1}\left[exp\left(\frac{V + R_s I}{n_1 \times V_t}\right) - 1\right] \tag{2.20}$$

$$I_{d2} = I_{s2}\left[exp\left(\frac{V + R_s I}{n_2 \times V_t}\right) - 1\right] \tag{2.21}$$

where I_{s1} is the saturation reverse current of diode one obtained in equation (2.22), I_{s2} is the saturation reverse current of diode two obtained in equation (2.23), n_1 is the ideality factor of diode one and n_2 is the ideality factor of diode two.

$$I_{s1} = C_1 \times T^3 exp\left(-\frac{E_{gap}}{k \times T}\right) \tag{2.22}$$

$$I_{s2} = C_2 \times T^3 exp\left(-\frac{E_{gap}}{k \times T}\right) \tag{2.23}$$

C_1 and C_2 represent the temperature coefficient. Substituting equations (2.20) and (2.21) into equation (2.19) the equation describing the circuit current for the double diode model is given by equation (2.24).

$$I = I_{ph} - I_{s1}\left[exp\left(\frac{V + R_sI}{n_1 \times V_t}\right) - 1\right] - I_{s2}\left[exp\left(\frac{V + R_sI}{n_2 \times V_t}\right) - 1\right] - \left(\frac{V + R_sI}{R_{sh}}\right) \quad (2.24)$$

Thus, the double diode model is characterised by seven unknown parameters $p = [I_{ph}, I_{s1}, I_{s2}, n_1, n_2, R_s, R_{sh}]$ which can be obtained in the same way as for the previous model.

2.6. PV cell engineering models

The single diode model offers the desired compromise between accuracy - complexity, and this is the model used in the present work.

With this more detailed model composed of one diode and five parameters, it is possible to obtain the I-V (current-voltage) characteristic curve (Figure 2.6.1) of the panel in certain circumstances, using data supplied by the manufacturer. In the most datasheets the data are taken under STC conditions: temperature $T_{ref} = 25°C$, irradiance e AM=1.5. The data required for a correct determination of the parameters are: [55] [60]

- The open circuit voltage, V_{oc}, corresponding to the point on the I-V curve where there is not electric current, it is the maximum voltage that the cell can produce.
- The short circuit current, I_{sc}, corresponding to the point on the I-V curve where the voltage is zero, is the maximum current flowing in the cell.
- The current and voltage at the point of maximum power, I_{mp} and V_{mp}, correspond to the point on the curve where $I \times V$ is maximum.
- The number of cells in the module, Ns.
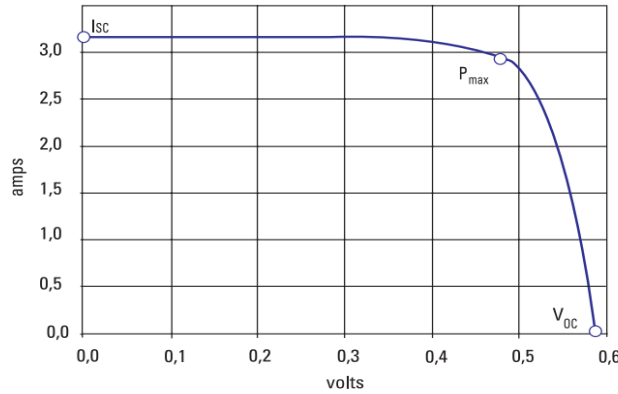
Figure 2.6.1: I-V curve representation, with the relevant values.

In this way, considering the number of cells in series, it is possible to rewrite the equation (2.16) as (2.25).

$$I = I_{ph} - I_s\left[exp\left(\frac{q(V + R_sI)}{N_snKT}\right) - 1\right] - \left(\frac{V + R_sI}{R_{sh}}\right) \quad (2.25)$$

In order to acquire the parameters in question, the equation (2.25) in studied at two distinct points: the short circuit point $(0, I_{sc})$ and the open circuit point $(V_{oc}, 0)$, respectively described by the following equations:

$$I_{sc} = I_{ph} - I_s \left[exp \left(\frac{qR_sI_{sc}}{N_snKT} \right) - 1 \right] - \left(\frac{R_sI_{sc}}{R_{sh}} \right) \qquad (2.26)$$

$$0 = I_{ph} - I_s \left[exp \left(\frac{qV_{0c}}{N_snKT} \right) - 1 \right] - \left(\frac{V_{0c}}{R_{sh}} \right) \qquad (2.27)$$

There are some external factors that affect the behaviour of a photovoltaic cell operating. Under real conditions, each separate set of measurements, temperature and irradiance will affect the values of the measured parameters, and there is only one characteristic I-V curve for each set of measurements. The most notorious consequence to variations in the irradiance value, as can be seen in the Figure 2.6.2 (a), is the linear increase of the short circuit current with irradiance, and a smaller increase of the open circuit voltage is also visible. The main effect of a temperature (Figure 2.6.2 (b)) increase in the cell, is on the open circuit voltage, which decreases linearly with increasing temperature, tending to decrease the efficiency of the cell. [1]
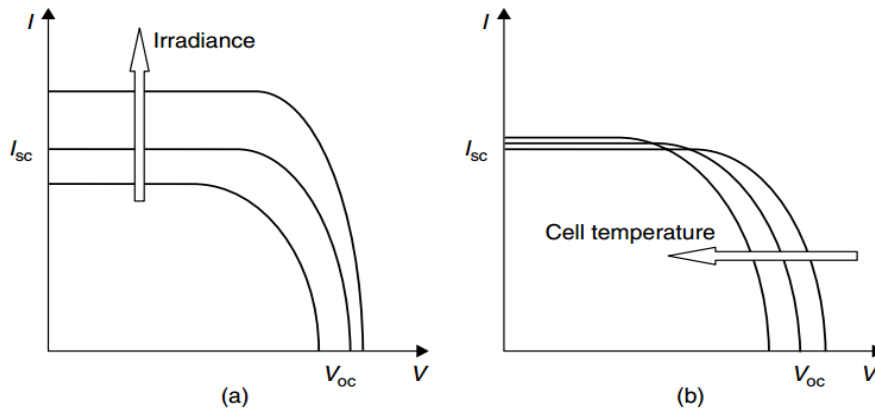
Figure 2.6.2: Effect of irradiance and temperature on the behaviour of the IV curve. (a) Effect of increasing irradiance. (b) Effect of increasing temperature. [1]

2.7.   Implementation of the proposed method

The mathematical equation which describes the behaviour of a photovoltaic cell is non-linear and transcendental. For this reason, it becomes difficult to solve it analytically and it is necessary to apply numerical methods. [61] [62] Studies usually resort to methods such as Newton-Raphson, bisection, false position, secant, Muller, Lambert-W function, among others. [63] [64]

In the studies carried out in the present work, the Newton-Raphson method was used to calculate the current value. For this method it is important to start the method interactions with

the value appropriate to the solution. On the other hand, with increasing number of iterations there are the possibility that may not converge.

The Newton-Raphson method is one of the most widely used for root location and is represented in the Figure 2.7.1. Considering the initial guess x_n, a tangent is extended from the point $[x_n, f(x_n)]$. The point where the tangent crosses the x-axis represents an improvement in the root estimate and this is the new approximation of x_{n+1}. [64] The interaction between the root axis obtained by the formula (2.28).

$$x_{n+1} = x_n - \frac{f(x_n)}{f'(x_n)} \tag{2.28}$$

slope $= f'(x_n)$

$f(x_n)$

x_{n+1} x_n
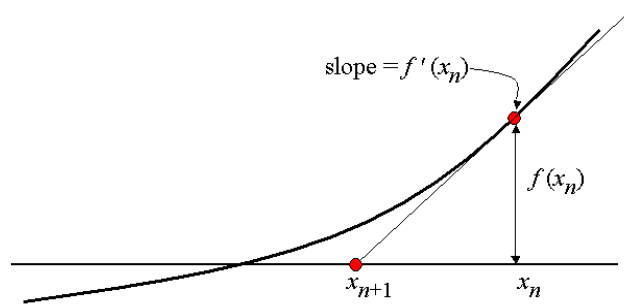
Figure 2.7.1: Graphical depiction of the Newton-Raphson method. "A tangent to the function of x_n [that is $f'(x_n)$] is extrapolated down to the x-axis to provide an estimate to the root at x_{n+1}" [64]

Applying the method to the photovoltaic model in question, the problem consists in solving the equation $f\big(\hat{I}_{(v_i,\tau)}\big) = 0$, expressed by the equation (2.29).

$$f\big(\hat{I}_{(v_i,\tau)}\big) = \left(I_{ph} - I_s \left[exp\left(\frac{q(v_i + R_s\hat{I}_{(v_i,\tau)})}{N_s nKT} \right) - 1 \right] - \left(\frac{v_i + R_s\hat{I}_{(v_i,\tau)}}{R_{sh}} \right) \right) - \hat{I}_{(v_i,\tau)} \tag{2.29}$$

The method evaluates the value of the function $f\big(\hat{I}_{(v_i,\tau)}\big)$, successively, until the stop condition used is reached. During the successive iterations, the method requires knowledge of the derivative of the function $f\big(\hat{I}_{(v_i,\tau)}\big)$ with respect to $\hat{I}_{(v_i,\tau)}$, by equation (2.30), in order to calculate the new value of the estimated current.

$$\frac{\partial f\big(\hat{I}_{(v_i,\tau)}\big)}{\partial \hat{I}_{(v_i,\tau)}} = -\frac{R_s}{R_{sh}} - \left(\frac{I_s R_s q \left[exp\left(\frac{q(v_i + R_s\hat{I}_{(v_i,\tau)})}{N_s nKT} \right) \right]}{N_s nKT} \right) - 1 \tag{2.30}$$

Note that in the stop condition a value $<10^{-9}$ is imposed to return the estimated current value I, in order to contribute to the accuracy of the extracted PV parameters. This same method is also used for the calculation of I_{sc} (equation 2.26) and V_{oc} (equation 2.27) values with the necessary adaptations. The description of the Newton-Raphson method is in the Figure 2.7.2.
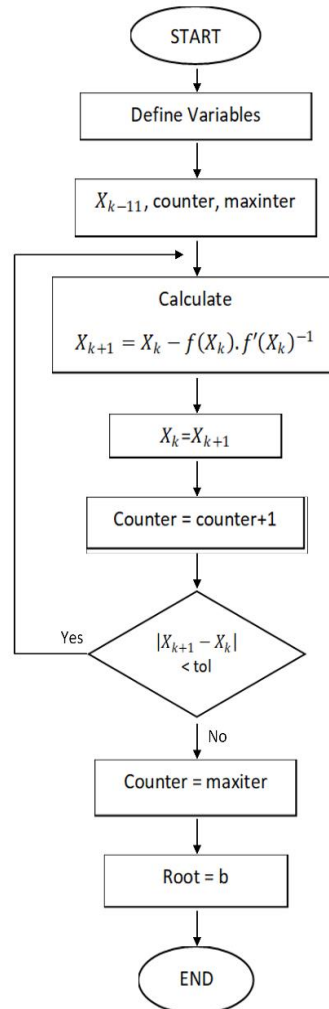
Figure 2.7.2: Flowchart of the Newton-Raphson method.

2.8. Maximum Power Point (MPP) – The problem and solution algorithms

Photovoltaic systems are able to convert solar irradiation into electrical energy under direct current, but it is necessary to convert it in AC so that can be used by households, commerce or industry, for this purpose a converter system is used. The converter system, depending on the application, may present the association of a DC-DC converter with a DC-AC converter, or only a DC-AC converter. This system aims to make the output voltage stable when it operates in alone mode, or when it acts as a controlled current source when connected to the grid, as well as operating the solar panel close to the point of maximum power point (MPP).

The efficiency of a photovoltaic panel is sensitive to external factors such as ambient temperature, solar radiation or the operating state of the module. The objective is to maintain the output power of the photovoltaic array at the point of maximum power (MPP) bringing higher efficiency to the system, which becomes a challenge. Ideally there is only one maximum power point, however different local maximum power points can be identified that result from a partial shadow on the photovoltaic module such as ash, dust, leaves, clouds, among others. [65] [66]

In this way, there are different MPPT search methods, where the easiness of implementation and the efficiency of these techniques are important factors to decide which method to use. The MPPT is an algorithm which can control the DC/DC converter to operate always in the maximum power point (MPP). In other words, through the MPPT it is possible to vary the duty cycle (*d*) of the converter, thus making the panels operate at MPP (Figure 2.8.1). [55]
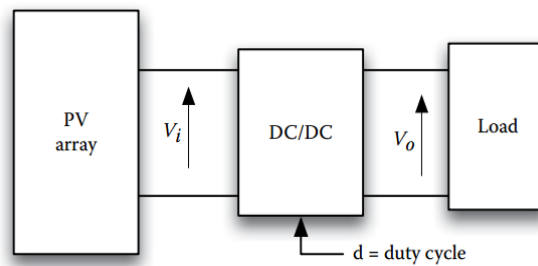
Figure 2.8.1: DC/DC converter scheme for optimising a photovoltaic panel generator. [55]

Instantaneous current and voltage values can be measured at the PV generator terminals, and the MPPT controller dynamically adjusts the duty cycle following the MPP value. The Figure 2.8.2 shows the block diagram on the MPPT implementation.
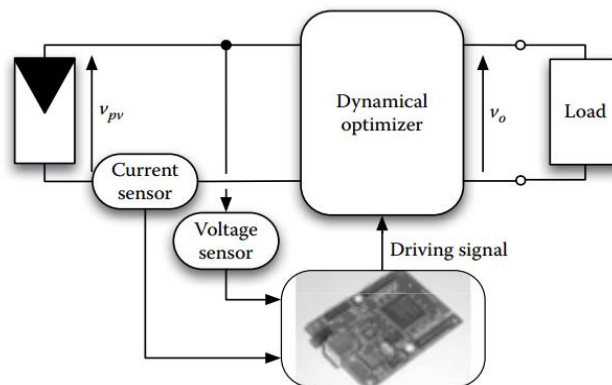
Figure 2.8.2: Block diagram of a MPPT implementation. [55]

There are different methods of parameter extraction and tracking the MPP. The methods vary in their implementation complexity, the speed with which they converge to the MPP value, the costs, the sensors that will be used, their efficiency, among other aspects.

PV modelling techniques, particularly regarding methods for extracting PV parameters, can be grouped according to the type of method used. According to the method used, they are usually grouped into three distinct primary classes: analytical techniques, numerical and Hybrid. [67] [68]

	Analytical techniques	Numerical (deterministic/stochastic)	Hybrid
Description	Analysis of mathematical equations	Gradient-based methods; minimises the error between experimental and simulated IV curve data	Integrate the benefits of both classifications: Analytical and Numerical
Advantages	Methodologies are simple to implement	Susceptible to starting values	To achieve the best of both worlds in terms of efficiency
Disadvantages	Can minimise the efficiency of the model; have different solutions.	Vulnerable to being caught in local optima; deterministic methods can be stuck; the convergence depends of the initial values	Require a high computational effort; parameters must be adjusted experimentally or by trial and error.
Methods' examples	Calculations through IV points and manufactory information	Levenberg–Marquardt algorithm, genetic algorithm (GA), artificial bee swarm optimization (ABSO), artificial bee colony (ABC),etc.	hybrid Nelder-Mead algorithm; hybrid DE with WO, hybrid firefly and pattern search algorithm, hybrid PSO and simulated Annealing, etc

Table 2.8.1: Parameter Extraction Methods. Adapted from [67] [68]

Some of the used methods are perturb and observe method (P&O) and incremental conductance (INC) methods [55], but there are other ones that can be used to bring greater efficiency, one of these being ANN methods. [69] If the photovoltaic panel is also under partial shade conditions, there are also algorithms that search for the global MPP, such as Newton's method. [70] Due to its popularity in the photovoltaic panels field, in the present work a *modified Nelder-Mead algorithm* is implemented whose description is detailed further on in the topic "*Nelder-Mead Algorithm*".

The following is a brief explanation of two of the commonly methods used: P&O and ANN methods.

Perturb and Observe (P&O) method

The P&O method is a used method to track the maximum power point because of its easy implementation. When this system is operating a voltage disturbance is induced and then the

power is measured. If the power increases, then it means that the operating point is approaching the MPP, making the direction of the disturbance the same as before. If the power decreases, it means that the operating point is moving away from the MPP, so the next disturbance will be in the opposite direction of the previous disturbance.

The main disadvantage of this method is that, as the disturbance is continuous, the MPP will never be reached, in other words, the operating point of the system will oscillate around the MPP, but it will never be the MPP. If the disturbance is small, the operating point will be closer to the MPP, but this would leave the system very slow, taking a long time to find the MPP. The block diagram in the Figure 2.8.3 shows an example application of the method where a direct perturbation of the duty ratio of the power converter is applied. [55] This algorithm has been improved according to the literatures. [71] [72]
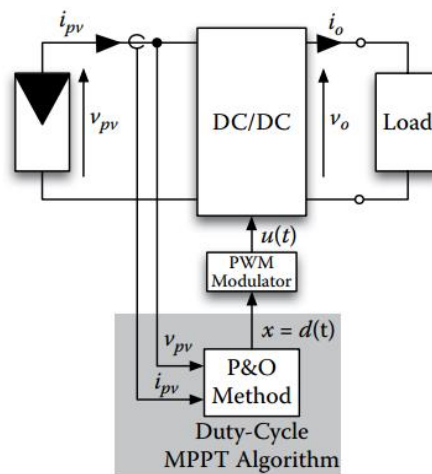
Figure 2.8.3: P&O algorithm block diagram. [55]

Artificial Neural Networks (ANN) method

The technique of artificial neural networks is based on the behaviour of biological nerve cells, where artificial neurons seek to reproduce the physiology of a neural network of human beings. ANNs are basically parallel distributed systems, which are composed of interconnected processing units (nodes) that calculate, based on input values, the weights in each layer. [73] [74]

In the Figure 2.8.4 it is possible to see the similarity of a biological neuron with an artificial neuron, where the inputs of the artificial neuron (x_i) are similar to the dendrites (receiving terminals) of a biological neuron, the sum function (Σ) represents the body of the biological neuron, the activation function (φ), generally a linear or hyperbolic-tangent function, represents the performance of the chemical reactions along the biological neuron and the output (y_j) represents the terminals of the Axon. The index i is the number of inputs of the ANN and the index j is the number of neurons.

There is also a set of synaptic weights (w_{ji}) that represents the synaptic connections of neurons, in other words, it is where information processing occurs. In the biological neuron, each dendrite has different reactions and can have an excitatory or inhibitory character to the

postsynaptic neuron. The weights play the excitatory or inhibitory disposition of the inputs. The term *b* added to the mathematical model is the bias or activation threshold**. [75]**
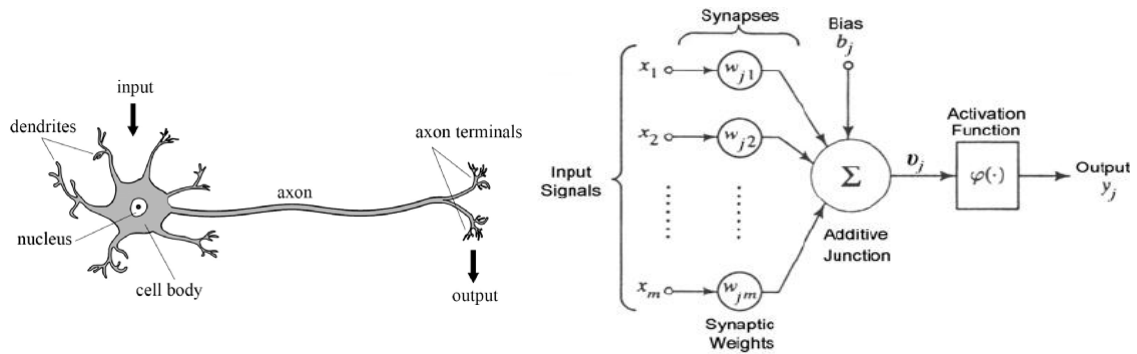
Figure 2.8.4: Biological and artificial neuron. [75]

Thus, it is possible to mathematically represent the output of an artificial neuron according to the equation in (2.31).

$$y_i = \varphi \left(\sum_{i=1}^{N} w_{ji}.x_i + b \right) \tag{2.31}$$

There are different types of architectures and topologies for ANNs. In the case of architecture, it defines if feedback will be necessary or not, or if it will be a single or multi-layer network. The ANN is formed by three or more layers, being an input layer, one or more hidden layers and an output layer. The input layer receives the input data. Usually, inputs are standardized to facilitate the working ranges in which the activation function should act, in the case of the logistic function, each input should be normalized to a range between [0, 1]. The hidden layer is responsible for all the knowledge processing of the network, where neurons are responsible for extracting and storing the knowledge coming from the external environment. Finally, the layer that gets all the signal processed by the network. [73]
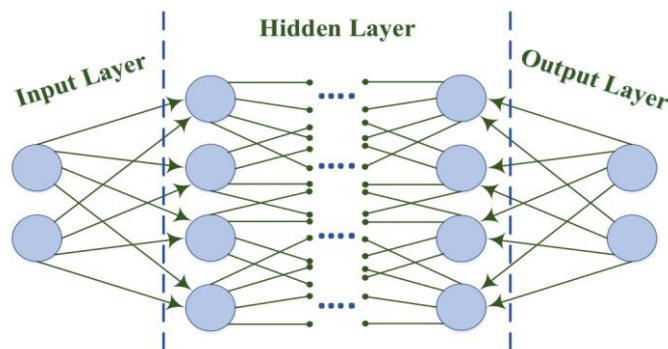
Figure 2.8.5: Diagram of the multilayer feed forward structure. [73]

The most important characteristic of an ANN is its ability to learn based on examples in order to reach the desired output value or to get as close as possible to this result. To achieve this,

the ANN must be trained through an iterative process of adjustments applied to synaptic weights, thus minimizing the error with the sequential adjustment of weights. There are different algorithms for training ANNs, and the backpropagation algorithm is one of the most used. [75] [76]

The ANN technique has a good output behaviour to track the MPP even when it has a large variation in temperature and irradiance, however, each photovoltaic system will need a specific ANN, since the network "learns" the characteristics of the modules used. There are different input variables for an ANN aiming to track the MPP of a photovoltaic system. Usually, solar irradiance and temperature are used, however other variables present in the manufacturer's catalogue can be used such as V_{OC}, I_{sc}, V_{mp} and I_{mp}. [73]

2.9.   Nelder-Mead algorithm and applied improvements

The Nelder-Mead algorithm is a heuristic numerical method for finding the minimum or maximum of an objective function in a multidimensional space. It was published first time by Nelder and Mead in 1965**.** [62]

The method minimizes the function of *n* independent variables using *n+1* vertices of a simplex (regular polyhedral in $\mathbb{R}^n$). Each vertex is defined by a vector *x*. The vertex where the function takes the highest value is projected through the centre of gravity (centroid) of the remaining vertices. Replacing the point where the value of *f(x)* is higher by better points, the minimum of *f(x)* can be found.

Considering a function with five variables (PV model), the simplex is composed of six vertices which compares the vertices by the value of the function.

The vertex where the value of the cost function is higher is considered the worst vertex, and in the next iteration it is replaced by a new one. Throughout the process different simplex with different shapes are generated, where the values of each vertex are increasingly smaller, consequently, reducing the sizes of the simplex until the minimum value is reached. The process finishes when the convergence criteria is attended. In practice, the *Nelder-Mead algorithm* minimizes the residuals between the theoretical models and the measured data. [77]

To search for a new candidate to replace the worst point found in the point set, five different transformations are used: reflexion, expansion, outer contraction, inner contraction and shrinkage. Figure 2.9.1 illustrates the transformations for a problem of two variables, thus having three vertices creating a triangle.
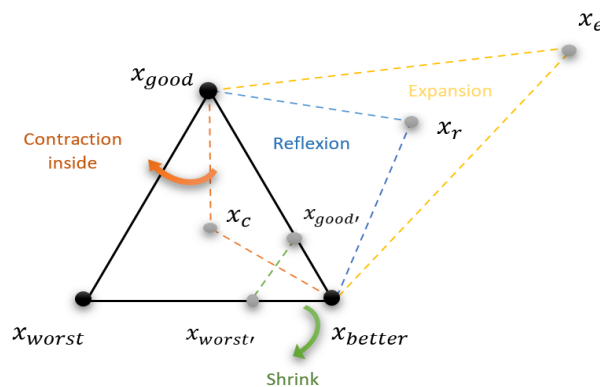
Figure 2.9.1: Illustration of the Nelder-Mead algorithm for the problem with two variables.

Each on of transformation has a scalar parameter specified in the method: coefficient of refection (ρ), expansion (χ), contraction (γ) and shrinkage (σ). The parameters are fixed with the values $\rho = 1$, $\chi = 1$, $\gamma = \frac{1}{2}$ and $\sigma = \frac{1}{2}$. [57] [62] [77] [78] [79]

Table 2.9.1 explains each of the Nelder-Mead algorithm transformations in detail. It also indicates the conditions to be validated in each step, as well as the result obtained from each one of them.

Step	Description
Sorting	Sort n+1 vertices in ascending order $f(V_{best}) < f(V_{good}) < \cdots < f(V_{worst})$.
Reflexion	Calculate the reflexion point according to the equation $x_r = (1 + \rho)\bar{V} - \rho V_{worst}$. If $f(V_{best}) < f(x_r) < f(V_n)$, replace the worst vertice with x_r. Otherwise go to the step "Expansion".
Expansion	If $f(x_r) < f(V_{best})$ compute the expansion point according to the equation $x_e = (1 - \chi)\bar{V} + \chi x_r$. Case $f(x_e) < f(x_r)$, replace the worst vertice with x_e. Otherwise replace the worst point with x_r and go to the next iteration.
Contraction	In the case $f(x_r) < f(V_{worst})$, can be performed two diferente types of contraction: inner contraction or outer contraction. a) Outer contraction: if $f(x_r) > f(V_n) > f(V_{best})$ but $f(x_r) < f(V_{worst})$ perform the outer contraction with the equation $x_{oc} = (1 - \gamma)\bar{V} + \gamma x_r$. If $f(x_{oc}) < f(x_r)$ replace the worst point with the value of x_{oc}. Otherwise calculate the shrink point. b) Inner contraction: if $f(x_r) > f(V_{worst})$ calculate the inner contraction point with the equation $x_{ic} = (1 - \gamma)\bar{V} + \gamma V_{worst}$. If $f(x_{ic}) < f(V_{worst})$ replace the worst point with x_{ic} and go to other iteration. Otherwise, perform the shrink point.
Shrinkage	Compute the equation $V = \bar{V} + \sigma(V_i - V_{best})$ for all the vertices beetween V_{good} until V_{worst}. The vertices of the simplex in the next iteration will be replaced by the new points.

Table 2.9.1: Description of the Nelder-Mead Algorithm steps.

For a better understanding and visualizing the algorithm in a graphical form, Figure 2.9.2 presents the flowchart. In order to highlight each one of the transformations, similarly to Figure 2.9.1, different colours were used for each step.
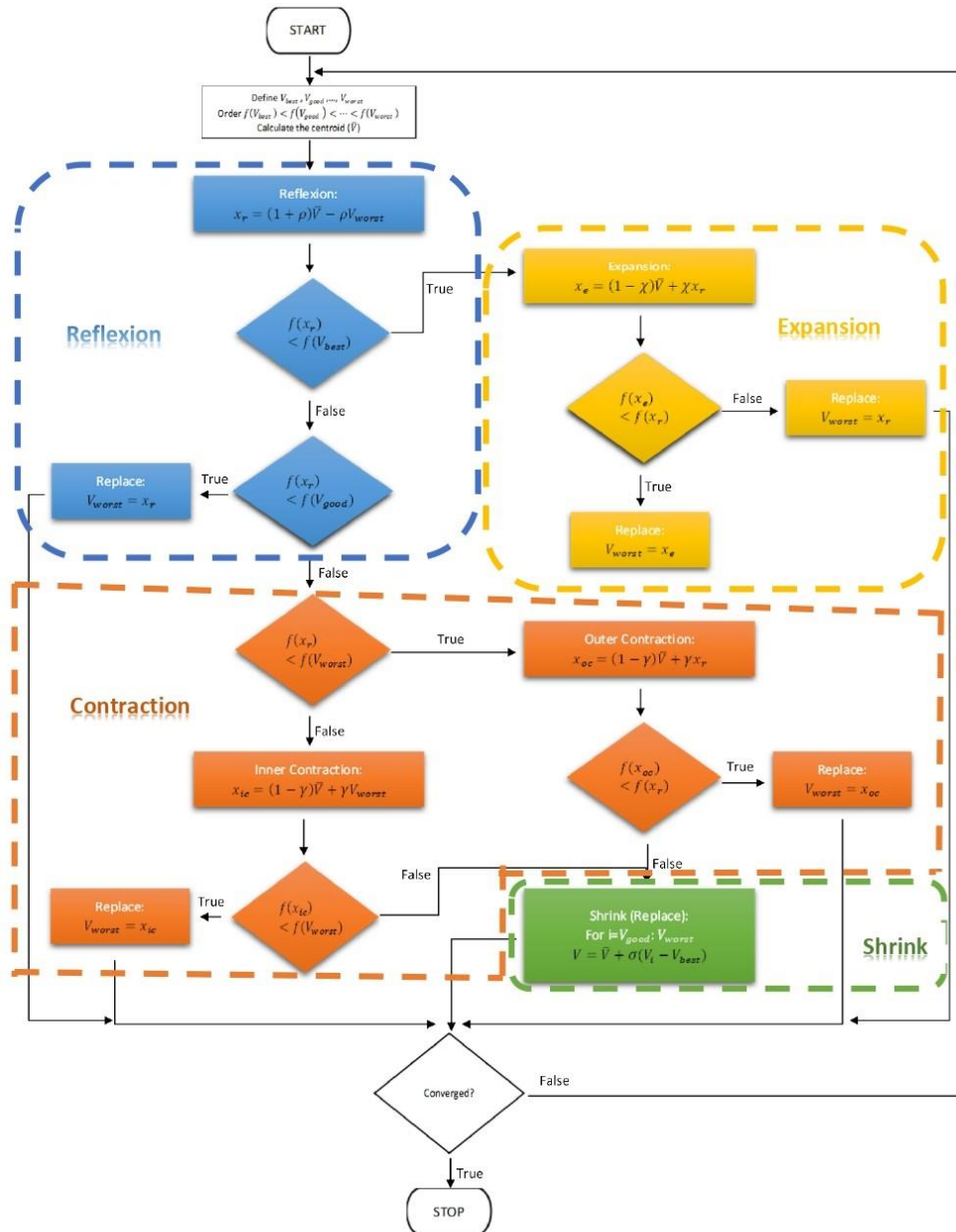
Figure 2.9.2: Nelder-Mead algorithm flowchart.

Legend of the Figure:

$\bar{V}$ – Value of the centroid; $f(V_n)$ – Value of the function in the point n; ρ – Reflexion coefficient; χ – Expansion coefficient; γ – Contraction coefficient; σ – Shrink coefficient

Simplex vertices and operations:

V_{best} – The best point value; V_{good} – The second-best point value; V_{worst} – The worst point value

x_r – Reflected value; x_e – Expandeed value; x_{oc} – Outer contracted value; x_{ic} – Inner contracted value; V - Shrink value calculated for all vertices except the best vertex.

Different studies have been done on the *Nelder-Mead algorithm*. In order to improve its convergence performance to the global minimum value, modifications have been made to the algorithm at the convergence criterion level and in this work, we will also propose a change to its algorithm initialization criterion. [62] [79]

There are different cost functions that quantify the differences between measurements and estimated values that will be minimised. The most used cost function, and also applied in this work, is the Ordinary Least Squares (OLS) and is defined by the sum of squares of the vertical deviations (current) between the measured current (I_p) and estimated current values ($\hat{I}_p$), as shown in the equation (2.32). The sum of squared distances is minimized by an iterative process where, in this case, the *Nelder-Mead algorithm* is applied. On the other hand, there are more complex methods such as Total Least Squares (TLS). In this case, the characterisation is done considering both current and voltage values, once both are affected by uncertainties. [14] [80]

$$S = \frac{1}{N_p} \sum_{p=1}^{N_p} (I_p - \hat{I}_p)^2 \tag{2.32}$$

The definition of the initial simplex for the convergence of the *Nelder-Mead* method is very important. There are already several proposed solutions with improvements of the *Nelder-Mead algorithm* in that way, such as: [81] where through the GS-INMS algorithm (grid search and improved *Nelder-Mead* simplex) a search method is applied to optimise the starting point of the *Nelder-Mead algorithm*, thus being able to improve its global search capability. This same algorithm proposes an improvement in the convergence of *Nelder-Mead*; [62] suggests new convergence and simplex initialization conditions for the *Nelder-Mead algorithm*; [82] presents the application of the *Nelder-Mead* simplex method and the modified Particle Swarm Optimization technique with the purpose of identifying the parameters of a solar cell; [67] hybridization of the improved *Nelder-Mead* simplex method (NMS) with the artificial bee colony (ABC) meta-heuristic method proposes a technique to improve parameter identification in photovoltaic models.

Start Criterion

The *classic Nelder-Mead algorithm* implemented in MATLAB tool creates the initial simplex through an estimate. This estimate will be the value of one of the vertices of the simplex. For the remaining *n* vertices a perturbation will be applied to each of the coordinates of the initial guesses, following the next criteria: [83]

- If the coordinate value is non-zero, a 5% perturbation of the current value will be applied;
- If the coordinate value is zero, the coordinate value is set to 0.00025.

In the present work a new initialization criterion of the *Nelder-Med algorithm* was applied in this method. It was selected a wide range of 1000 random values located near each guess (parameters), evaluating this way which will be the value of the function at each point creating consequently the initial simplex. The search range was defined according to the order of magnitude of the parameter in question, and this range can be tuned performing a search closer or farther from the initial guess. In this way, an engine was created to start the search process.

In order to clarify the starting criteria of the method, an illustration of the process is shown in the Figure 2.9.3 applied to a generic parameter.
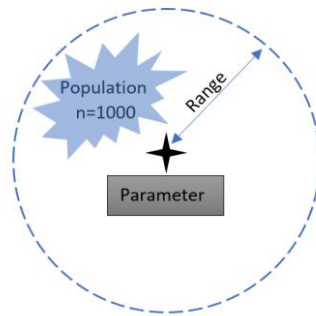
Figure 2.9.3: Starting criterion illustration of the modified Nelder-Mead algorithm applied to a generic parameter.

Convergence criterion

The classical approach of the *Nelder-Mead algorithm* has a convergence criterion focused on the absolute value of the size of the simplex, also analysing the difference between the values of the function in each vertex of the simplex that will be compared with a certain tolerance imposed. Successive iterations will be performed until the criterion satisfies the desired tolerance. [83]

In the present work, the convergence criterion was also changed. This modification implies that the cycle stops when the absolute maximum value of the distances from the vertices of the simplex to the barycentre is smaller than the imposed tolerance, as shown in the equation (2.33). Note that each interaction is necessary to calculate the value of the centroid and the distances. [57] [79]

$$Absolute\ maximum\ distance\ <\ imposed\ tolerance \qquad (2.33)$$

For a better understanding of the criterion applied, the Figure 2.9.4 shows an example for the case of a two-dimensional problem, in other words, a three-vertex simplex.
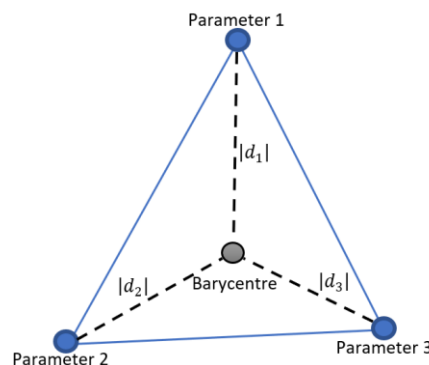
Figure 2.9.4: Stop criterion illustration of the modified Nelder-Mead algorithm.

2.10. Five parameters estimation - Simulation conditions and comparative study

In order to analyse the performance of the *modified Nelder-Mead algorithm*, the parameters of photovoltaic cells were estimated applying the developed algorithm. Simulations for performance analysis of the algorithm and comparison of results are made based on a pre-implemented function of the *classical Nelder-Mead algorithm* called *fminsearch* available in MATLAB tool.

In a simulation environment, to determine the samples and for them to be reliable, it is necessary to add Gaussian noise to the I-V characteristic curve and then apply an analogue digital converter (ADC). In this way it will be possible to obtain a digital representation generated through an analogue quantity, thus having a good replica of the experimentally measured values. [84] Note that in order to obtain a better estimate of the measured values, several measurements must be taken, and the values averaged.

Firstly, a study was carried out to identify the number of times that it would be necessary to run the algorithm. In this sense, each parameter was estimated by running the algorithm 10000 times, applying a white noise of 1%. Note that this study was done for each individual parameter, i.e., the remaining four are fixed. A moving average was then applied to the results obtained to make the graphs shown in the Figure 2.10.1.

(a)

(b)

(c)

(d)

(e)
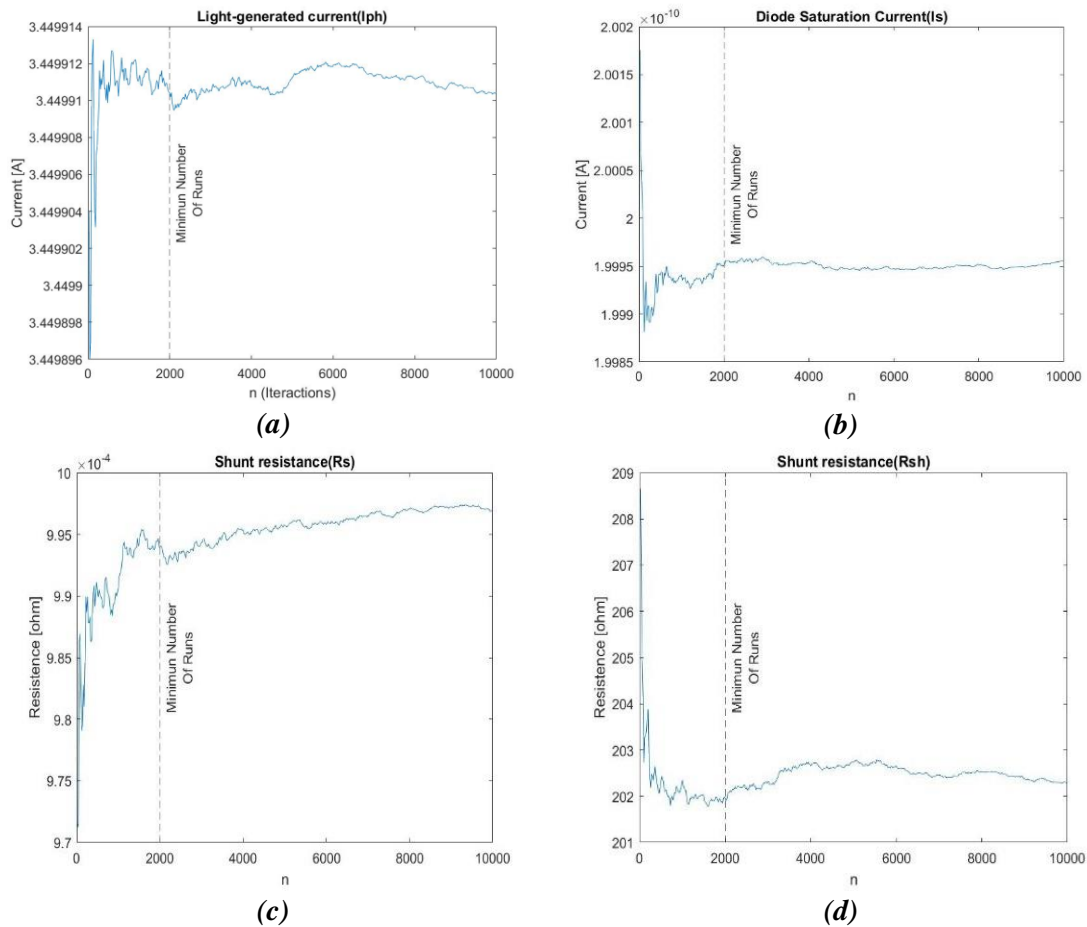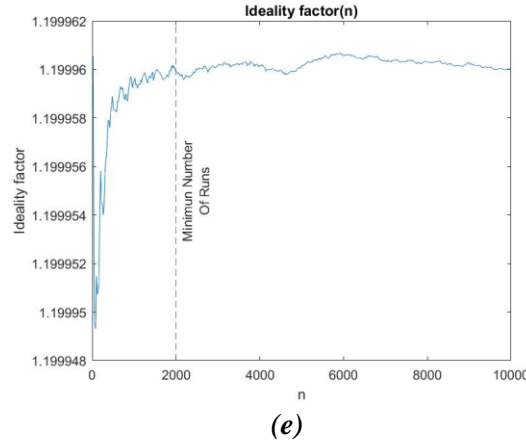
Figure 2.10.1: Figure 2.10.1: Minimum number of runs for each parameter. (a) Iph parameter (b) Is parameter (c) Rs parameter (d) Rsh parameter (e) n parameter

The moving average is an estimator calculated from sequential samples of the population. Given a sequence of local mean values, each mean is calculated over a sliding window of given length *k* (in this case set to the value 20) through neighbouring elements of the vector. [85]

Making a detailed analysis of each of the graphs in Figure 2.10.1, it can be seen that the parameters tend to stabilise at 2000 runs, which means that the developed algorithm must have been applied at least 2000 times, thus obtaining reliable values. In order to highlight the moment when stability is reached for each parameter, a dashed line was drawn on each one of the graphs.

The aim of the next simulations is to analyse the convergence of the proposed *Nelder-Mead algorithm* with the *classical Nelder-Mead algorithm* implemented in the MATLAB tool. The study of the performance of both algorithms results from the extraction of the mean and standard deviation obtained by performing 2000 simulations. In these simulations Gaussian white noise was added, varying its percentages from 0.1% to 10%.

Both algorithms were exposed to the same convergence tolerance, same noise, initial conditions, and the optimal parameters used in simulation environment are shown in the Table 2.10.1.

Parameter	Value
I_{ph}	3,45 [A]
I_s	$2 \times 10^{-10}[A]$
R_s	0.001 [Ω]
R_{sh}	200[Ω]
n	1,2

Table 2.10.1: Optimal parameters used in simulation environment.

After performing the simulation, the graphs of the Figures 2.10.2 e 2.10.3 were obtained. These graphs represent the mean of the five parameters as a function of the noise percentage value added. The blue curve represents the *classical Nelder-Mead algorithm* while the red curve shows the results referring to the *modified Nelder-Mead algorithm*.
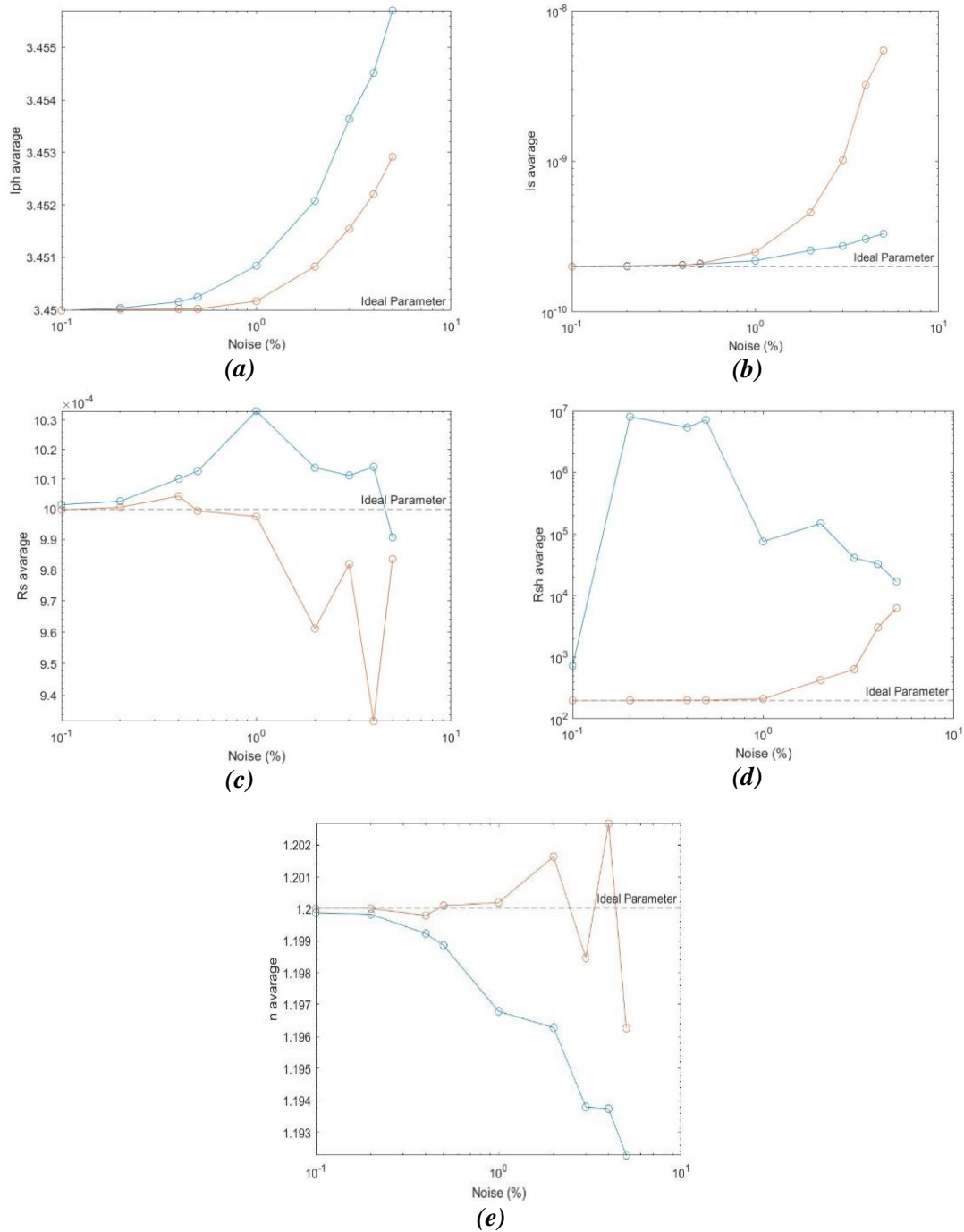
Figure 2.10.2: Mean Values of the Parameters Cell versus current noise. In red the modified Nelder-Mead algorithm and in blue the classical Nelder-Mead algorithm. (a) Iph parameter (b) Is parameter (c) Rs parameter (d) Rsh parameter (e) n parameter

In Figure 2.10.2, in general, the red curves are closer to the ideal value, and the lower the noise value, the closer the estimate is to the ideal value. The I_s parameter is the one that shows a distinct behaviour. However, as will be verified in Chapter 3, this difference does not have much influence in the maximum power point calculation.

The studied effect is also shown in the graphs of the Figure 2.10.3. These graphs analyse the problem from the standpoint of standard deviation.
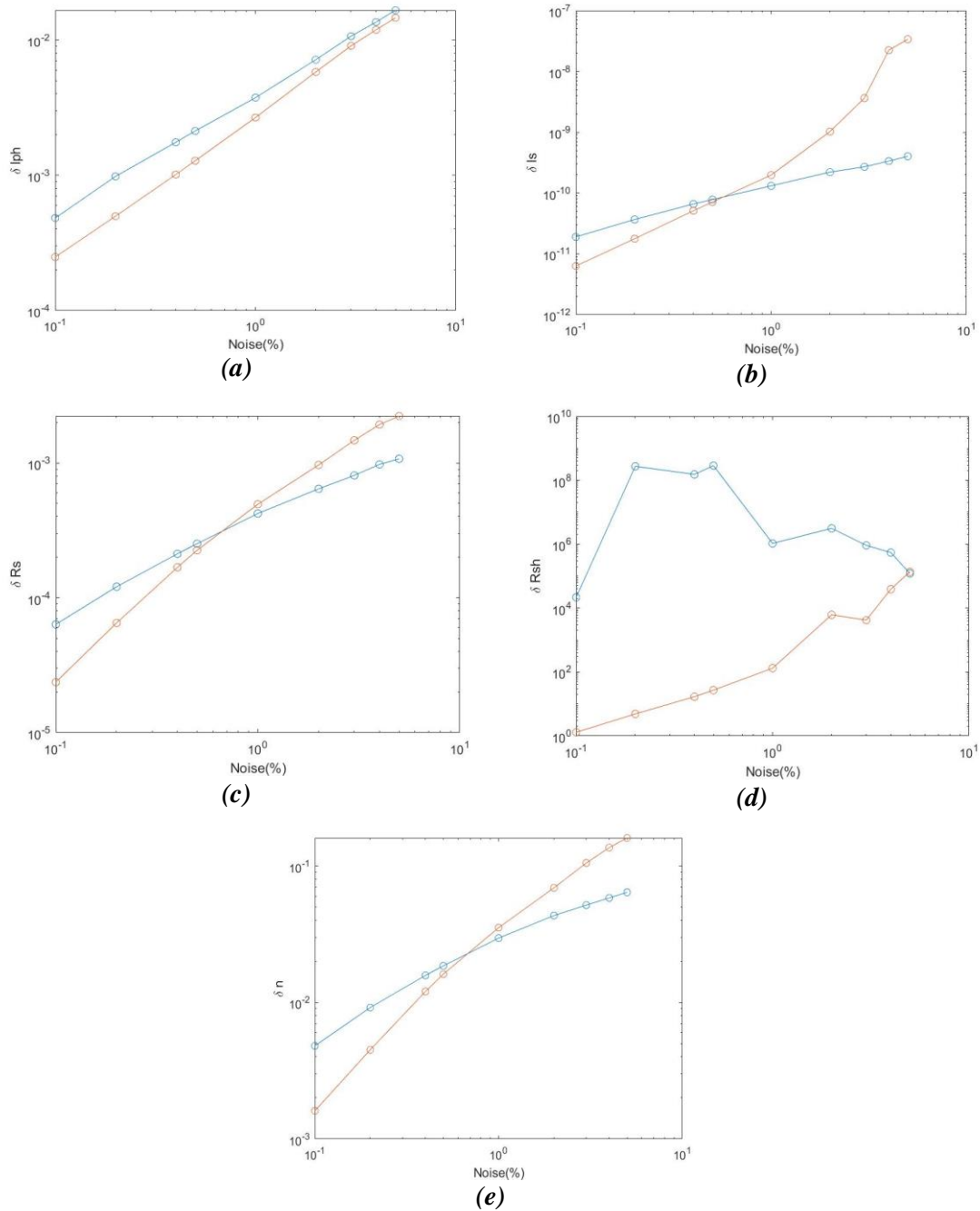
Figure 2.10.3: Standard Deviation of the Parameters Cell versus current noise. In red the modified Nelder-Mead algorithm and in blue the classical Nelder-Mead algorithm. (a) Iph parameter (b) Is parameter (c) Rs parameter (d) Rsh parameter (e) n parameter

According to the graphs in Figure 2.10.3, for small percentages of added noise, the lower the value of the standard deviation will be. Analysing the graphs, can be seen that, in this sense, the parameter I_s follows the same pattern, that is, for small values of noise, the *modified Nelder-Mead algorithm* presents a better performance. One of the parameters whose results stand out is the shunt resistance (R_{sh}) which will be studied in detail later in the "Sensitivity Analysis" and "Parameters Analysis Platform" section.

2.11. Sensitivity Analysis

The RMSE is the criteria to quantify the difference that exist between the results of the model of the single-diode (equation 2.25) and the measured data. RMSE means root mean square error and is calculated with the expression (2.34) and in the same way than the expression (2.32), for each pair of experimental values (I,V) it give us the difference of calculated measured data and real measurement current. [77]

$$RMSE = \sqrt{\frac{1}{N_p}\left(\sum_{p=1}^{N_p}(I_p - \hat{I}_p)^2\right)} \tag{2.34}$$

Using the root mean square error it is possible to study the sensitivity of each parameter. The sensitivity analysis is very important to be done because the convergence of the *Nelder-Mead algorithm* will depend on the choices made for the guesses of the initial simplex vertices. This analysis allows to identify if the approximation should be made from upwards or downwards, thus avoiding that the algorithm gets stuck. This topic will be studied in more detail in section "Parameter Analysis Platform".

Thus, for a 1% white noise, the RMSE value for each parameter was generated 2000 times. The graphs in Figure 2.11.1, for each parameter, display the average RMSE value obtained. In this way, it is possible to obtain the minimum value of the curve that corresponds to the average value of the parameter. In addition to the average value, the standard deviation can be studied by knowing the minimum value of the parameter reached in each of the 2000 iterations performed.

Table 2.11.1 shows the confidence intervals obtained through the graphs in Figure 2.11.1.

Parameter	*Confidence Interval*
I_{ph}	$[3.45 \pm 0.0045]$ [A]
I_s	$[2 \times 10^{-10} \pm 1.2214 \times 10^{-12}]$ [A]
n	$[1.2 \pm 3.3353 \times 10^{-4}]$
R_s	$[0.001 \pm 2.2755 \times 10^{-4}]$ [Ω]

Table 2.11.1: Confidence interval of each parameter

Table 2.11.1 shows the confidence interval for each parameter. A confidence interval is defined as an interval estimation used in statistics, which contains a population parameter. This unknown population parameter is found by means of a sample model calculated from the data collected. The confidence interval is important to indicate the margin of uncertainty (or inaccuracy) regarding a calculation made. This calculation uses the study sample to estimate the true size of the result in the source population. Thus, the confidence interval is interpreted as follows: it is 95% confident that the interval between X (lower limit) and Y (upper limit) contains the true value of the population parameter. [86]
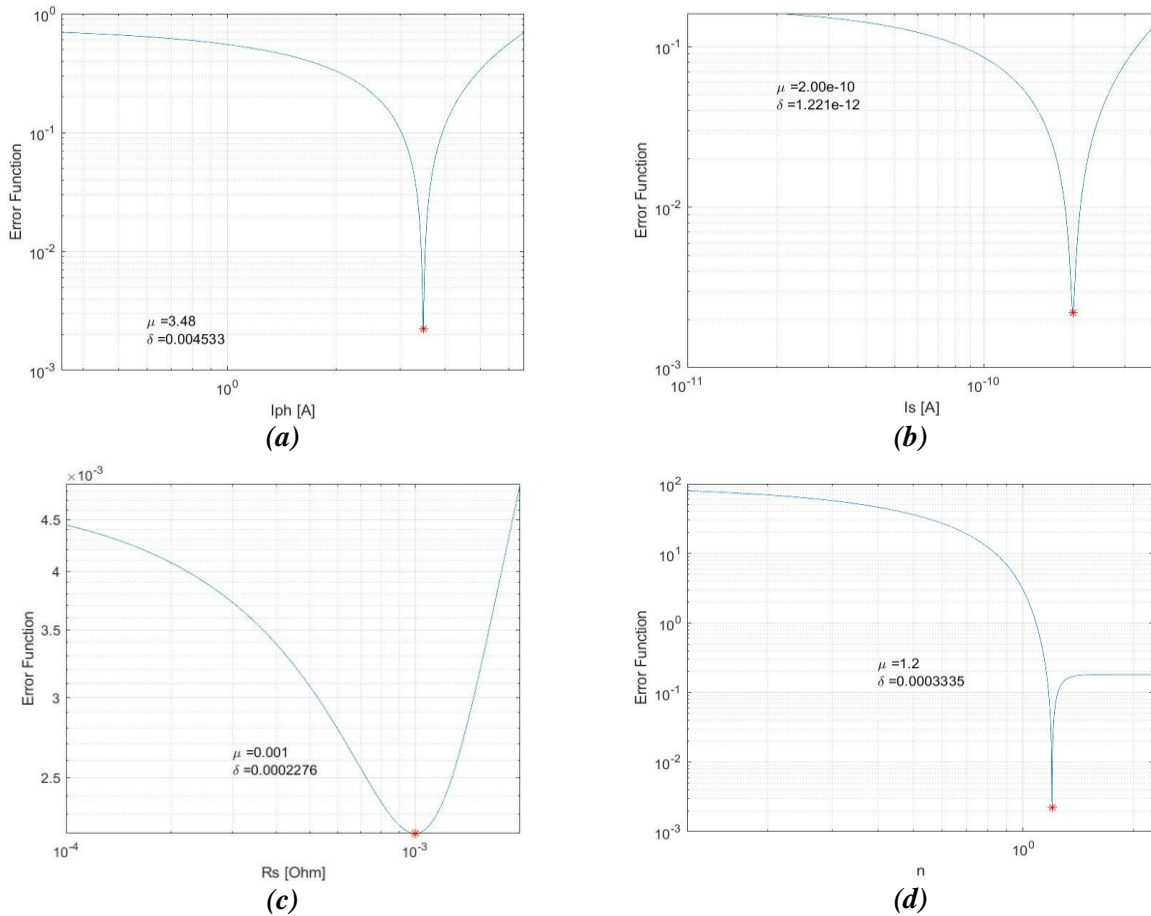
Figure 2.11.1: Individual sensitivity analysis. (a) Iph parameter. (b) Is parameter. (c) Rs parameter. (d) n parameter

The results obtained can also be shown as a histogram. A histogram consists of a bar graph demonstrating a frequency distribution, where the base of each one of the bars represents a class, and the height the amount or absolute frequency with which the class value occurs. At the same time, it can be used as an indicator of process dispersion.

Above all, it aims to illustrate how a certain data sample or population is distributed, arranging the information in a way that makes it easy to visualise the distribution of the data. At the same time, it highlights the location of the central value and the distribution of data around this central value.

Thus, it has two axes with different functions, where the horizontal axis is divided into small intervals, showing values assumed by the variable of interest. The vertical axis is proportional to the frequency of observations of the sample where the values belong to that class or interval.

For each of the parameters, a histogram was made with the values obtained, where it is possible to analyse in more detail which value was obtained more frequently. The results are shown in Figure 2.11.2.
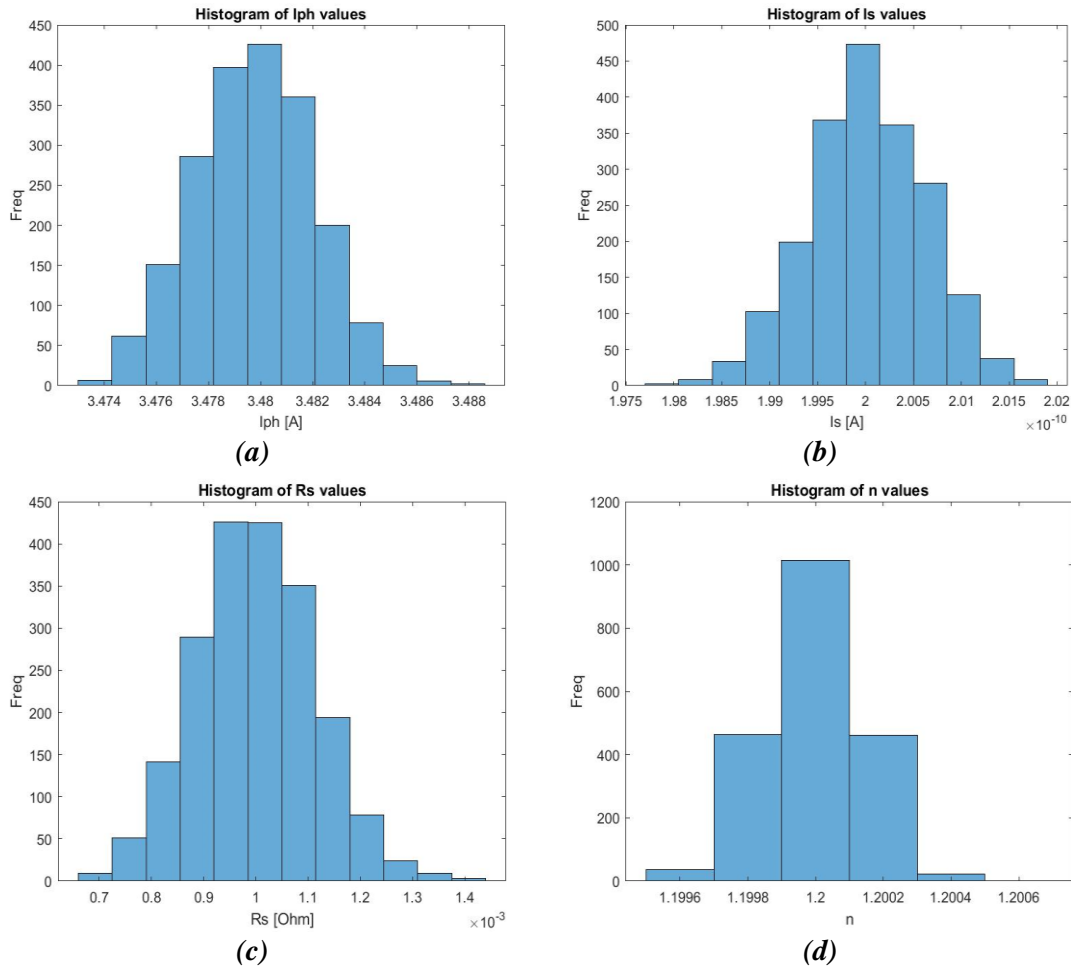
Figure 2.11.2: Histogram of minimum values achieved at each iteration. (a) Iph parameter. (b) Is parameter. (c) Rs parameter. (d) n parameter.

In the graphs of the Figure 2.11.2, it can be seen there is a symmetry in the data of each one of the histograms. This type of histogram has a higher frequency in the centre, which is the most frequent value for each parameter. The variations go down symmetrically on both sides. It is a standardized process where the data is stable and there are small variations.

Another important aspect to study is the effect that noise has especially on the R_{sh} parameter.

As can be seen in the Figure 2.11.3 corresponding to the shunt resistance, the variation of the white noise significantly affects the behaviour of the parameter, thus obtaining quite distinct sensitivity curves. In this way, it is also possible to define the minimum average value for this parameter which will vary according to the noise percentage.

Table 2.11.2 was filled according to the values obtained in the simulations that are in the graphs of Figure 2.11.3.

White Noise	*Minimum Average Value* [Ω]	*Minimum number of runs*
10%	173.92	3000
1%	199.07	3000
0.1%	200.08	2000

Table 2.11.2: Confidence interval of Shunt Resistance varying the white noise.

(a)

(b)

(c)
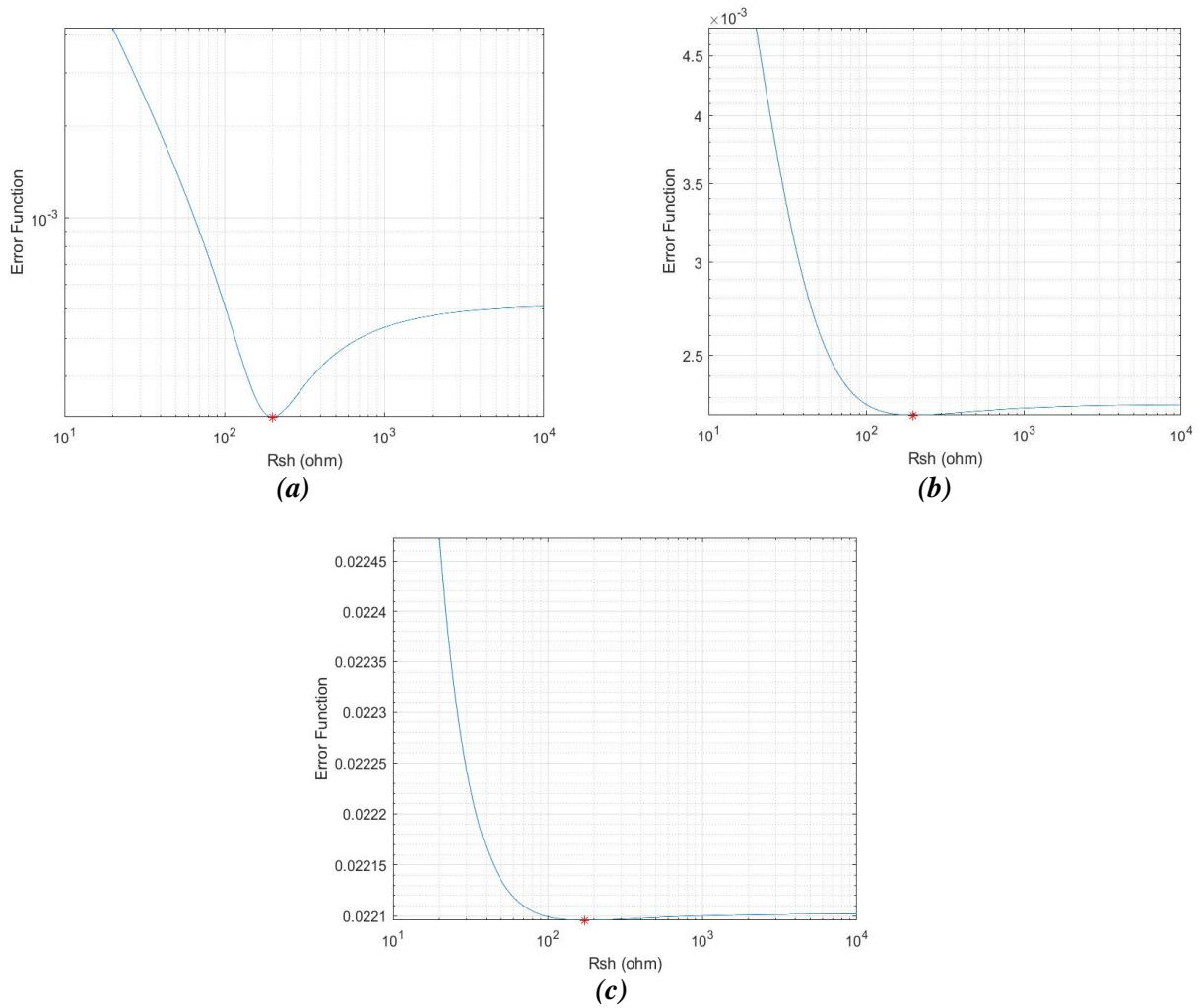
Figure 2.11.3: Sensitivity analysis for shunt resistance for different noise percentages. (a) Shunt Resistance with the 0.1% noise. (b) Shunt Resistance with the 1% noise. (c) Shunt Resistance with the 10% noise

By analysing Table 2.11.2 and the Figure 2.11.3, it can be seen that the higher the noise percentage, the more runs are needed to obtain reliable values. On the other hand, we see that the average value of the shunt resistance approaches the ideal value with less added noise. The conclusion is that for low noise percentages, the smaller the shift in the error function curve.

2.12. Parameters Analysis Platform – Graphical User Interface

A Graphical User Interface (GUI) is a computer program that uses a set of images and graphical objects to represent the actions and information available on the interface. Its main function is to provide a simple visual environment that allows communication between two systems that do not use the same language. [87]

It emerged as an evolution of the command line interfaces (CLI) used in early operating systems and is a fundamental part of most electronic devices used today.

The characteristics of an efficient interface are described in the diagram of the Figure 2.12.1.
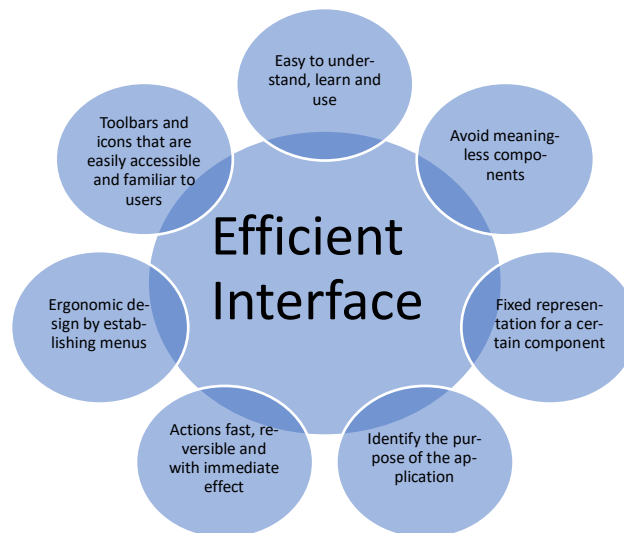
Figure 2.12.1: Efficiency of a graphical user interface.

MATLAB (short for "MATrix LABoratory") is a mathematical software tool widely used in universities and research and development centres.

This software has its own programming language (M language) which allows the user to operate with arrays, represent data and functions, implement algorithms, create user interfaces (GUIs) and communicate with programs in other languages and with other hardware devices. Additional applications such as Simulink (simulation platform), GUIDE and App Designer (user interface editors) are included. In addition, MATLAB functionality can be enhanced with toolboxes, and Simulink functionality can be enhanced with block set applications. [87]

The MATLAB package currently has three methods for creating user interfaces: [88]

- MATLAB functions.
- GUIDE.
- App Designer.

Each of these alternatives offers a different way of working, as well as a slightly different set of functionalities. The choice of one method or the other depends on the objectives of the project and the way the developer is used to working of the interface.

App Designer is a graphical interface development environment introduced in R2016a, includes a fully integrated version of the MATLAB editor. In this case, the design and code views are closely linked, so that changes made in one immediately affect the other. [87] [88] [89]

This tool seeks to continue with the trend of reducing the time needed to develop interfaces, as well as to facilitate their design. In this sense, it is important to highlight that this work environment optimises the way of programming with respect to that used in GUIDE, as it facilitates access to the properties of the components, the declaration of call-backs and the way of sharing information between these components. [89]

As mentioned, App Designer does not have all the graphical features of MATLAB, nor does it have menus and toolbars, but it does have a wider set of interactive controls, including meters, lamps and switches to create a more visually appealing interface for the user. [89]

The application created in the App Designer can be shared with other users for use in both MATLAB desktop and MATLAB online. It can also be installed in the applications tab or shared with non-MATLAB users. For users without MATLAB, you must use the MATLAB compiler. [88]

Using the App Designer tool was created a versatile numerical and simulation platform for optimal characterization purposes. It is a decision support system software applied to the estimation of the parameters of the photovoltaic cell. The platform's main menu is shown in Figure 2.12.2, where from this screen it is possible to navigate through the three different screens that are part of the platform: screen for parameter estimation; screen for parameter analysis; screen for parameter cost analysis.
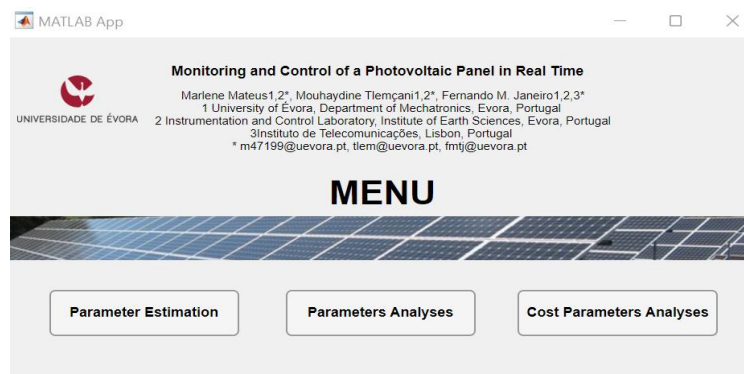
Figure 2.12.2: Menu Screen.

In the base of the platform is applied the *modified Nelder-Mead algorithm*, which allow to search for an optimal performance of a photovoltaic cell. The basic behaviour of the application is shown in the flowchart in Figure 2.12.3.
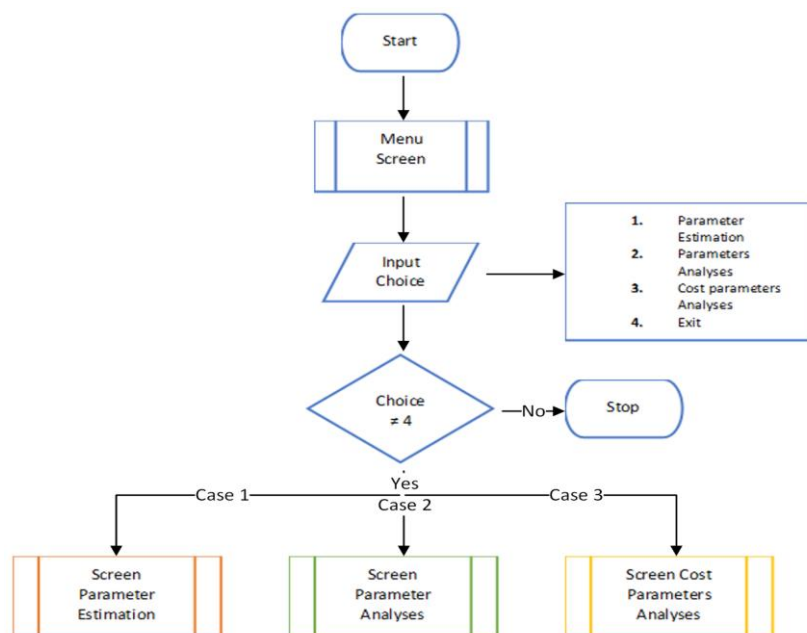
Figure 2.12.3: Flowchart of the menu screen.

Screen 1 - Parameter Estimation

The "Parameter Estimation" screen allows the estimation of two parameters simultaneously and in real time. This screen lets the ideal parameters to be entered in order to create virtual samples with the corresponding voltage and current measurements. To determine the samples and to make them reliable, it is necessary to add Gaussian noise to the I-V characteristic curve and then apply an analogue digital converter. In this way it will be possible to obtain a digital representation generated by an analogue quantity, thus having a good replica of the experimentally measured values.

The graph of the Figure 2.12.4 shows the level lines of the cost function and the simplex composed of three vertices (triangle) converging to the minimum value, which means that the estimation is done with two parameters simultaneously. This minimum point can be visualized through the contour plot.
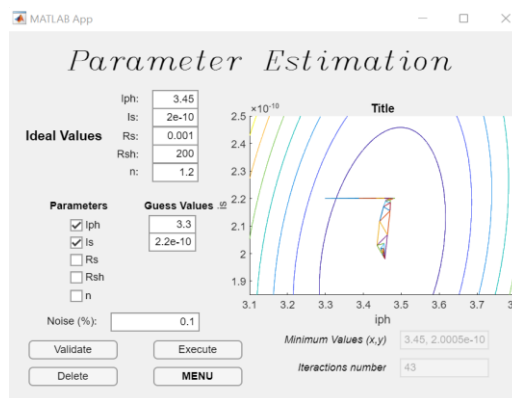
(a)
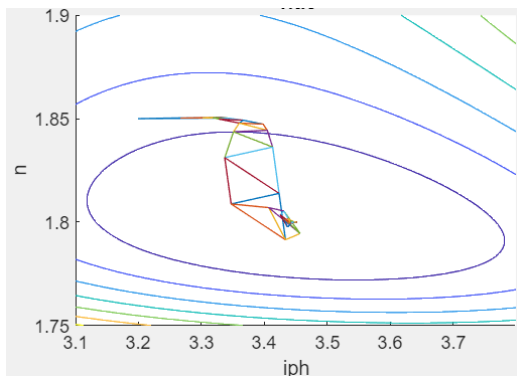
(b)
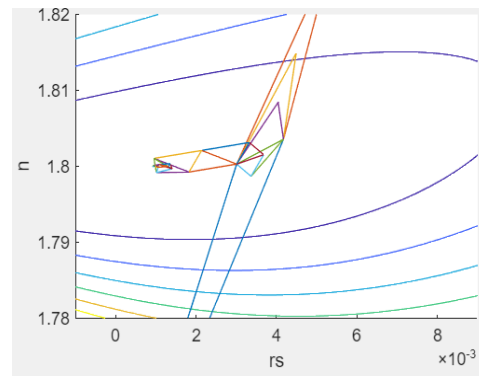
(c)

Figure 2.12.4: Parameter estimation screen. (a) Parameter Is e Iph estimation. (b) Parameter n e Iph estimation. (c) Parameter n e Rs estimation.

The Figure 2.12.4 shows the screen referring to the parameter estimation where three different demo tests were performed in order to demonstrate the operation of the application. Given the physiognomy of the application, it is necessary to be careful with the ideal values assigned to the parameters as well as the respective guesses, because the graph may not be presented as expected and the hole may not be visible. Additionally, there is a field where the user can

check the minimum value reached as well as the number of iterations required. The Figure 2.12.5 shows the flowchart for the "Parameter Estimation" screen.
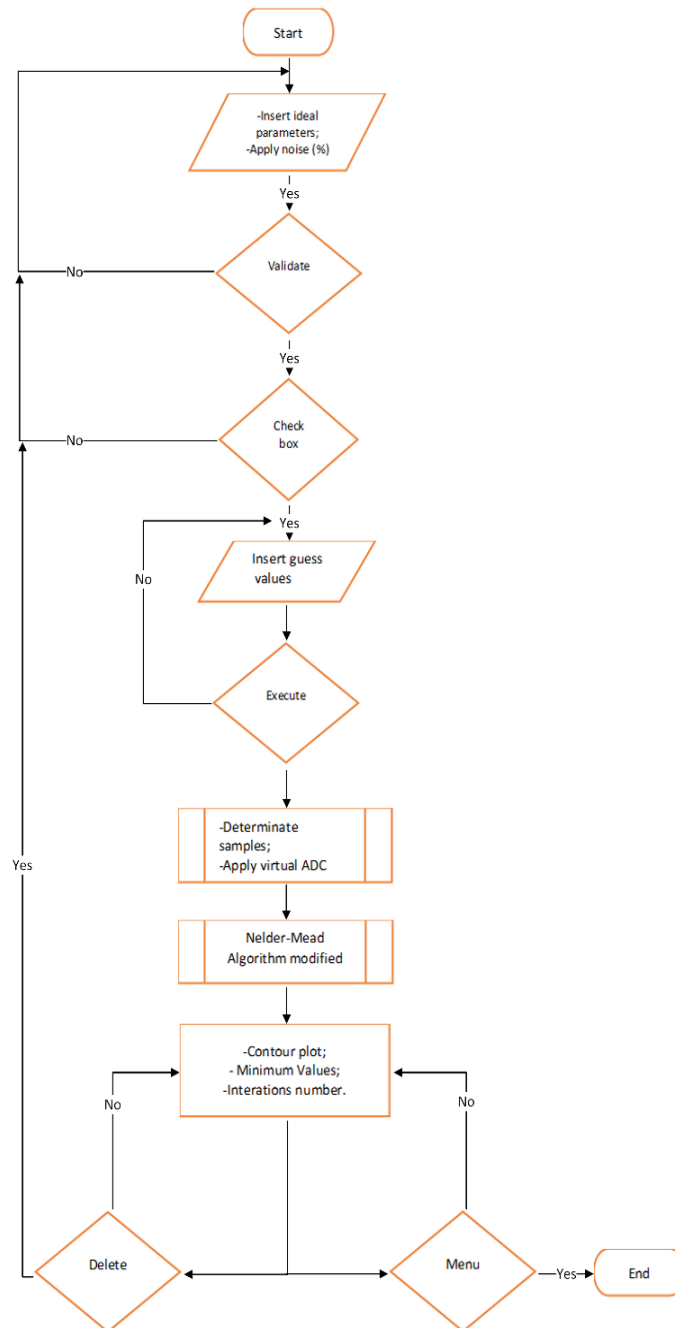
Figure 2.12.5: Flowchart of the "Parameter estimation" screen.

Screen 2 – Parameters Analyses

The "Parameter analyses" screen allows an individual analysis to be made of each parameter. The interface allows to know the behaviour of the error function applying (or not) a certain percentage of white noise.

This screen helps to study the impact that each parameter has in specific circumstances, for which a sensitivity analysis is carried out. Sensitivity analysis is a common methodology which aims to find the uncertainties in any evaluation, verify the impact that each parameter has on the process and the consequences that certain assumptions may have. [90]

The sensitivity analysis is tested using the RMSE equation (described in (2.25)), which results in the difference between the standard condition for the different variable conditions in which the parameter changes, as shown in the scheme in the Table 2.12.1. This process helps in identifying the sensitivity of parameters whether they are internal or environmental. These parameters are closely related to the photovoltaic cell and affect its performance. In the present work the five internal parameters of the photovoltaic model ($P = [I_{ph} \quad I_s \quad R_s \quad R_{sh} \quad n]$) were studied. With this analysis the quality of the model can be improved allowing for a better power extraction from the PV system. [91] [92]

Step	State	Description
1	Input	Parameter to analyse (P_1)
2	Input	Fix the remaining parameters (O_n)
3		Generate the simulated samples
4		Generate an array with parameters changes
5		for *i=1* to *n* $$RMSE_p = \frac{1}{n}\sqrt{\sum_{i=1}^{n}(I_i - \hat{I}_i)^2}$$ end
6	Output	Graphic error function versus parameter
7	Output	Nelder-Mead algorithm modified convergence animated

Table 2.12.1: Summary algorithm of the sensitivity analysis.

The Figures 2.12.6 – 2.12.11 present examples of sensitivity test performed to each parameter, where in the first graph is the error function that shows the behaviour of the output accurately. An animation based on the *modified Nelder-Mead algorithm* is also applied to the graph, where the convergence process towards the minimum value can be seen. The second graph on the screen shows the problem from a financial perspective. For this, there are fields that must be filled in: the farm power, the panel power, the number of cells, the number of hours it is in operation and the KWh value. In general, the closer the ideal value of the parameter in study is, the lower the cost losses will be.

Photocurrent

The Figure 2.12.6 show the behaviour of power generation varying the values of the photocurrent where the value of the parameter is varied between 0.345A and 6.555A. Thus, it is possible to generate the graph that shows the sensitivity of the parameter referring to the photocurrent.
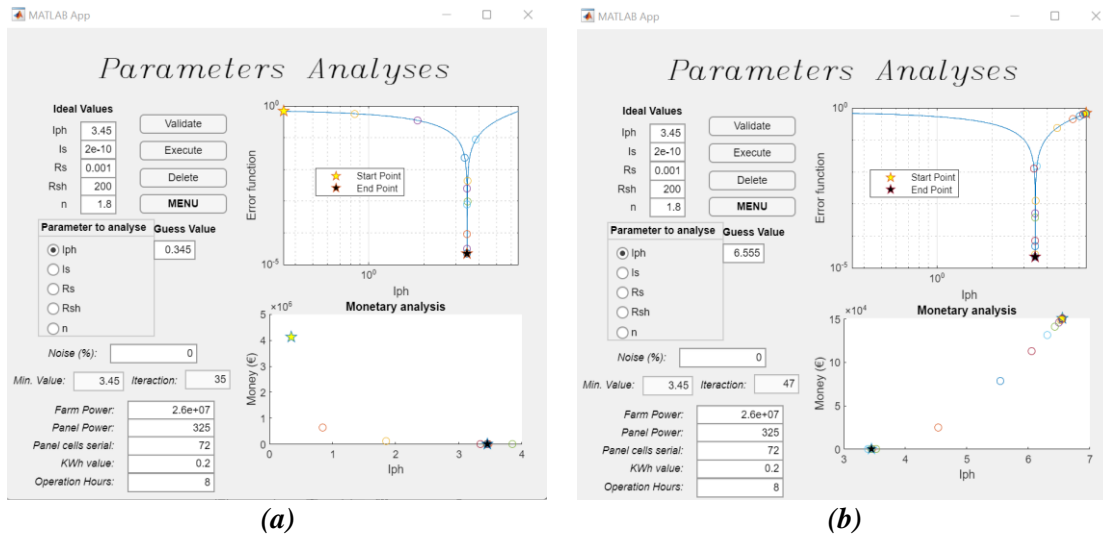
Figure 2.12.6: Photocurrent parameter analyses. (a) Approaching from the left. (b) Approaching from the right.

For easier analysis, both axes of the graphs are drawn on a logarithmic scale. The current values vary constantly, and the curve can be divided into two parts: one part to the right of the optimum value and another to the left of the optimum value. By analysing the Figure 2.12.6 (a) and (b), it can be concluded that the value of the I_{ph} parameter should be underestimated, as the optimum value is reached with a smaller number of iterations.

Saturation current

The saturation current is one of the parameters belonging to the five-parameter single diode model. The graphs 2.12.7 (a) and (b) show the error function applying different values of saturation current, these values varying between 2×10^{-11}A e 3.8×10^{-10}A.
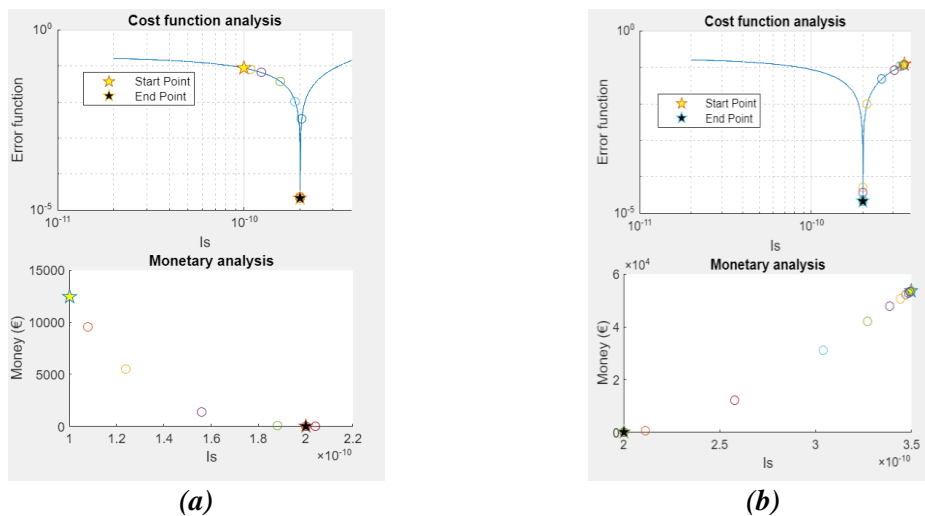
Figure 2.12.7: Saturation current analysis. (a) Approaching saturation current parameter from the left. (b) Approaching saturation current parameter from the right.

As observed in both graphs (2.12.7 (a) and (b)), the curve is divided in two parts: the left part at the optimal value and the right part at the optimal value. In order to obtain convergence with a smaller number of iterations, an estimation should be made on the left of the optimal value. However, one must be careful with this estimate, because if the initial value (guess) is too far from the optimal value, there is the risk of being in the flat zone and the algorithm does not converge.

Serial Resistance

The series resistance was also used to calculate the error function. To do so, a range of values was applied and the resistance value was varied, and for the case in the graphs of the Figure 2.12.8, the resistance was varied approximately between 0.0001 Ω and 0.002 Ω.
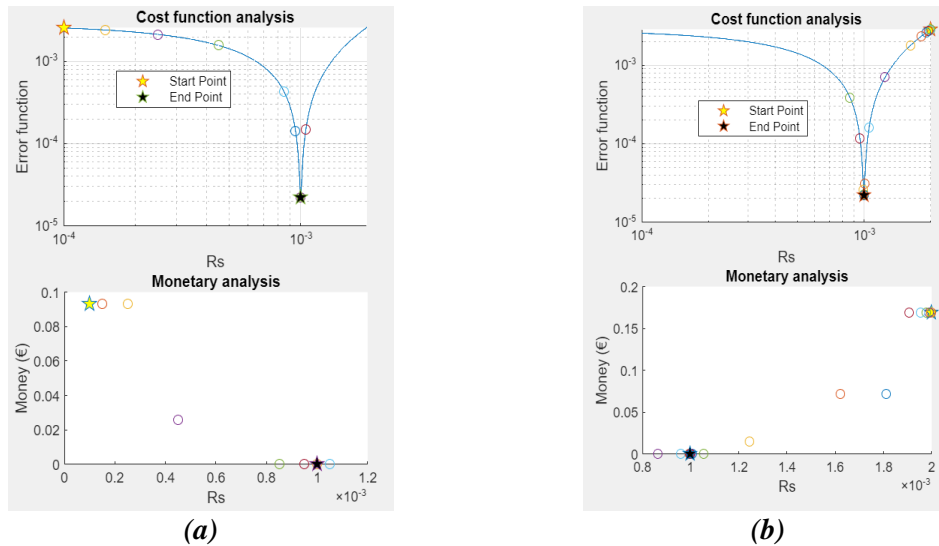
Figure 2.12.8: Serial resistance parameter analyse. (a) Approaching serial resistance parameter from the left. (b) Approaching serial resistance parameter from the right.

As for the previous parameters, the series resistance also has its curve divided into two parts separated by the optimum value. In order to obtain a faster estimation and with a lower number of iterations, according to the graphs analysis in the Figures 2.12.8 (a) and (b) the initial guess should be underestimated.

Diode Ideal Factor

The ideal factor of the diode is another parameter that its sensitivity analysis is done. This parameter is between the values 1 and 2 and its analysis is shown in the Figure 2.12.9.
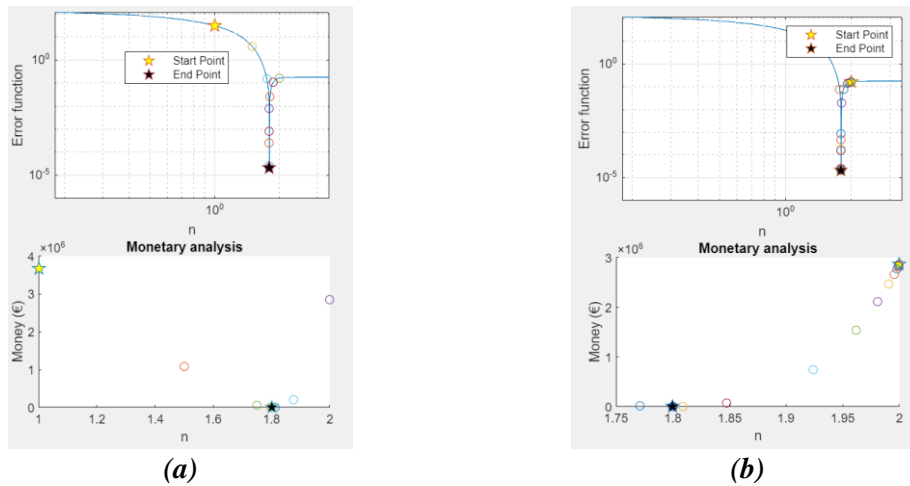
Figure 2.12.9: Diode ideal factor parameter analyses. (a) Approaching diode ideal factor parameter from the left. (b) Approaching diode ideal factor parameter from the right.

As in most previous studies, in the graphs 2.12.9 relating to the sensitivity analysis of the optimal diode factor both axes are on a logarithmic scale. The curve is divided into two parts separated by the optimum value. It can be seen that the left-hand side of the curve allows faster convergence to the optimum value, and therefore the parameter should be underestimated. Regarding the right side of the curve, if the estimation is done from this side, it is necessary to be careful, because there is a flat area which may lead to a non-convergence of the algorithm.

Shunt Resistance

The sensitivity of the shunt resistance is also studied. This parameter was identified as the most difficult to analyse, because unlike the others whenever a percentage (either big or small) of white noise is applied, the function error will suffer significant changes.
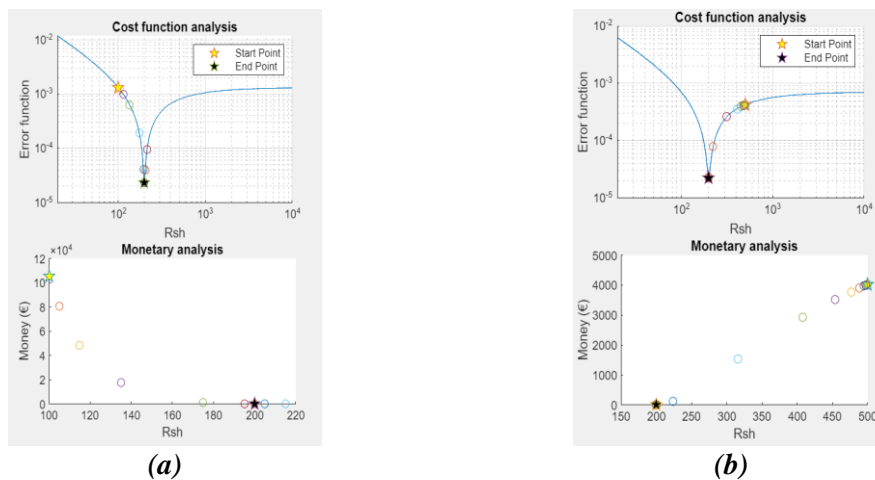
Figure 2.12.10: Shunt Resistance parameter analyses. (a) Approaching Shunt Resistance parameter from the left without noise. (b) Approaching Shunt Resistance parameter from the right without noise.

No noise was applied to the graphs in the Figures 2.12.10 (a) and (b), so it is possible to verify that this curve has a behaviour similar to the others, in other words, it is divided into two parts, separated by the optimum value. By graphical analysis it can be concluded that the approximation should be made from the left, which is faster. However, do not forget that this rule should not be followed when there is noise in the system as shown in the Figure 2.12.11.

(a)

(b)

(c)
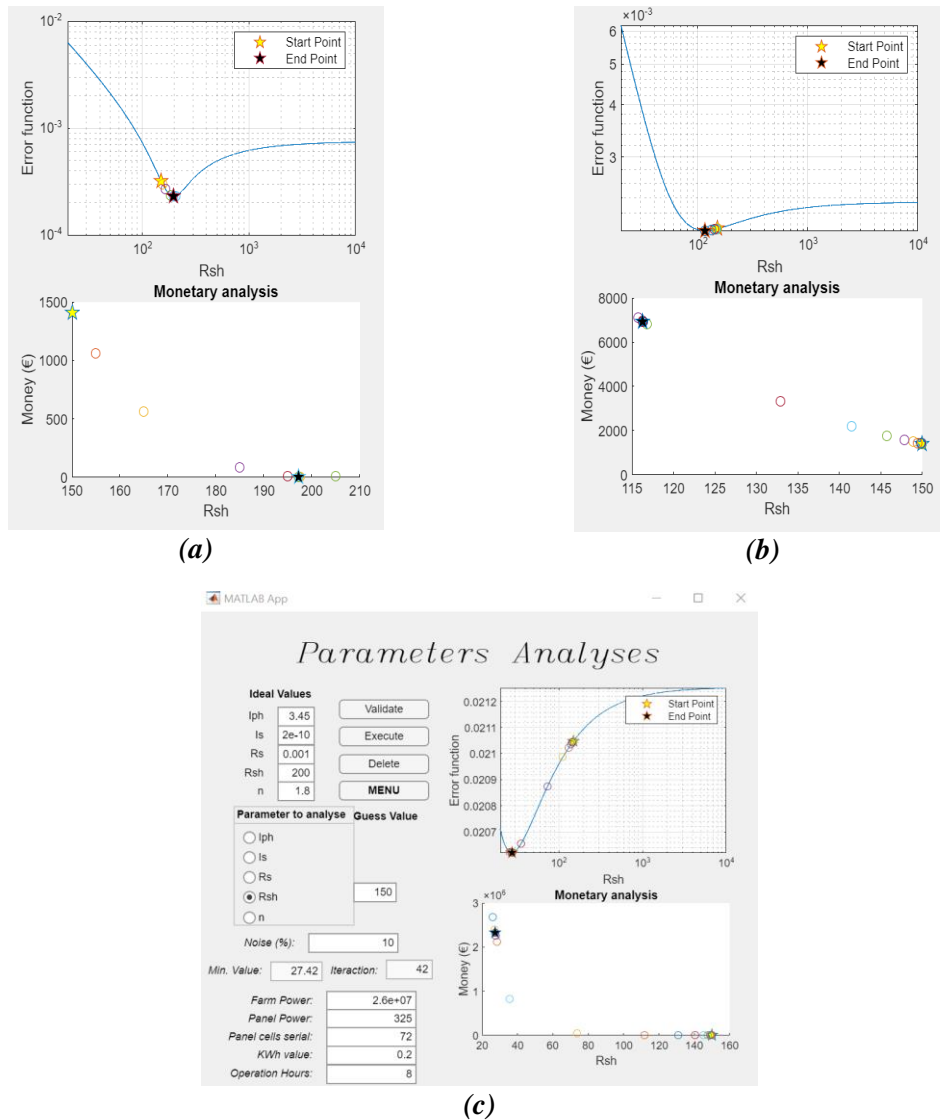
Figure 2.12.11: Shunt Resistance parameter analyses with noise. (a) 0.1% (b) 1% (c)10%

The graphs (Figure 2.12.11 (a)-(c)) show how noise can influence the shunt resistance estimate, for the current example some graphs were generated where a percentage of 0.1%, 1% and 10% of noise was added. The higher the noise percentage, the more unstable is the curve and consequently the more distant from $R_{sh} = 200\Omega$ (ideal value) the estimate will be.

As proof, it is highlighted the example where 10% of noise was added to the system (Figures 2.12.11 (c)). For the same ideal value of parameters and the same guess, a quite different curve was obtained with different estimates. Given this uncertainty and differentiability it is difficult to identify on which side of the curve the approximation to the optimal value should be made.

Figure 2.12.12 shows the flowchart for the "Parameter Analyses" screen.
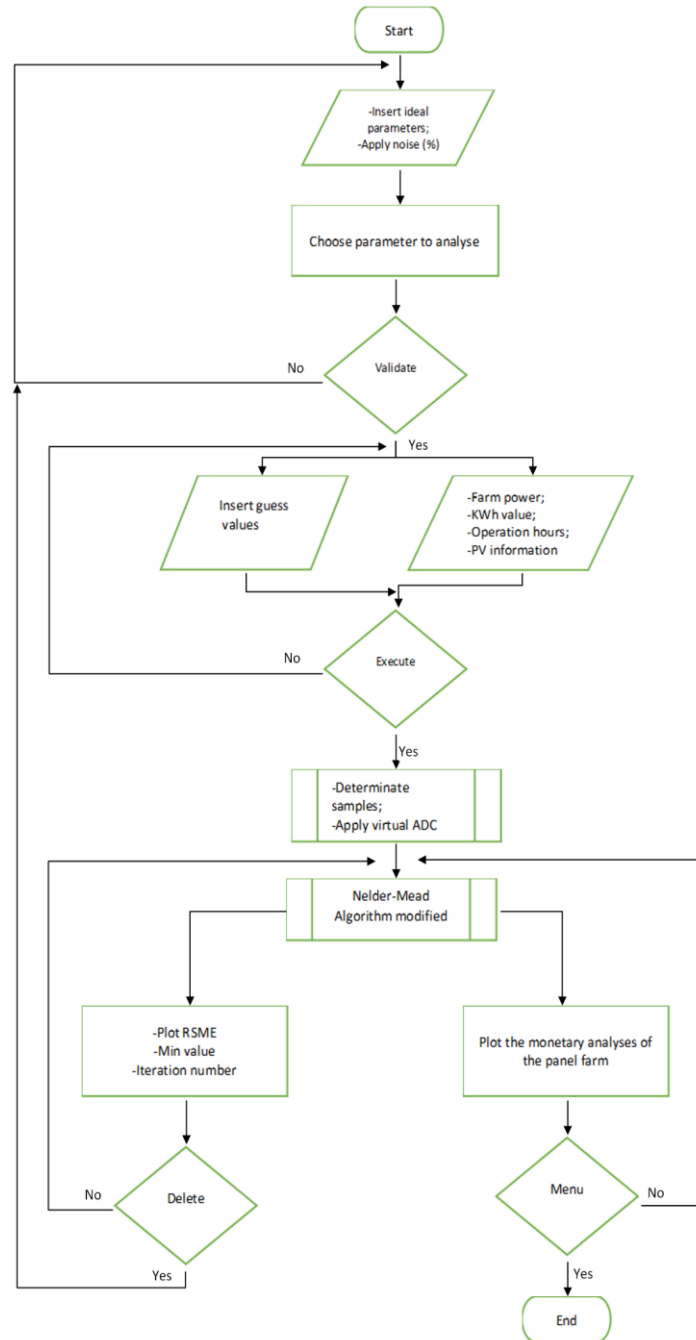
Figure 2.12.12: Flowchart of the "Parameter Analyses" screen.

Screen 3 – Cost Parameter Analyses

The third and last screen enables a direct cost analysis to be made for each parameter.

The screen consists of six tabs: one tab for the monetary study of each parameter of the single diode model and the last tab allows the desired real parameters to be entered. Figures 2.12.13 and 2.12.14 show examples of how this screen works.

(a) *(b)*
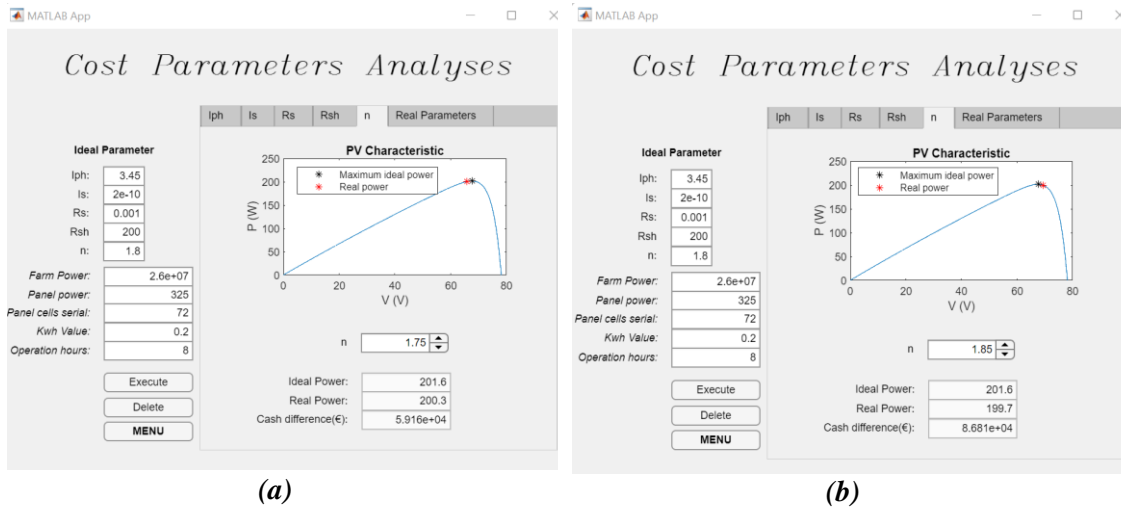
Figure 2.12.13: Cost analysis for diode ideal factor. (a) Default estimation. (b) Overestimation.

The Figure 2.12.13 (a) and (b) show a cost analysis carried out at the diode ideal factor parameter. The study of the parameter was performed by simulating a default estimate and an overestimation by selecting possible values present in the spinner. For this example, it was considered a farm with 26MW, which operates 8h per day and whose KWh value is 20 cents. It can be verified that this parameter, if wrongly estimated, has a high influence on the costs. Figure 2.12.14 shows the cost analysis for shunt resistance.

(a) *(b)*
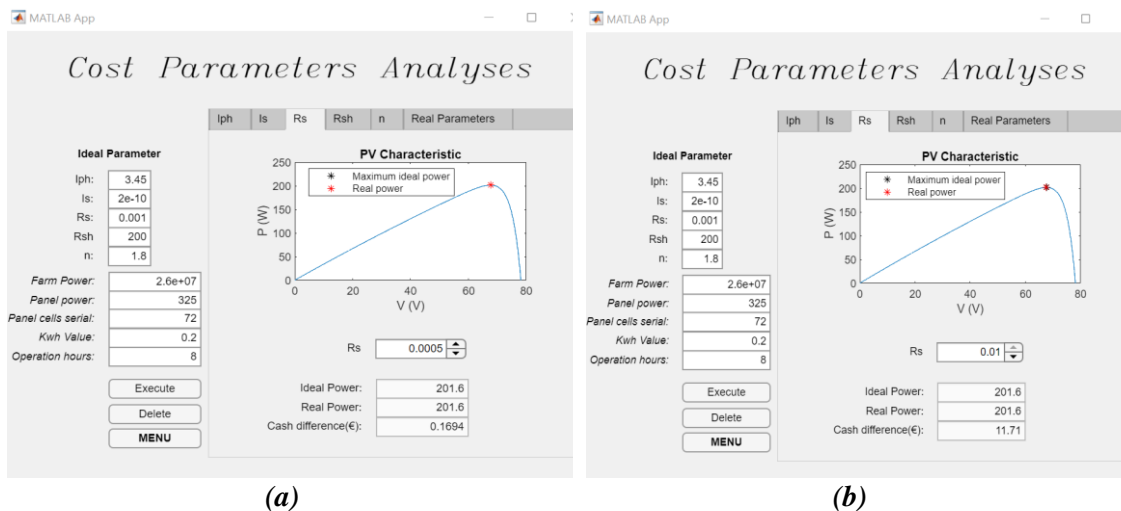
Figure 2.12.14: Cost analysis for serial resistance. (a) Default estimation. (b) Overestimation.

On the other hand, applying the same simulation conditions, it can be concluded from the Figure 2.12.14 (a) and (b) that the shunt resistance does not have a high influence in terms of costs, whether it is estimated by default or by excess.

At the base of this screen is a monetary analysis. The aim is to analyse, in euros (€), the amount of money lost in a year if one (or more) parameter is wrongly estimated.

In general, the PV curve is drawn considering the ideal parameters, thus saving the maximum power point (M_{PP}) which is represented in black on the graph (Figures 2.12.13 and 2.12.14). The real M_{PP} value resulting from the variation in the parameter under study is shown in red.

For this it is necessary to enter data such as: total farm power, the panel power, the number of cells, KWh value and number of hours of operation. At the end, the application shows the ideal and the real power value as well as the cash difference. In this way it is possible to conclude about the influence that each parameter has for the costs. The Table 2.12.2 shows the algorithm applied.

Step	Description	
	Ideal Values	**Real Values**
1	Insert the ideal parameter(s)	Insert the real parameter(s)
2	Drawing the characteristic curve IV	Drawing the characteristic curve IV
3	Drawing the characteristic curve PV	Drawing the characteristic curve PV
4	Calculate M_{pp} and V_{MPP}	Calculate V_{MPP}
5	Project the real V_{MPP} value onto ideal PV curve. Find the corresponding power value.	
7	$KWh\_value = Power \times Operation\_hours$ $day\_price = KWh\_value \times KWh\_price$ $year\_price\_ideal = day\_price \times 365$	$KWh\_value = Power \times Operation\_hours$ $day\_price = KWh\_value \times KWh\_price$ $year\_price\_real = day\_price \times 365$
8	$cash\_difference\_anual\_panel = year\_price\_ideal - year\_price\_real$ $cash\_difference\_anual\_farm = cash\_difference\_anual\_panel \times num\_panel$	

Table 2.12.2: Logic present in the "Cost Parameter Analyses" screen.

As shown in the logic in Table 2.12.2, initially the ideal parameter values as well as the real value(s) are entered into the platform.

Subsequently, the I-V and also the P-V characteristic curve will be drawn by applying the real and ideal parameters, thus making it possible to obtain the voltage value corresponding to the maximum power point. The voltage value corresponding to the real V_{MMP} will be projected onto the ideal curve, thus making it possible to know the real maximum power value.

As seen in step 7 and 8 of Table 2.12.2, knowing the number of hours of operation and the value of kWh, it is possible to calculate the real and ideal price value. This calculation allows to know the monetary value lost (cash difference) in a year if there is a bad parameter estimation. In order to make the calculation as real as possible, knowing the power of each panel as well as the power of the photovoltaic farm, the cost estimate is performed at the photovoltaic farm level.

For a better understanding of the algorithm, Figure 2.12.15 shows the flow chart of the "Cost Parameter Analyses" screen.
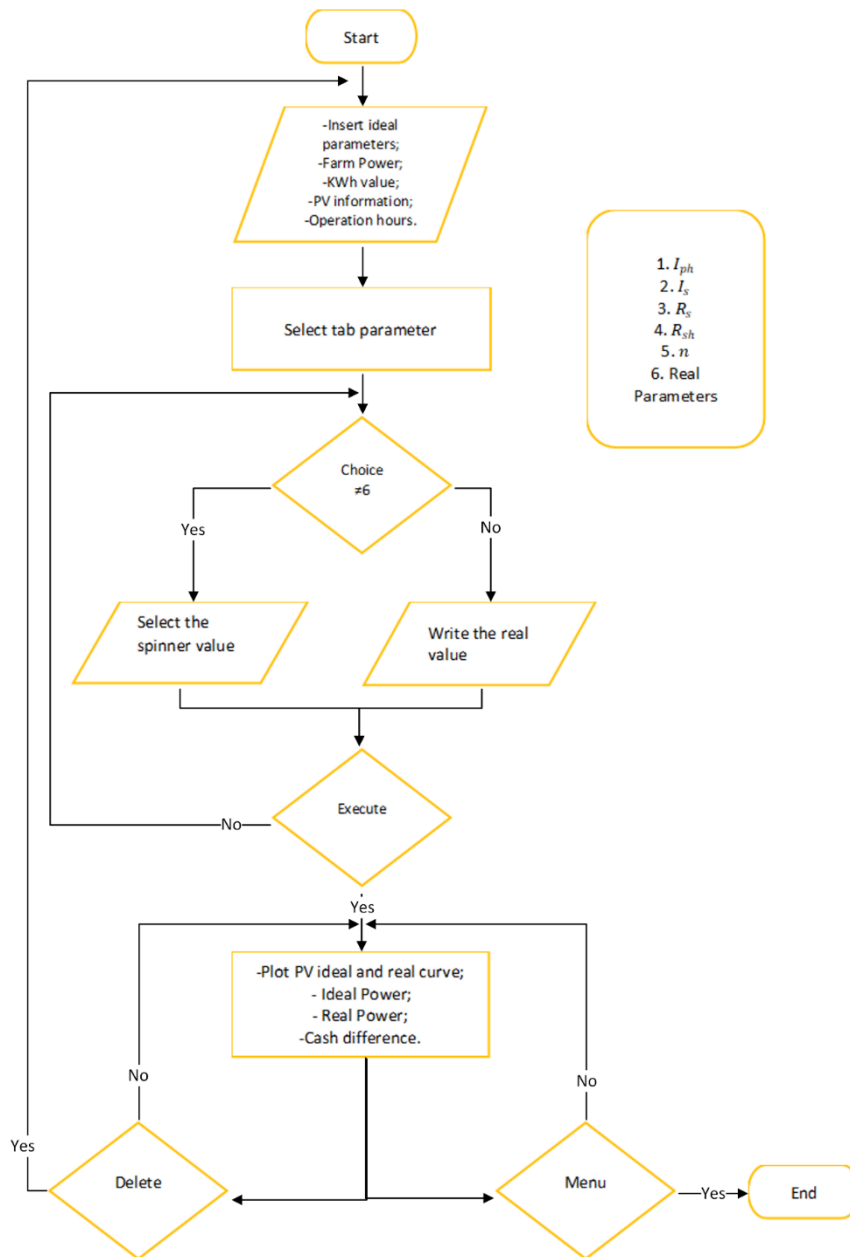
Figure 2.12.15: Flowchart of the "Cost Parameter Analyses" screen.

CHAPTER

3

Modified Nelder-Mead algorithm experimental validation

The present chapter is divided into four stages where all of them aim at validating the modified Nelder-Mead algorithm. In the first phase, it is used the RTC France cell, whose measurements are available in the laboratory, where it is intended to apply the performance indicators RMSE and R-squared as terms of comparison between the classical and modified Nelder-Mead algorithms. Subsequently, two different experimental methods are applied. Both have the purpose of measuring current and voltage values at the output of a PV applying different methods: an INA219 sensor coupled to an ESP32 board and a measurement acquisition system (DAQ). With this it is intended to obtain the I-V characteristic curves and calculate the maximum power point (M_{PP}). Both methods are described throughout the chapter. The experimental part ends with the implementation of the modified Nelder-Mead algorithm and the calculation of the M_{PP} in a low-cost embedded system that are of relevant importance.

3.1. Modified N&M algorithm validation

In the present section the experimental validation of the modified Nelder-Mead algorithm is performed. This algorithm will be applied to determine the five parameters by fitting the IV characteristic curve to the measured data.

Before carrying out the experimental part, the developed algorithm was validated on an R.T.C. France cell. This is a Silicon (Si) cell whose current and voltage measurements were already available in the laboratory. These experimental values were acquired at a temperature of 33ºC and 1000W/m^2.

It is very important to determine the first set of vertices of the simplex, because the convergence of the algorithm will depend on this choice. Initially, an approximation is sought for the first vertex and the others are created according to the criteria defined in *"2.8.1 Start and Stop Criterion"* in *Chapter 2*. The algorithm will stop when it finds a local minimum, but it may fail due to stagnation at a non-stationary point. [62]

In order to minimise the chances of the above problem occurring, an initial estimation of some parameters was made. For this purpose, the measured current and voltage samples are analysed (Figure 3.1.1) and, in this case, only the values referring to the "flat area" will be considered to perform the simple linear regression and this zone is approached as a straight line.

Linear regression analysis is used to predict the value of one variable based on the value of another. The variable that is desired to be predicted is called the dependent variable. The variable that is used to predict the value of another variable is called the independent variable.

This analysis estimates the coefficients of the linear equation, involving one or more independent variables that best predict the value of the dependent variable. The linear regression fits a straight or shallow line that minimises the discrepancies between predicted and actual output values. Then, the value of X (dependent variable) from Y (independent variable) is estimated. [64]

A simple linear regression is an equation, typically of the form shown in (3.1).

$$y = a + bx \qquad (3.1)$$

As indicated above, we intend to estimate the values (x, y) only by knowing some specific values $(x_1, y_1), (x_2, y_2), ..., (x_k, y_k)$. Where the values of a and b can be calculated by the following equations (3.2) and (3.3).

$$a = \frac{n \sum x_i y_i - \sum x_i \sum y_i}{n \sum x_i^2 - (\sum x_i)^2} \qquad (3.2)$$

$$b = \bar{y} - a\bar{x} \qquad (3.3)$$

Where n corresponds to the number of samples, $\bar{y}$ and $\bar{x}$ are the means of y and x respectively.
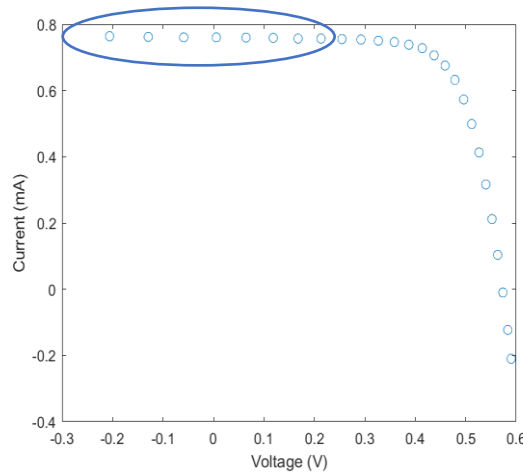
Figure 3.1.1: Measured current and voltage values of the RTC France cell.

To the current and voltage values present in Figure 3.1.1 were applied to equations (3.2) and (3.3). The first 8 points (n=8) were considered for the calculations and the straight line in equation (3.4) was obtained.

$$y = -1.5750 \times 10^{-2} x + 0.76035 \qquad (3.4)$$
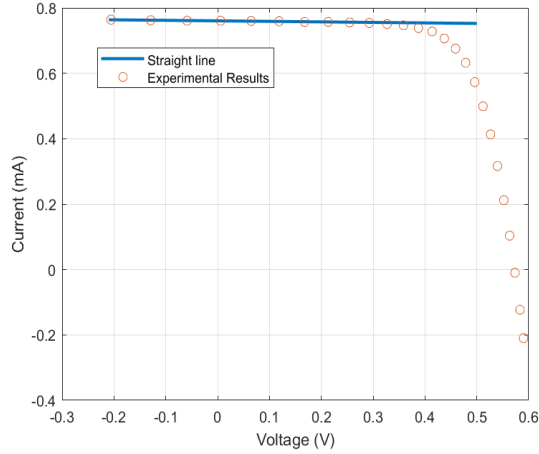
Figure 3.1.2: Straight line obtained considering the experimental results of the RTC France cell.

With the values calculated for the straight line equation and based on the experiment, it is concluded that the value intersecting the ordinate axis is relatively close to the value of the parameter I_{ph}. On the other hand, the value corresponding to the slope of the straight line is in the same magnitude order of the R_s parameter value. Therefore, these will be the initial values of the simplex for the parameters I_{ph} (0.76035 $[A]$) and R_s ($1.5750 \times 10^{-2}[\Omega]$) to be considered, thus being possible to reduce the chance of the algorithm stagnating at a local minimum or even to avoid the probability of non-convergence of the algorithm.

Finally, in order to analyse the performance of the algorithm three different experimental tests were carried out. The goal is to verify the convergence and performance of the *modified N-M algorithm* and the *classical N-M algorithm* when applied different initial guesses keeping the values of I_{ph} and R_s parameters estimated by linear regression. The algorithm applied, is described in the flowchart in Figure 3.1.4.

The following performance indicators were used as comparison object: Root means square error (RMSE) and R-squared (R^2).

The RMSE is a frequently used measure of the differences between the values (sample or population values) predicted by a model or an estimator and the observed values. The RMSE represents the square root of the second sample moment of the differences between the predicted and observed values or the root mean square of these differences. These deviations are called residuals when the calculations are performed on the data sample that was used for the estimation and are called errors (or prediction errors) when calculated outside the sample. RMSE is used for aggregating the magnitudes of errors in predictions for multiple data points into a single measure of predictive power. RMSE is a measure of accuracy for comparing prediction errors of different models for a given data set, not across data sets, as it is scale dependent. [93]

The RMSE is always non-negative and a value of zero (almost never achieved in practice) would indicate a perfect fit to the data. In general, a lower RMSE is better than a higher one. [94]

The mathematical expression for calculating the root means square error is the same as that applied in expression (2.33), i.e.,

$$RMSE = \sqrt{\frac{1}{N_p}\left(\sum_{p=1}^{N_p}(I_p - \hat{I}_p)^2\right)} \tag{3.5}$$

The coefficient of determination is a statistical measure that considers the difference in one variable that can be explained by the difference in a second variable when predicting the result of a given event. In other words, this coefficient, which is more commonly known as R-squared (or R^2), evaluates how strong the linear relationship between two variables is and is widely used by researchers when conducting trend analyses and is calculated by the mathematical expression (3.6). [95]

$$R^2 = 1 - \frac{\sum_{i=1}^{m}(\hat{I}_i - I_i)^2}{\sum_{i=1}^{m}(\bar{I} - \hat{I}_i)^2} \tag{3.6}$$

The coefficient of determination is a measure used to explain how much variability in one factor can be caused by its relationship with another related factor. This correlation, known as "quality of fit", is represented as a value between 0.0 and 1.0. A value of 1.0 indicates a perfect fit and is therefore a highly reliable model for future predictions, while a value of 0.0 indicates that the calculation cannot accurately model the data.

In a graph, the quality of fit measures the distance between a fitted line and all the data points that are scattered throughout the graph. The narrow data set will have a regression line close to the points and will have a high level of fit, meaning that the distance between the line and the data is small.

Considering the flow chart present in Figure 3.1.4 different test cases were performed for R.T.C. France cell as shown in the graphs of Figure 3.1.3.

Through the analysis of the results obtained, it is possible to verify the importance that the initial simplex has for the search of minimum values. In the different experimental test cases it is verified that the *classical Nelder-Mead algorithm*, represented in red on the graphs and Tables 1.3.1-1.3.3, presents some difficulty in reaching the ideal values, and may even move away from them when the initial guesses are not close to them, such effect being visible in Figure 3.1.4 (c) and respective Table 3.1.3.
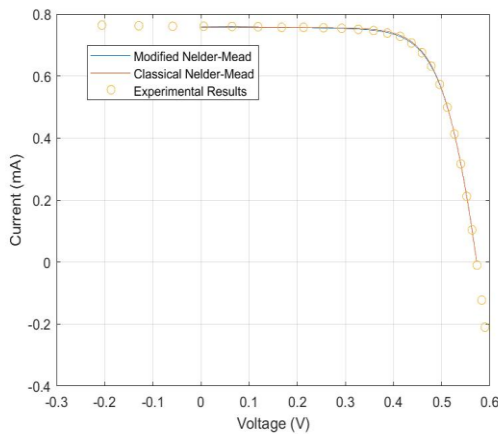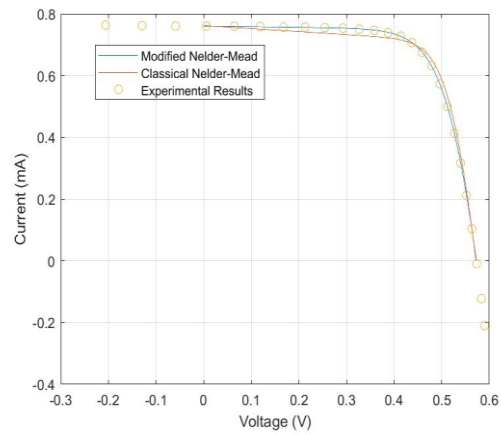
(a)   *(b)*
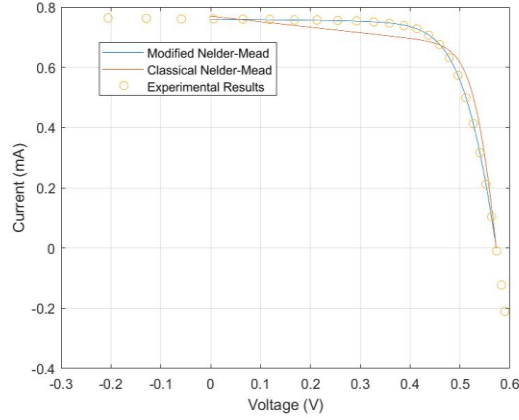
(c)

Figure 3.1.3: Experimental tests. (a) Test case 1 - best fit of the straight line to the measured values. (b) Test case 2 - second best fit of the straight line to the measured values. (c) Test case 3 - worst fit of the straight line to the measured values.

Designation	Parameter symbol	N&M classical algorithm	N&M modified algorithm
Five parameters	$I_{ph}[A]$	0.753	0.761
	$I_s[A]$	2.315×10^{-7}	3.107×10^{-7}
	$R_s[\Omega]$	3.879×10^{-2}	3.655×10^{-2}
	$R_{sh}[\Omega]$	2.962×10^2	52.89
	n	1.486	1.516
Short circuit current	$I_{sc}[A]$	0.757	0.760
Open circuit voltage	$V_{oc}[V]$	0.573	0.573
Voltage at P_{max}	$V_{mp}[V]$	0.4507	0.4507
Maximum power	$P_{mp}[W]$	0.3124	0.3107
Root Mean Squared error	RMSE	2.8312×10^{-3}	7.7301×10^{-4}
Coefficient of determination	R^2	0.9991	0.9999

Table 3.1.1: Results of the experimental test case 1.

Designation	Parameter symbol	N&M classical algorithm	N&M modified algorithm
Five parameters	$I_{ph}[A]$	0.753	0.761
	$I_s[A]$	2.315×10^{-7}	3.107×10^{-7}
	$R_s[\Omega]$	3.879×10^{-2}	3.655×10^{-2}
	$R_{sh}[\Omega]$	2.962×10^2	52.89
	n	1.486	1.516
Short circuit current	$I_{sc}[A]$	0.762	0.760
Open circuit voltage	$V_{oc}[V]$	0.572	0.573
Voltage at P_{max}	$V_{mp}[V]$	0.4507	0.4507
Maximum power	$P_{mp}[W]$	0.3124	0.3107
Root Mean Squared error	RMSE	2.8485×10^{-2}	7.7301×10^{-4}
Coefficient of determination	R^2	0.99624	0.99999

Table 3.1.2: Results of the experimental test case 2.

Designation	Parameter symbol	N&M classical algorithm	N&M modified algorithm
Five parameters	$I_{ph}[A]$	0.737	0.758
	$I_s[A]$	1.213×10^{-11}	7.217×10^{-7}
	$R_s[\Omega]$	2.917×10^{-2}	3.347×10^{-2}
	$R_{sh}[\Omega]$	5.447	2.1560×10^4
	n	0.901	1.607
Short circuit current	$I_{sc}[A]$	0.769	0.758
Open circuit voltage	$V_{oc}[V]$	0.573	0.573
Voltage at P_{max}	$V_{mp}[V]$	0.4805	0.4496
Maximum power	$P_{mp}[W]$	0.3139	0.3165
Root Mean Squared error	RMSE	3.1065×10^{-1}	2.3548×10^{-3}
Coefficient of determination	R^2	0.9764	0.9994

Table 3.1.3: Results of the experimental test case 3.

On the other hand, it can be seen that the *modified Nelder-Mead algorithm* (blue curve in the graphs) maintains, in general, a good fit to the points. It is also possible to compare, in each test case table, the RMSE and R^2 results as well. In these parameters it is noticeable that the value of the residuals is smaller for the developed algorithm as well as the coefficient of determination is closer to the value 1. In this way it may be concluded that the modified algorithm, for the conditions tested, has a better performance than the classical algorithm.
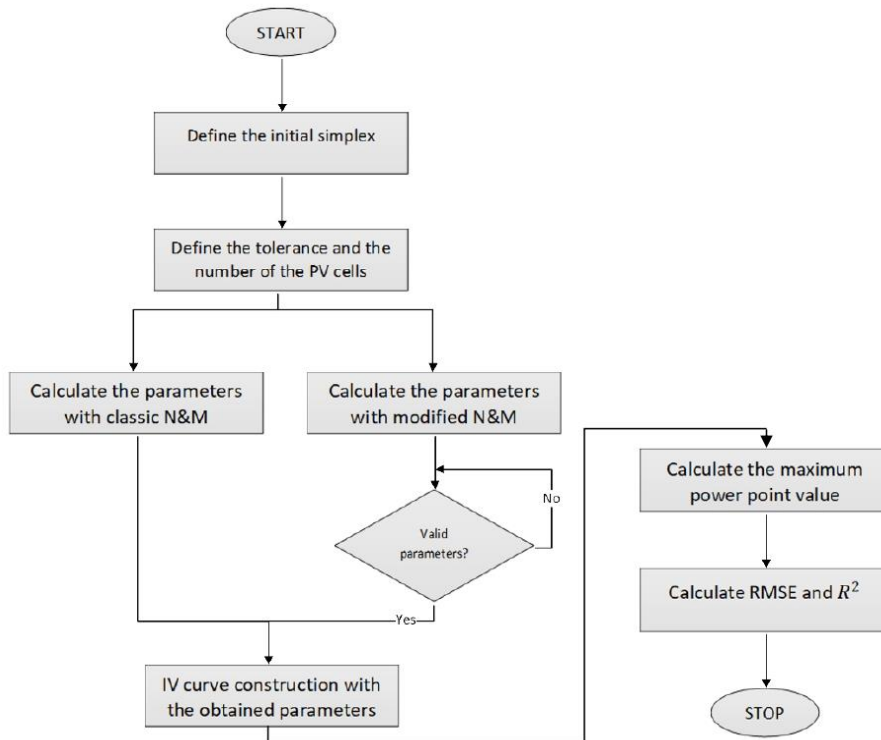
Figure 3.1.4: Program that estimates the parameters, calculates the value of the maximum power point, and compares the classical and modified N&M algorithms.

3.2. Method 1 – Sensor to read data

The first experimental work aims to integrate an embedded system with a sensor, which allows making measurements of current and voltage values of a photovoltaic panel. The instrumentation required to carry out the experiment comprises a photovoltaic module, a variable resistor, an INA219 sensor and one microcontroller ESP32. The configuration schematic of the experimental setup is shown in Figure 3.2.1.
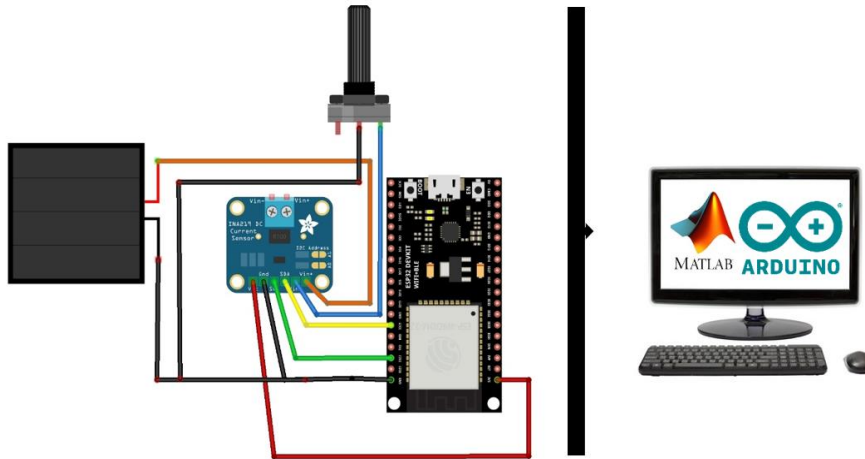
Figure 3.2.1: Schematic of the experimental method implemented.

With this assembly and exposing the panel to solar radiation, it is intended to trace the I-V characteristic curve of the photovoltaic module used, subsequently applying the *Nelder-Mead algorithm* in order to identify the value of the five PV parameters and finally calculate the maximum power point value (P_{max}).

The INA219 sensor, whose description is given in the subtopic "INA219 sensor", will detect the current and voltage at the output of the photovoltaic panel. The readings are then transmitted to the ESP32 microcontroller. The board was programmed using the Arduino IDE where an available library called "Adafruit INA219" was used to program the INA219 module. At the same time, the ESP32 device performs a serial communication with the computer that, through a programmed protocol, the readings (current and voltage) will be received in the MATLAB software.

To perform the experimental activity, it is used a photovoltaic module of the Figure 3.2.2 available in the laboratory composed of 14 solar cells in series and with an area of 3.68×10^{-2} m^2.
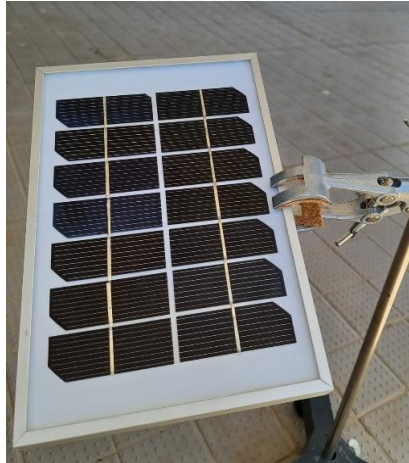
Figure 3.2.2: Photovoltaic module for experimental work.

INA219 Sensor

The INA219 module (Figure 3.2.3) is a current and voltage sensor developed for monitoring, using a shunt resistor to make the necessary measurements. Its interface has compatibility for I2C or SMBUS, being responsible for monitoring the voltage drop in the shunt resistor and the bus supply voltage. The module performs measurements in the range of 0 to 26 VDC, with maximum current limit according to the shunt resistance, the board features a 100mΩ shunt resistor, and the maximum tolerated current is 3.2 A. To power the module, it is necessary to use a 3 or 5V source. [96]
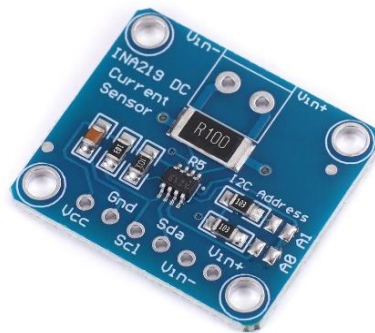
Figure 3.2.3: Sensor INA219. [97]

Due to the impossibility of measuring the current directly in the component, the INA sensor uses a shunt resistor. The shunt resistor is a resistor connected in series with the load, and through the voltage drop over this component it is possible to determine the current in the circuit, usually a low resistance component is used, so that it does not interfere with the total resistance, usually between 1mΩ and 1Ω, and of high power to withstand the current without suffering damage. The current calculation is made following the principle of Ohm's Law, knowing the resistance (R) and the voltage (V), it is possible to determine the current, according to equation (3.7).

$$I = \frac{V}{R} \tag{3.7}$$

The Figure 3.2.4 shows the simplified schematic of the module available in the datasheet. The INA219 sensor has 16 programmable addresses, jumpers for I2C addressing and an internal 12 bit ADC converter. [96]
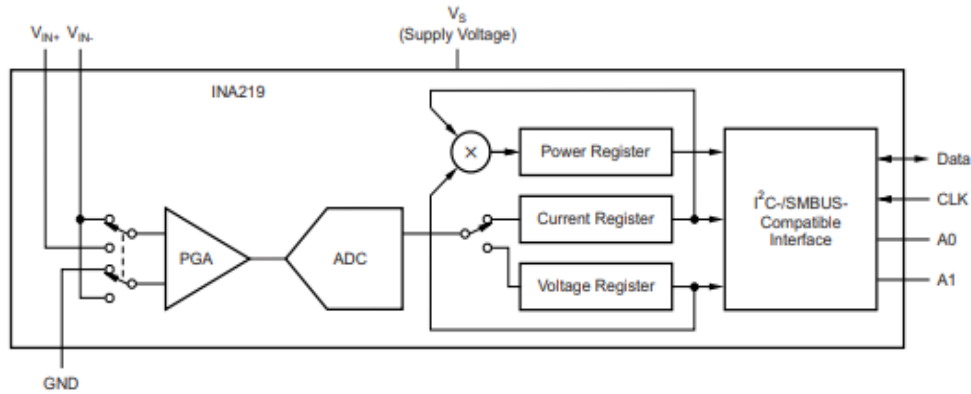
Figure 3.2.4: Simplified schematic diagram of an INA219 module. [96]

ESP microcontroller

The ESP family was created and is produced by the Chinese company Espressif Systems which aimed to facilitate access to the world of prototyping by integrating several components, previously sold separately, on a single board**.** [98]

ESPs are structured in a similar way to an Arduino: they have a memory module, one for Wi-Fi connection, another for Bluetooth, GPIO pins (General Purpose Input/Output, used for digital signals) and ADC channels (Analogic-Digital Converter, for analog signals), all controlled by a microprocessor. These microcontrollers are able to interpret programming languages other than C++, such as JavaScript, Python and C.

The ESP family is extremely versatile and has applications in any prototyping, automation and especially IoT (Internet of Things) projects. All these boards can communicate with other devices through the Internet or Bluetooth. In addition, its board occupies a small area, and supports temperatures from - 40 to 125 ºC, which allows its use in various environments.

ESPs are microcontrollers suitable for projects that need access to the Internet or are in unfavourable environments for technology, which are the reasons why it was thought to apply these panels in the present experimental work. In this regard was used the ESP32 (Figure 3.2.5) microcontroller, placed on the market in 2016 by the company Espressif Systems.
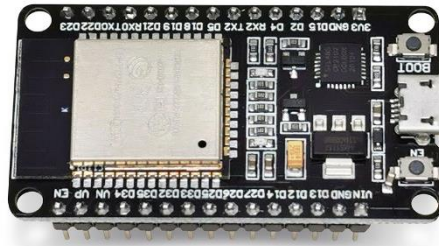
Figure 3.2.5: ESP32 microcontroller. [99]

On the pins of an ESP32, there are 34 GPIO ports, 3 SPI, 2 I2S, 2 ADC converters (12 bits) of up to 18 channels, 2 DAC converters (8 bits), 3 UART, 10 touch sensor pins, PWM, among others. The diagram in the Figure 3.2.6 shows the distribution of the existing components on the board. [100]
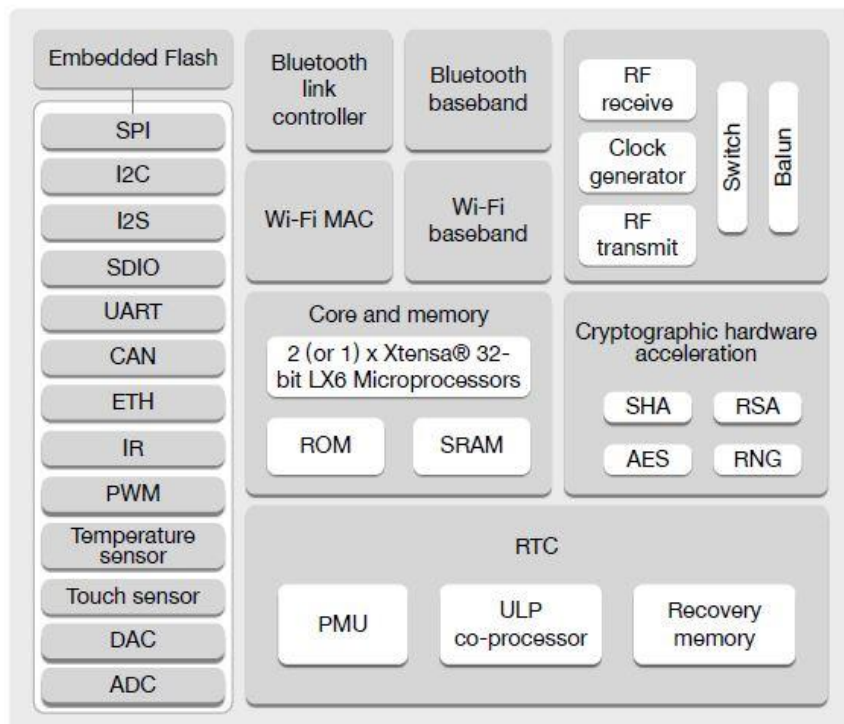
Figure 3.2.6: Distribution of components in an ESP32 microcontroller. [100]

Results of experimental Nelder-Mead algorithm

This section is devoted to the validation of the *modified Nelder-Mead algorithm* based on the experimental measurements obtained by applying the experimental method 1. The analysis is performed through the dependence that the algorithm presents by applying different values for the initial simplex and the effect that the tolerance imposed as a stopping criterion has.

Similarly to the RTC France cell, the results obtained using the classical and modified *Nelder-Mead algorithm* are compared.

Note that the value of the cell temperature was not measured, so for the purposes of applying the algorithm the temperature of 25ºC was considered. The Table 3.2.1 shows the initial conditions to start the iterative process of the algorithm.

		Case 1	Case 2
Number of cells		14	
Straight line equation		$y = -3.3852 \times 10^{-3}x + 0.55633$	
Initial guesses	$I_{ph}[A]$	0.55633	0.55633
	$I_s[A]$	1×10^{-9}	1×10^{-8}
	$R_s[\Omega]$	3.3852×10^{-3}	3.3852×10^{-3}
	$R_{sh}[\Omega]$	200	200
	n	1.2	1.7

Table 3.2.1: Initial conditions to start the algorithm.

As shown in Table 3.2.1. two different test cases were performed for the same measurements taken through the experimental process of Figure 3.2.1. Figure 3.2.7 shows the graphs obtained for both cases.
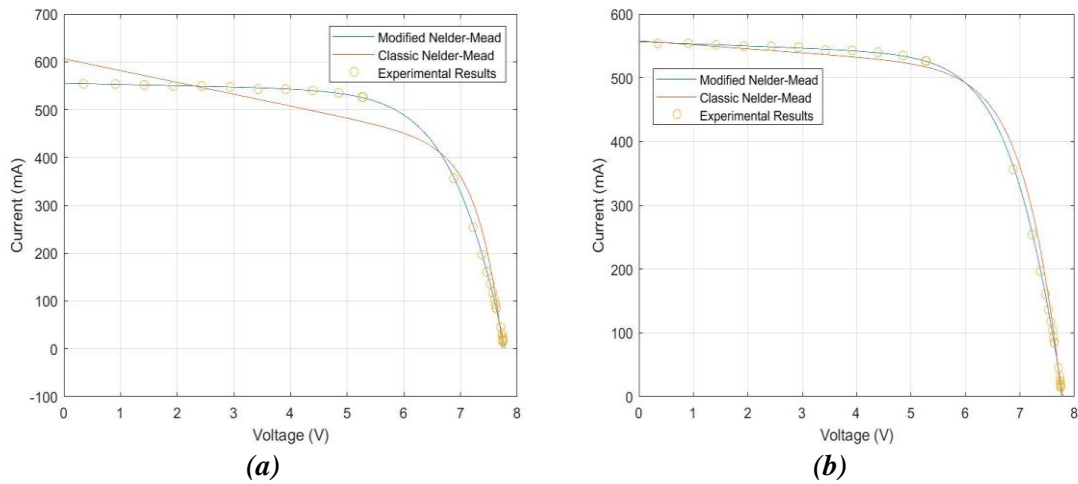
Figure 3.2.7: IV characteristic curve and measured values. (a) Case 1. (b) Case 2.

Figures 3.2.7 (a) and (b) show the curve fitting to the measured values. In order to estimate the parameters, the *classical Nelder-Mead algorithm* (curve in red) and the *modified Nelder-Mead algorithm* (curve in blue) were applied.

To display the results, two different cases were studied where for some of the parameters a different initial guess was applied. To the *modified Nelder-Mead algorithm*, it was checked that the values achieved in both cases are very close and in general, within the same order of

magnitude. On the other hand, the results achieved by the classical algorithm are very distinct and the same can be seen in the graphs, where in case 1 (Figure 3.2.7 (a)) the curve obtained does not fit the experimental values.

In order to complement the graphs in Figure 3.2.7, two Tables (3.2.2 and 3.2.3) were prepared with the results obtained for both case studies.

Designation	Parameter symbol	N&M classical algorithm	N&M modified algorithm
Five parameters	$I_{ph}[A]$	0.606	0.556
	$I_s[A]$	9.542×10^{-9}	3.1211×10^{-6}
	$R_s[\Omega]$	-4.505×10^{-2}	0.5578
	$R_{sh}[\Omega]$	40.541	4.045×10^2
	n	1.223	1.794
Short circuit current	$I_{sc}[A]$	0.606	0.556
Open circuit voltage	$V_{oc}[V]$	7.7419	7.7824
Voltage at P_{max}	$V_{mp}[V]$	6.4283	6.0154
Maximum power	$P_{mp}[W]$	2.7483	2.9326
Root Mean Squared error	RMSE	3.1097×10^{-2}	2.4599×10^{-3}
Coefficient of determination	R^2	0.98123	0.99988

Table 3.2.2: Results of Case 1.

Designation	Parameter symbol	N&M classical algorithm	N&M modified algorithm
Five parameters	$I_{ph}[A]$	0.559	0.558
	$I_s[A]$	7.9571×10^{-7}	8.1838×10^{-7}
	$R_s[\Omega]$	0.1919	0.7108
	$R_{sh}[\Omega]$	1.6086×10^2	3.036×10^2
	n	1.613	1.6165
Short circuit current	$I_{sc}[A]$	0.557	0.557
Open circuit voltage	$V_{oc}[V]$	7.7631	7.7861
Voltage at P_{max}	$V_{mp}[V]$	6.2351	6.0403
Maximum power	$P_{mp}[W]$	2.9697	2.9518
Root Mean Squared error	RMSE	1.4572×10^{-2}	2.7646×10^{-3}
Coefficient of determination	R^2	0.99518	0.99985

Table 3.2.3: Results of Case 2.

Finally, analysing the values of the Tables 3.2.2 and 3.2.3 for the Root Mean Squared Error (RMSE) and the coefficient of determination (R^2), it can be concluded that the residual value

obtained in both cases is lower for the developed algorithm and there is also a better adjustment of the curve to the points by this one (value closer to 1).

3.3. Method 2 – Data acquisition system

There are different processes for carrying out experimental work. In this second method, a data acquisition board (DAQ), a function generator and a photovoltaic module (Figure 3.2.2) were used to obtain valid readings in real time. The experiments were made with the photovoltaic panel under solar radiation, thus it is possible to obtain more accurate results to identify the panel behaviour.

__Data acquisition (DAQ) board__

Acquiring data can simplistically be defined as measuring real world information. Most real-world occurrences and their measurement have an analogue character. So the aim is to collect the information about the physical and electrical phenomenon happening in the project. This collection helps to understand the behaviour of the system. To perform data acquisition (DAQ) four distinct phases are required: sensors, measuring devices, instruments and computer. This set is called a DAQ system and is represented schematically in Figure 3.3.1. [101] [102]
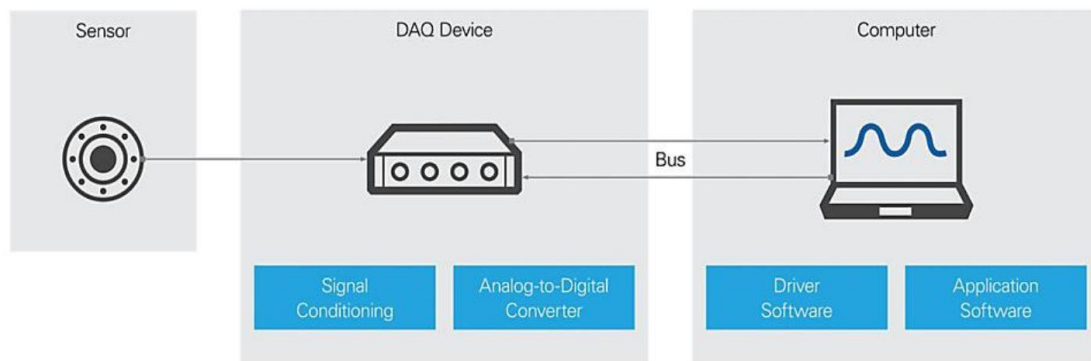
Figure 3.3.1: DAQ Data Acquisition system block diagram. [101]

As shown in diagram 3.3.1, a DAQ system consists of sensors, DAQ device and the computer. The sensors (or transducers) convert are devices that transform a physical magnitude, such as temperature, pressure, position (among others), into an electrical signal (voltage or current). Since the electrical signals generated by the sensors must be optimized for the ADC (Analog-to-Digital) converter input scale, signal conditioning must be performed. Signal conditioning consists in amplifying low intensity signals, isolating and filtering them for more precise measurement. These are the functions of the DAQ board: signal conditioning and ADC converter. Finally, the computer has the platform to run the DAQ system application, which requires the special driver software to be installed on the computer. In order to transmit signals, the blocks are interconnected with each other. This function is performed by the data bus based on a protocol such as: RS232, RS485, Ethernet, USB, or other field buses. [101]

In the present work, MATLAB R2021a is used as the software that makes the connection with the board. As mentioned, it could use different types of communication, however the GPIB port to USB will be used as a means of connection. Additionally, the NI-DAQmx driver software is installed in order to read the data through the MATLAB tool.

The data acquisition board plays an important role as a means of communication between sensors and the computer. Through software installed on the computer, it can decode the signal from the DAQ and communicate with it. The data acquisition board used in this work is the NI USB-6009 shown in the Figure 3.3.2.

Figure 3.3.2: NI USB-6009 DAQ board. [103]

The NI USB-6009 board is a low-cost multifunction DAQ device. As shown in the Figure 3.3.3, it has 8 analogue inputs of 13 and 14 bits with a maximum sampling rate of 48 kS/s, 2 analogue output 12 bits, 12 digital I/O and a 32 bits counter. The USB-6009 provides basic functionality for projects and laboratory experience. The device has a lightweight mechanical box and is bus-powered for easy portability. It can easily connect sensors and signals to the USB-6009 with screw terminal connectivity. [104] [105]

Figure 3.3.3: NI USB-6009 port description. [104]

Function generator and GPIB devices

A Function Generator is an instrument used to generate electrical waveform signals. The frequency is variable (from a few Hz to hundreds of MHz) as well as the signal amplitude (voltage). These devices are widely used in laboratories as signal sources for testing various types of electronic equipment. A function generator is normally capable of generating sine, triangular, square and sawtooth waves, all with various frequencies and amplitudes. It usually has a frequency meter attached and several adjustment and selection buttons, as well as signal outputs. Its operation is based on electronic circuits, oscillators, filters and amplifiers. [106]

In the present work it was used the AFG 320 (Figure 3.3.4) function generator available in the laboratory. It is a function generator with two independent output channels and the instrument supports standard waveforms such as: sine, square, triangular, ramp, pulse, DC and noise.

Figure 3.3.4: AFG 320 function generator used in the experimental work.

The output characteristics are shown in Table 3.3.1. [107]

Characteristic	**Description**
Amplitude (into 50Ω)	$50mVp-p$ to $10mVp-p$. Accuracy: ±(1% of setting + 5mV) at 1kHz, no offset
Offset (into 50Ω)	505 $mVp-p$ to 10 $Vp-p$ amplitude: peak amplitude + offset is limited to +5V or –5 V. 50 $mVp-p$ to 500 $mVp-p$ amplitude: –0.75 V to +0.75 V. Accuracy: ± (1% of setting +5 mV)
Resolution	5mV
Impedance	50 Ω

Table 3.3.1: Output characteristics of the AFG 320 function generator. [107]

The AFG 320 function generator loads waveforms from using GPIB (General-Purpose Interface of Bus) interface. In this sense, a GPIB-USB-HS is used to provide the interface between MATLAB tool and the function generator allowing automatic control of the output waveforms, depending on the information received**.**

The GPIB-USB-HS (Figure 3.3.5) is a portable analyser device and IEEE 488 controller for computers with USB slots. It can be used to integrate an instrument into a system using GPIB. The GPIB-USB-HS can connect to a high-speed USB port and can control up to 14 programmable GPIB instruments. This device has a modern design, which provides physical compatibility with almost any instrument. [108]

Figure 3.3.5: GPIB-USB-HS interface. [108]

Application of the method and results

Finally, the experimental procedure is implemented where DAQ is applied. The Figure 3.3.6 shows the assembly carried out in a laboratory environment, where the photovoltaic panel, through a breadboard, is connected to a DAQ board and the function generator.
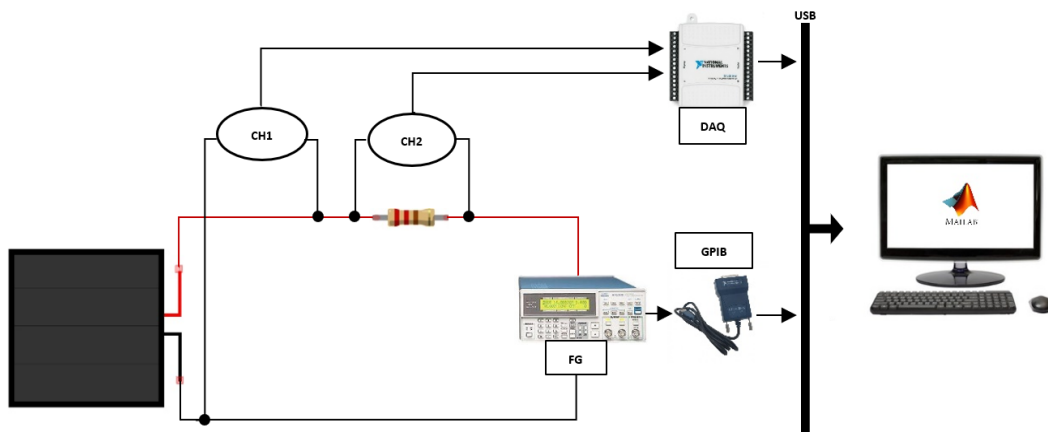
Figure 3.3.6: Schematic of the experimental method implemented.

The computer has the necessary drivers and programs installed to communicate with the function generator and DAQ board. In order to communicate successfully with the function generator and read information from the board, code was developed in MATLAB environment.

In this sense, the DAQ is connected to the computer which provides information on the voltage readings made on the PV module through functions for this purpose available in the MATLAB tool. A resistor with 1.2Ω is connected to the PV, where the voltage value is also read. Finally, the function generator is connected in parallel to the photovoltaic module. The aim is to generate a function so that the I-V characteristic curve of the panel can be plotted.

The inputs A0+/- and A1+/- of the DAQ are connected to the output of the photovoltaic module in order to measure the output voltage and also to the additional resistor to measure its voltage. The purpose of the resistance present in the circuit is to find out the value of the current in the circuit. Once the voltage value is known and also the resistance value is known, the current is calculated using Ohm's law. Through MATLAB, indication is given to the function generator to generate a RAMP type signal where the values regarding amplitude and frequency will be adjusted based on the experiment and results obtained. All the values read are stored in the workstation being used to subsequently plot the characteristic of the photovoltaic panel under study.

Due to the maximum amplitude limit of the function generator used (see Table 3.3.1) it was not possible to perform the experiment with the panel exposed directly to solar radiation, placing it in the shadow. Applying the present laboratory method, the current and voltage measurements were taken as shown in the Figure 3.3.7.
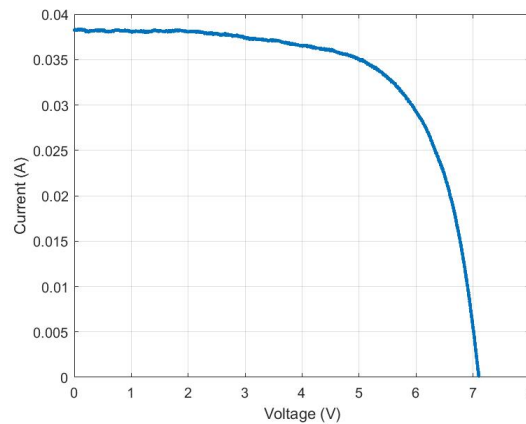
Figure 3.3.7: Output Figure I-V measurements from the data acquisition system.

The *modified Nelder-Mead algorithm* was used to estimate the parameters. However, for comparative study purposes, the *classic Nelder-Mead algorithm* is also applied. In this way, as in the other methods, the logic present in the flowchart of Figure 3.1.3 is followed. The graphics in the Figure 3.3.8 show the fit of the I-V curve obtained to the points measured with the DAQ as well as the respective P-V curve.

Note that the cell temperature was not measured in the experiment. For the estimation of the parameters a temperature of 25ºC was applied in the algorithm. Considering that in the previous experiments were discussed the importance that the initial guesses must initialise the *Nelder-Mead algorithm*, in the present method it was attempted to attribute to the initial simplex values close as possible to the minimum value in order to obtain better estimates.
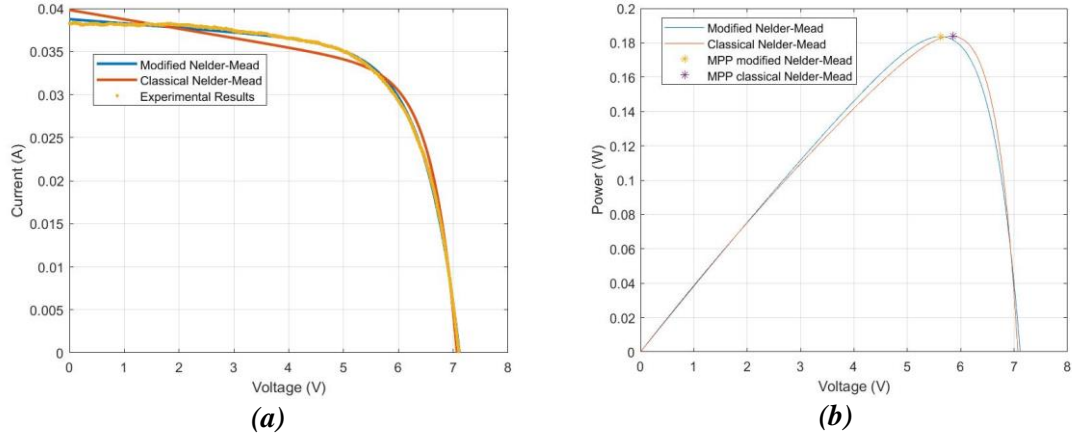
Figure 3.3.8: Characteristic curve using DAQ system. (a) I-V characteristic curve and measured values applying the modified and classical Nelder-Mead algorithms. (b) P-V curve applying the modified and classical Nelder-Mead algorithms.

The analysis of the graphs as well as the results achieved in the Table 3.3.2 shows the *modified Nelder-Mead algorithm* presents a better performance than the classical algorithm. It is notable that, for this case, the *classical Nelder-Mead algorithm* presents some difficulty in adjusting to the measured points. Relatively to the classical algorithm it can also be concluded that this shows a greater sensitivity to the initial guesses assigned to each parameter.

Designation	Parameter symbol	N&M classical algorithm	N&M modified algorithm
	$I_{ph}[A]$	3.9827×10^{-2}	3.8776×10^{-2}
	$I_s[A]$	3.6189×10^{-9}	3.5125×10^{-7}
Five parameters	$R_s[\Omega]$	-6.1863×10^{-4}	0.97772
	$R_{sh}[\Omega]$	9.1864×10^{2}	2.0190×10^{3}
	n	1.2278	1.7163
Short circuit current	$I_{sc}[A]$	3.9827×10^{-2}	3.8752×10^{-2}
Open circuit voltage	$V_{oc}[V]$	7.0687	7.1127
Voltage at P_{max}	$V_{mp}[V]$	5.8590	5.6176
Maximum power	$P_{mp}[W]$	0.18385	0.1836
Root Mean Squared error	RMSE	1.0376×10^{-3}	2.7529×10^{-4}
Coefficient of determination	R^2	0.98972	0.99928

Table 3.3.2: Results after applying the modified and classical Nelder-Mead algorithms.

Even considering this is a small and low power photovoltaic panel, a cost analysis can be carried out to verify the amount of money lost in a year if the *classic Nelder-Mead algorithm* was applied. To do this, it was started by projecting the V_{mp} value obtained through *the classic Nelder-Mead algorithm* on the P-V curve of the *modified Nelder-Mead algorithm*, thus knowing the maximum power point as shown in the Figure 3.3.9.
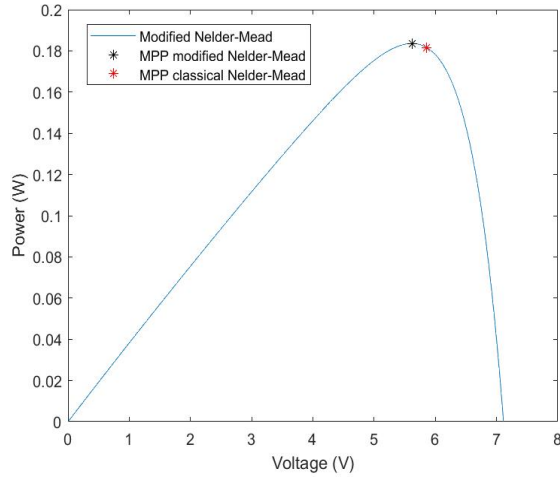
Figure 3.3.9: Projection of the Vmp value of the classical Nelder-Mead algorithm onto the PV curve of the modified Nelder-Mead algorithm.

This simulation, considering a 1MW farm, will have approximately 55 million photovoltaic panels with the defined characteristics, where these panels work 8h/day with the kWh value at 20 cents. Performing the calculations, there will be a monetary difference of 64 394€ in one year. In the Figure 3.3.10 is a graph with cost forecasts applying the same conditions until 20 years. Note that the present monetary study carried out corresponds to the photovoltaic panel used to perform the laboratory experiments.
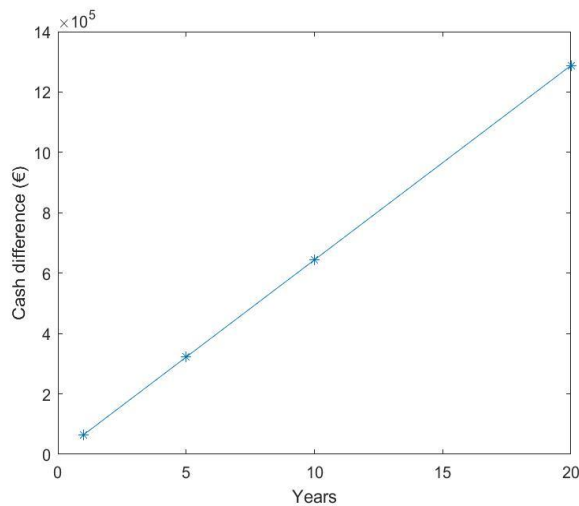
Figure 3.3.10: Cash difference lost if the parameters of the classical Nelder-Mead algorithm are applied.

3.4.   Method 3 – Using a microcontroller

Embedded systems are increasingly present in our daily life, the low-cost technology allowed the increase of the hardware capacity, enabling the implementation of more complex applications. The emergence of new applications is driven by market growth and a better

knowledge of human needs. However, the complexity of these new applications is reflected in the process of their development. The purpose of this method is to apply a low-cost embedded system to calculate the value of the maximum power point using a photovoltaic panel exposed solar radiation. The Figure 3.4.1 shows the laboratory assembly.
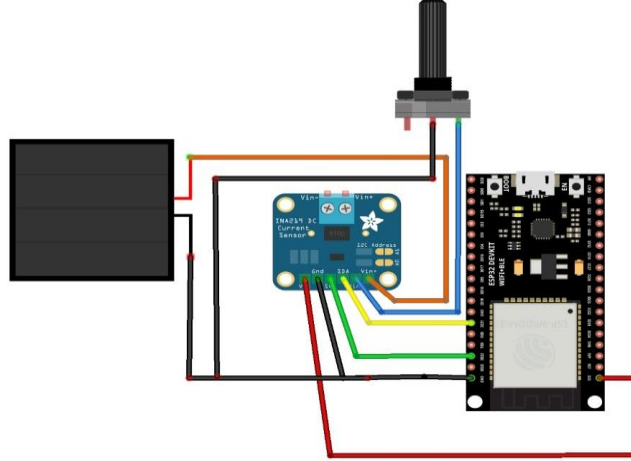
Figure 3.4.1: Schematic of the experimental method implemented.

Using an ESP32 microcontroller, it will acquire the values at the photovoltaic panel's output through an INA219. In order to vary the voltage values, similarly to the first laboratory work, a variable resistance available in the laboratory is used.

Arduino IDE was the software chosen to program the ESP32, the board was programmed with the *modified Nelder-Mead algorithm* whose logic is shown in the flowchart in the Figure 3.4.2.

Applying the assembly presented in Figure 3.4.1, the following characteristics of the photovoltaic module present in Table 3.4.1 are obtained.

Designation	**Parameter symbol**	**N&M modified algorithm**
	$I_{ph}[A]$	5.8530×10^{-1}
	$I_s[A]$	1.0015×10^{-6}
Five parameters	$R_s[\Omega]$	3.4696×10^{-3}
	$R_{sh}[\Omega]$	60.032
	n	1.6616
Short circuit current	$I_{sc}[A]$	5.8527×10^{-1}
Open circuit voltage	$V_{oc}[V]$	7.79024
Voltage at P_{max}	$V_{mp}[V]$	6.23218
Maximum power	$P_{mp}[W]$	2.79033

Table 3.4.1: Characteristics of the photovoltaic module with ESP32 microcontroller.
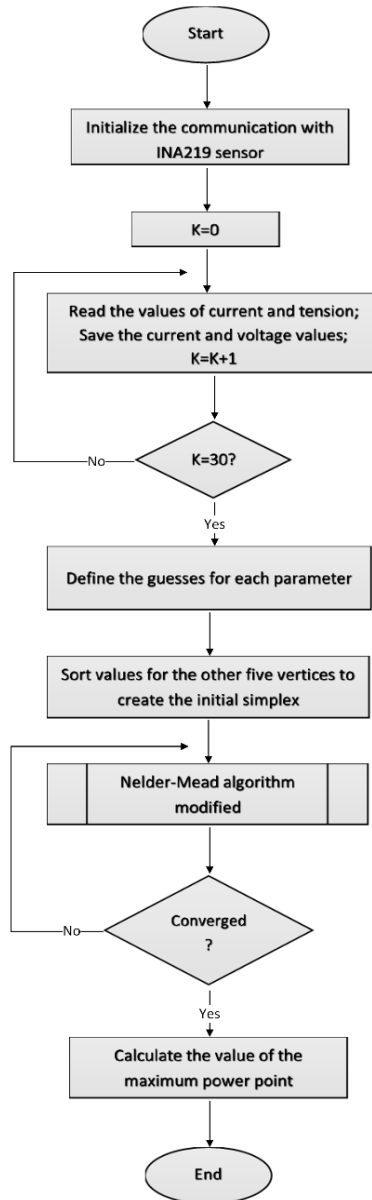
Figure 3.4.2: Flowchart with the logic implemented in the ESP32.

As shown in the flowchart in Figure 3.4.2, the ESP32 will instruct the INA 219 sensor to collect 30 points (voltage and current values) by varying a load and store them in the board memory. After indicating the guesses for building the initial simplex, the *modified Nelder-Mead algorithm* will be executed on the ESP32 board until the convergence criteria is satisfied. With the five parameters obtained, it will then be possible to know the P-V characteristic curve thus calculating the maximum power point value.

This validation method is under development in the NeuralSolar startup, where the aim is to extract the exact parameters by applying low tolerances. However, this work was an important step in the characterisation of photovoltaic panels, where the development of the *modified Nelder-Mead algorithm* was started and advantageous alterations were applied to the method in favour of the photovoltaic panel functions.

CHAPTER

4

Conclusion and future work

The present research work addressed several topics in the area of photovoltaic panels parameters estimation. Due to the non-linear nature of the equation resulting from the model describing the behaviour of a photovoltaic cell, it was chosen to apply the *Newton-Raphson* numerical method in order to plot the characteristic I-V curve.

The main aim of the dissertation work was to develop an algorithm to calculate the maximum power point of a photovoltaic panel. In this sense, the *modified Nelder-Mead* algorithm, which allows the estimation of the five parameters of a solar cell in real time, was developed and validated. Based on the classical algorithm, a way to improve it was sought. Modifications were made in the stopping criterion and also in the initialization criterion. The initialization points of the algorithm are the fundamental key for the convergence of the algorithm without getting stuck on a wrong value or a local minimum value. In this sense, given the importance of the initial simplex for the convergence of the algorithm it was thought strategies to apply and were suggested the following two: estimate the initial guesses through the analysis of the trend of the I-V characteristic curve, which was only applied to two of the parameters and on the other hand a versatile interface was developed. This application allows studying the algorithm behaviour during the cost function minimisation, analysing the level lines, the error function and also allows analysing the problem from a financial perspective in case there is a bad estimate of a parameter. In order to analyse the performance of the developed algorithm in the adjustment of the curve to the measured values, two different indicators were used: RMSE and R-squared. These indicators allow to conclude, for the studies carried out, that the *modified Nelder-Mead Algorithm* presented a better fit between curve-measured values than the classic algorithm.

Another goal of this work was to program a low-cost embedded system (ESP32) that allows the measurement of current and voltage in a photovoltaic panel and apply the developed algorithm to calculate the M_{PP} value without using MATLAB software (which did not happen with the other experimental methods performed), only using the Arduino IDE to display the readings and the USB port to power the board. Given the impossibility of achieving very low tolerances, which is possible using MATLAB, the values obtained are not as accurate and sometimes may not reach the desired minimum value.

The importance of the sensitivity analyses carried out should be highlighted. Besides allowing the creation of confidence intervals for each parameter, it also allowed to conclude about the importance of the noise, especially on the shunt resistance parameter, where the higher the percentage, the more unexpected is the behaviour of its error function.

Finally, it is important to mention that all the work developed in the dissertation is integrated in NeuralSolar startup project and respective patent.

Considering the work performed, there are topics that can be developed in the future, such as:

1. Optimization of the modified *Nelder-Mead* algorithm, mainly to tune the search ranges of values for the vertices of the initial simplex as well as the minimum number of elements required for the search.
2. Take temperature readings when the panel is exposed to solar radiation.
3. Another important point that should be studied is the behaviour of the shunt resistance when white noise is applied. This parameter, unlike the others, has an uncertain behaviour whenever noise is applied, whose curves have different shapes and minimum values of different magnitudes.
4. The developed application can be connected locally or remotely to a photovoltaic panel with the purpose that it works as an auxiliary tool to identify the initial guesses to apply to the *modified Nelder-Mead algorithm*.
5. In order to identify the best initial guesses, as an alternative to the application, an intensive study of the measured IV characteristic curve could be done. In the present work, through the flat area analysis it was estimated possible values for the photocurrent and series resistance. In this sense the behaviour of the curve could be studied to estimate values for the remaining parameters.
6. The experimental results obtained by applying the ESP32 microcontroller are not the same as those obtained using the MATLAB tool. In this sense, due to memory issues and ESP32 characteristics, it could be necessary to use a device with more memory/processing capacity such as the TM4C123G board from Texas Instrument or a Raspberry PI board. Thus, the ESP32 microcontroller connected to the INA219 sensor would be exclusively responsible for reading the measurements at the PV output while the additional board with more features has the *modified Nelder-Mead algorithm* implemented and performs the calculation of the M_{PP} value.
7. Since it is intended to create an automatic system, the use of a variable resistor as a load does not become practical. Therefore, it would be necessary to create a circuit with additional electronics with a feature similar to the function generator allowing the IV curve to be plotted. There are several methods for doing this electronically and some of them are described in the article. [109]

CHAPTER

5

References

[1]   S. Kalogirou, Solar Energy Engineering, Academic Press, 2009.

[2]   NASA, "Solar Dynamics Observatory," [Online]. Available: https://sdo.gsfc.nasa.gov/assets/img/browse/2010/08/19/20100819_003221_4096_0304.jpg. [Accessed 2022 June 30].

[3]   F. Pereira and M. Oliveira, Curso Técnico Instalador de Energia Solar Fotovoltaica, Porto: Publindústria, 2015.

[4]   M. Villalva, Energia Solar Fotovoltaica - Conceitos e Aplicações Sistemas Isolados e Conectados à Rede, Brasil: ÉRICA, 2012.

[5]   IRENA, "THE POWER TO CHANGE: SOLAR AND WIND COST REDUCTION POTENTIAL TO 2025," International Renewable Energy Agency, Germany, 2016.

[6]   "Global Solar Atlas," [Online]. Available: https://globalsolaratlas.info/map. [Accessed 2022 June 30].

[7]   A. Albino, D. Bortoli, M. Tlemçani, A. Hajjaji and A. Joyce, "Sensitivity analysis of atmospheric spectral irradiance model," *The European Physical Journal,* 2019.

[8]   NASA, "World of Change: Global Temperatures," 2022. [Online]. Available: https://earthobservatory.nasa.gov/world-of-change/global-temperatures. [Accessed 22 July 2022].

[9]   L. DAHLMAN and R. LINDSEY, "Climate Change: Global Temperature," 28 June 2022. [Online]. Available: https://www.climate.gov/news-features/understanding-climate/climate-change-global-temperature#:~:text=June%2028%2C%202022-,Highlights,based%20on%20NOAA's%20temperature%20data.. [Accessed 22 July 2022].

[10]   eia, "Fossil fuels still dominate U.S. energy consumption despite recent market share decline," 1 July 2016. [Online]. Available: https://www.eia.gov/todayinenergy/detail.php?id=26912. [Accessed 22 July 2022].

[11]   EPA, "Global Greenhouse Gas Emissions Data," 25 February 2022. [Online]. Available: https://www.epa.gov/ghgemissions/global-greenhouse-gas-emissions-data. [Accessed 22 July 2022].

[12]   P. Reis, "Portal Energia - Energias Renováveis," 15 July 2016. [Online]. Available: https://www.portal-energia.com/vantagens-e-desvantagens-das-energias-renovaveis/. [Accessed 22 July 2022].

[13] R. Tripathi, G. Tiwari, T. Bhatti and M. Shukla, "Comparison of electrical energy and power of PV with different cells materials in clear sky day condition," *Materials Today: Proceedings,* pp. 693-696, 2021.

[14] O. Mesbahi, M. Tlemçani, F. M. Janeiro, A. Hajjaji and K. Kandoussi, "Recent Development on Photovoltaic Parameters Estimation: Total Least Squares Approach and Metaheuristic Algorithms," *Energy Sources, Part A: Recovery, Utilization, and Environmental Effects,* vol. 44, no. 2, p. 4546–4564 , 2022.

[15] T. Hai, J. Zhou and K. Muranaka, "An efficient fuzzy-logic based MPPT controller for grid-connected PV systems by farmland fertility optimization algorithm," *Optik - International Journal for Light and Eletron Optics,* 2022.

[16] M. Khan, M. Zafar, M. Mansoor, A. Mirza, U. Khan and N. Khan, "Green energy extraction for sustainable development: A novel MPPT technique for hybrid PV-TEG system," *Sustainable Energy Technologies and Assessments,* 2022.

[17] S. Fan, W. Liang, G. Wang, Y. Zhang and S. Cao, "A novel water-free cleaning robot for dust removal from distributed photovoltaic (PV) in water-scarce areas," *Solar Energy,* pp. 553-563, 2022.

[18] E. Becquerel, Memoire sur les Effects d'Electriques Produits Sous l'Influence des Rayons Solaires, vol. 9, Comptes Rendus de l'Academie des Sciences, 1839, pp. 561-567.

[19] W. Adams and . R. Day, The action of light on selenium, Proceedings of the Royal , 1877.

[20] "First photovoltaic Devices," [Online]. Available: https://www.pveducation.org/es/fotovoltaica/first-photovoltaic-devices. [Accessed 2022 June 20].

[21] "Albert Einstein – Biographical," 25 July 2022. [Online]. Available: https://www.nobelprize.org/prizes/physics/1921/einstein/biographical/.

[22] "Photoelectric Effect," 25 July 2022. [Online]. Available: https://physics.info/photoelectric/.

[23] D. M. Chapin, C. S. Fuller and . G. L. Pearson, "A New Silicon p-n Junction Photocell for Converting Solar Radiation into Electrical Power," *Journal of Applied Physics,* 1954.

[24] D. M. Chapin, C. S. Fuller and . G. L. Pearson, "Solar Energy Converting Apparatus". Patent US2780765, 1965.

[25] G. L. Pearson, "Conversion of solar to electric energy," *American Journal of Physics,* 1957.

[26] S. Parks, "This woman realized the sun's potential long before the rest of the country," [Online]. Available: https://timeline.com/woman-solar-power-leader-f682bb7c6feb. [Accessed 2022 July 10].

[27] "Wikipédia - Vanguard 1," [Online]. Available: https://pt.wikipedia.org/wiki/Vanguard_1. [Accessed 2022 June 20].

[28] "Wikipédia - Mars Exploration Rovers," [Online]. Available: https://pt.wikipedia.org/wiki/Mars_Exploration_Rovers. [Accessed 2022 July 20].

[29] M. M. Koltun, "History of solar cell development in the Soviet space program and the terrestrial potential for this technology," *Solar Energy Materials and Solar cells,* pp. 293-317, 1996.

[30] J. Lindemeyer and . J. F. Allison, "The violet cell: An improved silicon solar cell," *Solar Cells,* pp. 151-166, 1990.

[31] J. Mandelkorn and J. H. Lamneck, "Simplified fabrication of back surface electric field silicon cells and novel characteristics of such cells," *Solar Cells,* pp. 121-130, 1990.

[32] J. Haynos, J. Allison, R. Arndt and A. Meulenberg, "The COMSAT non-reflexive silicon solar cell: a second generation improved cell," 1974.

[33] M. Green, A. Blakers, S. Narayanan and M. Taouk, "Improvements in silicon solar cell efficiency," *Solar Cells,* pp. 75-83, 1986.

[34] R. Sinton, Y. Kwark, S. E. Swirhun and R. Swanson, "Silicon point contact concentrator solar cells," *IEEE Electron Device Letters,* pp. 405 - 407, 1985.

[35] T. M. Bruton and J. M. Woodock, "Multimegawatt upscaling of silicon and thin film solar cell and module manufacturing," 1997.

[36] J. Zhao, A. Wang, . M. A. Green and F. Ferrazza, "Novel 19.8% efficient "honeycomb" textured multicrystalline and 24.4% monocrystalline sili-con solar cells," *Applied Physics Letters,* 1998.

[37] D. Zielke, S. Herlufsen, F. Werner and J. Schmidt, "Multicrystalline Silicon Solar Cells Exceeding 20% Efficiency," *29th European Photovoltaic Solar Energy Conference and Exhibition,* pp. 1282 - 1285, 2004.

[38] R. King, C. Fetzer, P. Colter, K. Edmondson, D. Law, A. Stavrides, H. Yoon, G. Kinsey, H. Cotal, J. Emer, R. Sherif, K. Emery, W. Metzger, R. Ahrenkiel and N. Karam, "Lattice-matched and metamorphic GaInP/GaInAs/Ge concentrator solar cells," *3rd World Conference onPhotovoltaic Energy Conversion,* pp. 622-625, 2003.

[39] M. Viaud, W. Hoffman and H. Aulich, "European PV Industry roadmap," *Proceedings 19th EPVSEC,* 2004.

[40] Energia Fotovoltaica: manual sobre tecnologias, projecto e instalação, Lisboa: Instituto Superior Técnico, 2004.

[41] D. De Rooij, "SinoVoltaics - Monocrystalline Silicon Cells: efficiency and manufacturing," [Online]. Available: https://sinovoltaics.com/learning-center/solar-cells/monocrystalline-silicon-cells/. [Accessed 2022 June 20].

[42] "indiamart," [Online]. Available: https://www.indiamart.com/proddetail/amorphous-silicon-solar-cell-13679537662.html. [Accessed 2022 June 20].

[43] M. F. Ashby, Materials selection in mechanical design, Oxford: Butterworth Heinmman, 1999.

[44] J. Carneiro and M. Passos, Sistemas Fotovoltaicos - Fundamentos sobre Dimensionamento, Porto: Quântica Editora, 2020.

[45] M. Bolotinha, "Conducting and Insulating Materials," *Neutro à Terra,* 2016.

[46] P. Y. Yu and M. Cardona, Fundamentals of semiconductors, London: Springer, 2010.

[47] A. Heeger, A. MacDiarmid and H. Shirakawa, "The Nobel Prize in Chemistry, 2000: Conductive polymers," in *Royal Swedish Academy of Sciences*, Sweden, 2000.

[48] "Hyperphysics - Semiconductor Current," [Online]. Available: http://hyperphysics.phy-astr.gsu.edu/hbase/Solids/intrin.html. [Accessed 2022 July 10].

[49] J. Carneiro, SEMICONDUTORES – Modelo Matemático da célula fotovoltaica, Universidade do Minho, 2010.

[50] B. Razavi, Fundamentals of Microeletronics, 2006.

[51] M. Villavalva, J. Gazoli and E. Filho, "Comprehensive Approach to Modeling and Simulation of Photovoltaic Arrays," *IEEE TRANSACTIONS ON POWER ELECTRONICS,* vol. 24, pp. 1098-1208, 2009.

[52] G. Ciulla, V. Lo Brano, V. Di Dio and G. Cipriani, "A comparison of different one-diode models for the representation of I–V characteristic of a PV cell," *Renewable and Sustainable Energy Reviews,* vol. 32, pp. 684-696, February 2014.

[53] J. Cubas, S. Pindado and M. Victoria, "On the analytical approach for modeling photovoltaic systems behavior," *Journal of Power Sources,* pp. 467-474, 2014.

[54] K. Ishaque, Z. Salam and H. Taheri, "Simple, fast and accurate two-diode model for photovoltaic modules," *Solar Energy Materials & Solar Cells,* pp. 586-594, 2011.

[55] N. Femia, G. Petrone, G. Spagnulo and M. Vitelli, Power Electronics and Control Techique for Maximum Energy Harvesting in Photovoltaic Systems, New York: CRC Press, 2013.

[56] M. T. Ahmed, "Modelization and Characterization of Photovoltaic Panels," University of Évora, Évora, Portugal, 2017.

[57] A. Foles, ""MPPT study from a solar photovoltaic panel according to perturbations induced by shadows," University of Évora, Évora, Portugal, 2017.

[58] A. R. Jordehi, "Parameter estimation of solar photovoltaic (PV) cells: A review," *Renewable and Sustainable Energy Reviews,* pp. 354-371, 2016.

[59] T. Tabu, J. Ram, K. Sangeetha, A. Laudani and N. Rajasekar, "Parameter extraction of two diode solar PV model using Fireworks algorithm," *Solar Energy,* pp. 265-276, 2016.

[60] W. De Soto, S. Klein and W. Beckman, "Improvement and validation of a model for photovoltaic array performance," *Solar Energy,* vol. 80, pp. 78-88, 2006.

[61] H. Can, K. Parlak and D. Ickilli, "A New Numerical Solution Approach for the Real-Time Modeling of Photovoltaic Panels," *Asia-Pacific Power and Energy Engineering Conference,* pp. 1-4, 2012.

[62] O. Mesbahi, M. Tlemçani , F. M. Janeiro, A. Hajjaji and K. Kandoussi, "A Modified Nelder-Mead Algorithm for Photovoltaic Parameters Identification," *International Journal of Smart Grid,* vol. 4, no. 1, March 2020.

[63] F. Jingxun, L. Shaowu, Z. Xianping and L. Yan, "Research on Photovoltaic Cell Models : A Review," *33rd Chinese Control and Decision Conference (CCDC),* pp. 1006-1011, 2021.

[64] S. Chapra and R. Canale, Numerical Methods for Engineers, New York: McGraw-Hil, 2010.

[65] L. Gong, G. Hou and C. Huang, "A two-stage MPPT controller for PV system based on the improved artificial bee colony and simultaneous heat transfer search algorithm," *ISA Transactions,* 2022.

[66] E. Moshksar and T. Ghanbari, "A model-based algorithm for maximum power point tracking of PV systems using exact analytical solution of single-diode equivalent model," *Solar Energy,* vol. 162, pp. 117-131, 2018.

[67] Z. Chen, L. Wu, P. Lin, Y. Wu and S. Cheng, "Parameters identification of photovoltaic models using hybrid adaptive Nelder-Mead simplex algorithm based on eagle strategy," *Applied Energy,* no. 182, pp. 47-57, 2016.

[68] C. Kumar and D. M. Mary, "A novel chaotic-driven Tuna Swarm Optimizer with Newton-Raphson method for parameter identification of three-diode equivalent circuit model of solar photovoltaic cells," *Optik - International Journal for Light and Eletron Optics,* no. 264, 2022.

[69] R. Burbano, G. Petrone and P. Manganiello, "Early Detection of Photovoltaic Panel Degradation through Artificial Neural Network," *Applied Sciences,* vol. 11, no. 19, 2021.

[70] O. Mesbahi, K. Kandoussi, R. E. otmani, A. Hajjaji, F. M. Janeiro and M. Tlemçani, "Global MPP Tracking for Photovoltaic Panel under Shading Conditions using Robust Numerical Algorithm," in *IOP Conference Series Materials Science and Engineering*, 2020.

[71] V. R. Kota and M. N. Bhukya, "A novel linear tangents based P & O scheme for MPPT of a PV system," *Renewable and Sustainable Energy Reviews,* pp. 257-267, 2017.

[72] S. Rajamand, "A novel sliding mode control and modified PSO-modified P&O algorithms for peak power control of PV," *ISA Transactions,* 2020.

[73] M. Seyedmahmoudian, B. Horan, T. K. Soon, R. Rahmani and A. M. T. Oo, "State of the art artificial intelligence-based MPPT techniques for mitigating partial shading effects on PV systems – A review," *Renewable and Sustainable Energy Reviews,* no. 64, pp. 435-455, 2016.

[74] T. Konjić, A. Jahić and J. Pihler, "Artificial Neural Network Approach to Photovoltaic System Power Output Forecasting," in *18th Intelligence Systems Applications to Power Systems*, Porto, Portugal, 2015.

[75] R. Guarnieri, E. Pereira and S. C. Chou, "Solar radiation forecast using artificial neural networks in south Brazil," in *Proceedings of 8 ICSHMO*, Foz do Iguaçu, Brazil, 2016.

[76] D. Rumelhart, R. Williams and G. Hinton, "Learning representations by back-propagating errors," *Nature,* vol. 323, 1986.

[77] H. Oudira, A. Mezache and C. Aissa, "A prediction Model Based on Nelder-Mead Algorithm for the Energy Production of PV Module," *International Journal of Information Science & Technology ,* vol. 3, no. 3, 2019.

[78] G. Lindfield and J. Penny, Numerical Methods Using Matlab, England: Academic Press, 2019.

[79] O. Mesbahi, H. Abdeloawahed, T. Mouhaydine, K. Khalid and F. M. Janeiro, "Estimation of Photovoltaic Panel Parameters by a Numerical Heuristic Searching Algorithm," *8th International Conference on Renewable Energy Research and Applications (ICRERA),* November 2019.

[80] O. Mesbahi, M. Tlemçani, F. M. Janeiro, A. Hajjaji and K. Kandoussi, "Sensitivity analyses of a new approach to the photovoltaic parameters extraction based on the Total Least Squared method," *Metrology and Measurement Systems,* vol. 28, no. 4, p. 751–765, 2021.

[81] Z. Chen, Y. Lin, L. Wu, S. Cheng and P. Lin, "Development of a capacitor charging based quick I-V curve tracer with automatic parameter extraction for photovoltaic arrays," *Energy Conversion and Management ,* vol. 226, 2020.

[82] N. Hamid, N. Rahim and J. Selvaraj, "Solar cell parameters identification using hybrid Nelder-Mead and modified particle swarm optimization," *Journal of Renewable and Sustainable Energy ,* 2016.

[83] D. Byatt, "Convergent Variants of the Nelder-Mead Algorithm," University of Canterbury, 2000.

[84] M. T. Ahmed, M. Tlemcani and T. Goncalves, "Analysis of Noise with Curve Fitting Method of a PV cell," *EAI Endorsed Transactions on Energy Web,* vol. 3, 2017.

[85] MathWorks, "Help Center - movmean," The MathWorks, Inc., [Online]. Available: https://www.mathworks.com/help/matlab/ref/movmean.html. [Accessed 10 June 2022].

[86] R. Gouveia and S. Sousa, "Significados - Intervalo de Confiança," [Online]. Available: https://www.significados.com.br/intervalo-de-confianca/. [Accessed 26 August 2022].

[87] G. C. Espinosa, "Interfaz para el control vectorial de motores de imanes permanentes," Escuela Técnica Superior de Inginieros Industriales - Universidad Politécnica de Madrid, Madrid, 2018.

[88] MathWorks, "MATLAB GUI - Create apps with graphical user interfaces in MATLAB," [Online]. Available: https://www.mathworks.com/discovery/matlab-gui.html. [Accessed 18 June 2022].

[89] MathWorks, "MATLAB App Designer," [Online]. Available: https://www.mathworks.com/products/matlab/app-designer.html. [Accessed 18 June 2022].

[90] A. Pranadi, Q. Haramaini, A. Setiawan, E. Setiawan and C. Ali, "Sensitivity Analysis of Financial Parameters in Varying PV Penetrations in the Optimum Location of a Feeder," *Energy Procedia,* vol. 156, pp. 95-99, 2019.

[91] M. R. Rashel, "Modeling Photovoltaic Panels Under Variable internal and Enironmental Condition with non-contant load," Universidade de Évora, Évora, 2018.

[92] M. R. Rashel, T. Goncalves, M. Tlemcani and J. Rifath, "Sensitivity Analysis Through Error Function of Crystalline-Si Photovoltaic Cell Model Integrated in a Smart Grid," *International Journal of Renewable Energy Research,* vol. 7, no. 4, 2017.

[93] R. J. Hyndman and A. B. Koehler, "Another look at measures of forecast accuracy," *International Journal of Forecasting,* vol. 22, no. 4, pp. 679-688, 2006.

[94] R. G. Pontius, H. Chen and O. Thontteh, "Components of information for multiple resolution comparison between maps that share a real variable," *Environmental and Ecological Statistics,* no. 15, pp. 111-142, 2008.

[95] D. Chicco, M. J. Warrens and G. Jurman, "The coefficient of determination R-squared is more informative than SMAPE, MAE, MAPE, MSE and RMSE in regression analysis evaluation," *PeerJ Comput Sci,* vol. 7, no. 623, 2021.

[96] T. Instruments, *INA219 Zerø-Drift, Bidirectional Current/Power Monitor With I2C Interface,* August 2008– Revised December 2015.

[97] "Curto Circuito - INA219 como usar," [Online]. Available: https://www.curtocircuito.com.br/blog/Categoria%20Arduino/ina219-como-usar.

[98] "3E UNICAMP - Microcontroladores ESP: conheça tudo sobre esse poderoso equipamento," 7 March 2022. [Online]. Available: https://3eunicamp.com/microcontroladores-esp/. [Accessed 7 July 2022].

[99] "ESP 32 Wifi e Bluetooth," [Online]. Available: https://www.wjcomponentes.com.br/esp-32.

[100] E. Systems, "ESP32 Series Datasheet".

[101] OnEletronTech, "NI Multifunction I/O DAQ Devices Turn PCs Into Data Acquisition Systems," OnEletronTech, November 5 2020. [Online]. Available: https://www.onelectron-tech.com/ni-multifunction-i-o-daq-devices-turn-pcs-into-data-acquisition-system/. [Accessed July 11].

[102] M. Baptista, "Sistemas de Aquisição de Dados," Departamento de Informática - Escola Superior de Viseu, Viseu.

[103] "Data Acquisition Card (DAQ) function," [Online]. Available: https://automation-forum.co/data-acquisition-card-daq-function/. [Accessed 2022 July 30].

[104] ni, "ni - USB-6009 Dispositivo E/S multifunção," [Online]. Available: https://www.ni.com/pt-pt/support/model.usb-6009.html. [Accessed 2022 July 11].

[105] ni, "ni - USB-6009 Specifications," [Online]. Available: https://www.ni.com/docs/en-US/bundle/usb-6009-specs/page/specs.html. [Accessed 2022 July 11].

[106] FEUP, "FEUP - Gerador de Funções," Faculdade de Engenharida da Universidade do Porto, 2007. [Online]. Available: https://paginas.fe.up.pt/~ee00264/equipamentos/gerador.html. [Accessed 2022 July 11].

[107] Tektronix, "Arbitrary Function Generators - AFG310, AFG320," Tektronix, [Online]. Available: https://www.tek.com/en/datasheet/afg310-afg320. [Accessed 2022 July 11].

[108] ni, "ni - GPIB-USB-HS - Dispositivo de controle de instrumentos por GPIB," ni, 2022. [Online]. Available: https://www.ni.com/pt-pt/support/model.gpib-usb-hs-.html. [Accessed 11 July 2022].

[109] Y. Zhu and W. Xiao, "A comprehensive review of topologies for photovoltaic I–V curve tracer," *Solar Energy,* pp. 346-357, 2020.

[110] J. Matias, "O Que São Díodos?," 14 May 2011. [Online]. Available: https://www.jose-matias.pt/eletr/o-que-sao-diodos/. [Accessed 2022 August 28].

[111] Semiconductor Eletronics: Materials, Devices and Simple Circuits, "Intrinsic Semiconductor," toppr, 2022. [Online]. Available: https://www.toppr.com/guides/physics/semiconductor-electronics-materials-device-and-simple-circuits/intrinsic-semiconductor/. [Accessed 11 July 2022].